Title
Mesoscale coupled ocean-atmosphere feedbacks in boundary current systems

Author
Putrasahan, Dian Ariyani

Publication Date
2012

Peer reviewed|Thesis/dissertation

UNIVERSITY OF CALIFORNIA, SAN DIEGO

Mesoscale Coupled Ocean-Atmosphere Feedbacks in Boundary Current Systems

A dissertation submitted in partial satisfaction of the
requirements for the degree
Doctor of Philosophy

in

Oceanography

by

Dian Ariyani Putrasahan

Committee in charge:

Arthur J. Miller, Chair
Sarah Gille
Petr Krysl
Joel Norris
Richard Salmon
Guang Zhang

2012

The dissertation of Dian Ariyani Putrasahan is approved, and it is acceptable in quality and form for publication on microfilm and electronically:

____

____

____

____

____

____

Chair

University of California, San Diego

2012

DEDICATION

Dedicated to my parents, George and Jacinta Putrasahan

EPIGRAPH

For most of history, man has had to fight nature to survive; in this century he is beginning to realize that, in order to survive, he must protect it.

— Jacques-Yves Cousteau

It is clear that the study of the joint interannual variability of the coupled ocean-atmosphere system has demanded the creation of a new breed of scientist, one who is equally adept in understanding processes in the ocean and in the atmosphere. This is an important change in the paradigm of scientific concentrations that have channeled our thinking for many centuries. However, this new amphibious beast has more responsibility than merely understanding common vagaries of two spheres instead of one. The amphibian is at the forefront of a revolution in the very fabric of human endeavor and humankind.

— Henry F. Diaz

TABLE OF CONTENTS

LIST OF FIGURES

ACKNOWLEDGEMENTS

First, I would like to express my deepest gratitude to **Art Miller** for being such a great advisor and mentor. His guidance, support and encouragement has carried me through my graduate career. His energy and enthusiasm for science is an inspiration. I'm also grateful for his kindness and generosity in sending me to conferences and meetings all over the world, to develop my presentation skills and meet other scientists. But most of all, I want to thank Art for being such a wonderful friend, for sharing life stories and laughters. Thank you so much Art!

I would like to thank my committee members, **Sarah Gille**, **Guang Zhang**, **Rick Salmon**, **Joel Norris** and **Petr Krysl** for their time, their great ideas and suggestions for scientific studies, and their advise in my professional career. I would also like to thank the late **John Roads** for his support and guidance that was crucial. He is dearly missed.

I'm very grateful to **Hyodae Seo**, **Kei Yoshimura** and **Emanuele Di Lorenzo** for all their guidance, especially in plowing through model codes, and for their encouragement in times when the model errors look impossible to decipher. They are wonderful friends and mentors.

A huge thank you to my fellow Scripps friends for all the distractions and making life so great for the past 7 years. To name but a few of my amazing friends, **Anais, Lauren, Robert, Stephanie, Ha Joon, Jim, Kyla, San, Gordy, Kaushik, Yvonne, Ben, Peter, Aneesh, Gino, Nathalie** and **Geoff**. Also a huge thank you to the ICCSD family for further distractions, support and prayers, particularly **Yuko, Freddy, Andre, Carissa, Jerry, Carol and the family, Alice, David, Carl** and **Rice** & **Virtue group**.

Special thanks to **Michael Keil, Enny Wijaya, Cailing Huang, Zhu Jun** and **Mei Liong** for their support and encouragement, specifically through long hours on the phone.

I'm deeply grateful to my parents, **George and Jacinta**, my brothers, **Perri and Kris**, family and relatives for their love and support. They may be spread out all over the globe, some even half-way around the world, but their constant prayers and encouragement have been my comfort and strength.

Finally, I am forever thankful to my **heavenly Father**, His Son **Jesus Christ** and the **Holy Spirit**, for all the love and grace that is showered upon me, carried me and sustained me through everything.

Chapter 3, in part, is being prepared for publication. Dian Ariyani Putrasahan, Arthur J. Miller, and Hyodae Seo. I am the primary investigator and author of this paper.

Chapter 4, in part, is being prepared for publication. Dian Ariyani Putrasahan, Arthur J. Miller, and Hyodae Seo. I am the primary investigator and author of this paper.

VITA

2004	B. S. in Chemical Engineering, Georgia Institute of Technology
2004	M. S. in Chemical Engineering, Georgia Institute of Technology
2012	Ph. D. in Oceanography, Scripps Institution of Oceanography, University of California - San Diego

PUBLICATIONS

Putrasahan, D. A., A. J. Miller and H. Seo, 2012: Coupled ocean-atmosphere interactions between the oceanic mesoscale and the atmospheric boundary layer in the Southeast Pacific. *Atmospheric Chemistry and Physics (VOCALS Special Issue)*, in preparation.

Putrasahan, D. A., A. J. Miller and H. Seo, 2012: Isolating mesoscale coupled ocean-atmosphere interactions in the Kuroshio Extension region. *Dynamics of Atmospheres and Oceans*, in preparation.

ABSTRACT OF THE DISSERTATION

Mesoscale Coupled Ocean-Atmosphere Feedbacks in Boundary Current Systems

by

Dian Ariyani Putrasahan

Doctor of Philosophy in Oceanography

University of California, San Diego, 2012

Arthur J. Miller, Chair

The focus of this dissertation is on studying ocean-atmosphere (OA) interactions in the Humboldt Current System (HCS) and Kuroshio Extension (KE) region using satellite observations and the Scripps Coupled Ocean-Atmosphere Regional (SCOAR) model. Within SCOAR, a new technique is introduced by implementing an interactive 2-D spatial smoother within the SST-flux coupler to remove the mesoscale SST field felt by the atmosphere. This procedure allows large-scale SST coupling to be preserved while extinguishing the mesoscale eddy impacts on the atmospheric boundary layer (ABL). This technique provides insights to spatial-scale dependence of OA coupling, and the impact of mesoscale features on both the ABL and the surface ocean.

For the HCS, the use of downscaled forcing from SCOAR, as compared to NCEP Reanalysis 2, proves to be more appropriate in quantifying wind-driven upwelling indices along the coast of Peru and Chile. The difference in their wind stress distribution has significant impact on the wind-driven upwelling processes and total upwelling transport along the coast. Although upwelling induced by coastal Ekman transport dominates the wind-driven upwelling along coastal areas, Ekman pumping can account for 30% of the wind-driven upwelling in several coastal locations. Control SCOAR shows significant SST-wind stress coupling during fall and winter, while Smoothed SCOAR shows insignificant coupling throughout, indicating the important role of ocean mesoscale eddies on air-sea coupling in HCS. The SST-wind stress coupling however, did not produce any rectified response on the ocean eddies. Coupling between SST, wind speed and latent heat flux is insignificant on large-scale coupling and full coupling mode. On the other hand, coupling between these three variables are significant on the mesoscale for most of the model run, which suggests that mesoscale SST affects latent heat through direct flux anomalies as well as indirectly through stability changes on the overlying atmosphere, which affects surface wind speeds and thus latent heat flux.

In the KE region, differences in the strength of coupling between the Control and Smoothed SCOAR runs indicate how the spatial scale of SST fronts affects the OA coupling via two distinct mechanisms, the vertical mixing mechanism (VMM) and the pressure adjustment mechanism (PAM). Intuitively, one might expect that the VMM would be most active on the ocean mesoscale and less significant on the large scale. Instead, the model revealed that the VMM, expressed through the coupling between downwind SST gradient and wind stress divergence, acts strongly on both the large scale and mesoscale. In contrast, coupling between crosswind SST gradients and wind stress curl is seen on the mesoscale, but extinguished over large-scale SST gradients, revealing the vital role of ocean mesoscale. For PAM, one might expect the large-scale coupling to be dominant in establishing the PAM. Instead, model results suggest that in PAM, the coupling between the Laplacian of sea level pressure and surface wind convergence are active on both the mesoscale and the large scale, though the coupling strength nearly doubles with the inclusion of ocean mesoscale. Ocean mesoscale imprints are also seen on precipitation anomalies, for which their differences are more aligned with the differences in SST gradients and surface wind convergence rather than SST anomalies.

Chapter 1

Introduction

Global and regional climate models have worked well to simulate ocean circulation and atmospheric flow patterns on the large scale. It was not till recent times that models are able to resolve mesoscale spatial features, those of the order of 100km. Observations and models have been used to study ocean-atmosphere interactions in a fully-coupled mode that includes the range of large scale (order 1000km) to the mesoscale (Small et al., 2008; Chelton et al., 2001; Xie, 2004; Minobe et al., 2010). The crux of this thesis is to understand the relative roles of large-scale coupling versus mesoscale coupling when ocean-atmosphere coupling is observed. Here, a new technique is introduced to extract coupling at the mesoscale. This thesis explores the spatial scale dependence of ocean-atmosphere interactions in boundary current systems, particularly the Humboldt Current System and the Kuroshio Extension region.

The Southeast Pacific region is a region of great climate interest because of the vast distribution of stratocumulus cloud that reflects back incoming solar radiation and emits comparatively larger amounts of outgoing longwave radiation, thereby having a cooling effect on this planet. It also contains the most biologically productive oceanic eastern boundary current, providing an estimated of 18-20% of the world's fish catch (Sherman and Hempel, 2008). Typically known as the Humboldt Current System (HCS) or Peru-Chile Current System (PCCS), its high productivity is mainly attributed to the wind-driven upwelling, bringing in cold, nutrient-rich subsurface waters to the surface layer for the biology to feed on (Smith, 1968).

The climate of the Southeast Pacific involves important feedbacks between atmospheric circulation, sea-surface temperature (SST), clouds, ocean heat transport, aerosols, and coastal orography, bathymetry and geometry (e.g., Ma et al. (1996)). A major experimental and modeling effort called VOCALS (VAMOS [1] Ocean Cloud Atmosphere Land Studies) Program has been initiated to investigate these feedbacks. For this thesis, the study for the HCS is part of the VOCALS project, for which numerical experiments are set up to study (i) the SST-wind stress coupling in fully-coupled mode and large-scale coupled mode, (ii) the local impact of oceanic mesoscale on surface heat flux and the atmospheric boundary layer (ABL), and conversely, (iiI) the impact of SST-induced flux anomalies on ocean eddies.

In the North Pacific, the atmosphere drives basin-scale variability of SST via latent heat and sensible heat flux (Cayan, 1992), and thus suggests that the ocean is a slave to the atmosphere. This is supported by negative correlation of SST and winds found during winter months (Wallace et al., 1990). However, the presence of oceanic fronts prove to counter those results (Nakamura et al., 2004; Nonaka and Xie, 2003). A western boundary current in the North Pacific subtropical gyre, called the Kuroshio current, brings warm tropical water as it flows northward/ northeastward along the coast of Taiwan and Japan. It separates from the coast around 35°N and flows eastward to the open ocean and forms the Kuroshio Extension (KE) (Mizuno and White, 1983). A confluence of warm, northward flowing Kuroshio current and cold, southward Oyashio current from the north, along the eastern Japan coast forms a SST front with sharp gradients that affect the overlying atmospheric circulation (Nonaka and Xie, 2003; Xie, 2004), and have imprints that penetrate well into the free troposphere (Tokinaga et al., 2009; Minobe et al., 2010). In this thesis, the study of the KE region focuses on the effects of ocean-atmosphere boundary layer coupling, e.g., through SST affecting the stability of the atmospheric boundary and concomitantly altering the surface stresses and surface heat fluxes and, in turn, the altered fluxes affecting the ocean

[1] VAMOS is the abbreviation for Variability of the American MOnsoon Systems, which is an international, multidisciplinary CLIVAR program.

eddy statistics (Chelton et al., 2001; Samelson et al., 2002; Seo et al., 2006; Xie, 2004).

Chapter 2 will discuss the model used to study ocean-atmosphere interactions in the eastern and western boundary current systems. It will introduce a new technique to study the impact of full-coupling versus large-scale coupling, as well as a strategy to isolate mesoscale coupling.

Chapter 3 contains several studies pertaining to the Humboldt Current System. First is a simple study on the affects of wind products used on wind-driven upwelling along the coast of Peru and Chile. The second study is assessing SST-wind stress coupling through the vertical mixing mechanism in the Peruvian waters. The third study focuses on understanding the impact of mesoscale SST on wind speed and latent heat flux. The fourth is a short study on the effects of full coupling versus large-scale coupling on ocean eddy statistics.

Chapter 4 investigates coupled ocean-atmosphere interactions in the Kuroshio Extension System. The first section assesses SST-wind stress coupling through the vertical mixing mechanism and pressure adjustment mechanism, as well as SST-latent heat flux coupling. The second section focuses on the influence of SST on precipitation at the mesoscale.

Chapter 2

SCOAR Model

The Scripps Coupled Ocean-Atmosphere Regional (SCOAR) model is employed to perform coupled ocean-atmosphere interaction studies in the Humboldt Current System (HCS), as well as in the Kuroshio Extension (KE) region. This model is developed by Seo et al. (2007b). The model consists of the Experimental Climate Prediction Center (ECPC) Regional Spectral Model (RSM) as the atmospheric component, the Regional Ocean Modeling System (ROMS) as the oceanic part, and a flux-SST coupler to bridge the two. This model is chosen because it has shown to be effective in capturing mesoscale features in tropical and mid-latitudinal oceans (Seo et al., 2006, 2007a,b).

2.1 ROMS oceanic model

ROMS is an incompressible, free-surface, hydrostatic, primitive equation ocean model that utilizes a horizontal, orthogonal, curvilinear grid and a stretched sigma-coordinate system to enhance vertical resolution in the surface and bottom layers of the ocean (Haidvogel et al., 2000; Shchepetkin and McWilliams, 2005). It allows for different options of mixing and diffusion schemes, and a variety of ways to handle boundary conditions. Here, the KPP mixing scheme (Large et al., 1994) is chosen, along with a third-order upstream horizontal advection and a fourth-order centered vertical advection scheme for both tracers and momentum. Radiation nudging to open boundary conditions is used so that long-term integrations are more stable and nudging is adaptive to inflow/outflow ratio, meaning nudging is stronger on inflow than on outflow if the ratio is greater than 1. There are also a myriad of lateral boundary conditions that one can supply. Commonly, boundary conditions can be provided using the Levitus World Ocean Atlas data. One could also use climatological mean from 1990-2001 of temperature, salinity, horizontal currents and sea surface heights from Simplified Ocean Data Assimilation (SODA) products (Carton et al., 2000b,a). Another option is to use hindcast 1950-2007 OFES (OGCM [Ocean Global Climate Model] for the Earth Simulator) daily mean products (Sasaki et al., 2006, 2008) to force the lateral boundary conditions on ROMS. Both studies of the Humboldt Current System and the Kuroshio Extension uses OFES products for their oceanic lateral boundary conditions.

2.2 RSM atmospheric model

ECPC-RSM, here forth denoted plainly as RSM, is a hydrostatic, primitive equation atmospheric model that uses a terrain-following sigma-coordinate system. RSM is first developed by Juang and Kanamitsu (1994) at the National Center for Environmental Prediction (NCEP) and later revised and improved upon its dynamics and efficiency by Juang et al. (1997). Essentially, RSM provides regional details downscaled from the Global Spectral Model (GSM) that is physically and dynamically consistent with the NCEP/Department of Energy (DOE) Reanalysis (RA2) model (Kanamitsu et al., 2002a). This is done by nesting RSM non-interactively and one-way within GSM such that GSM forces RSM along the lateral boundaries as well as on the low-wavenumber (large-scale) fields through perturbations in the dynamics and physics.

The boundary layer (BL) parameterization in RSM uses a nonlocal diffusion scheme (Hong and Pan, 1996) that couples strongly with the surface layer physics. Above the BL, in the free troposphere, a local diffusion scheme is used. For the study in the HCS, the Relaxed Arakawa-Schubert scheme (Arakawa and Schubert, 1974; Moorthi and Suarez, 1992) is used for deep convective parameterization, while for the study in the KE region, the Zhang-McFarlene scheme (Zhang and McFarlane, 1995) along with Hack shallow convection scheme (Haack et al., 1992) is used. Both studies utilize the Yonsei University cloud water prediction scheme (Lim and Hong, 2010), which follows a double-moment cloud microphysics scheme that takes water vapor, cloud water and rain water as prognostic variables. The default setting of spectral tendency damping scheme was turned off to allow features of fields greater than 2000km within the domain to freely evolve. Please refer to (Kanamitsu et al., 2002b) for more details regarding the model physics.

2.3 Flux-SST coupler

With ROMS and RSM being independent models, a flux-SST coupler is needed to connect the two and allow for interactions between the ocean and atmosphere. This forms the third component of the SCOAR model. Figure 2.1 gives a graphic illustration of how the coupler works (Seo et al., 2007b). Currently, the coupling works in a sequential manner, such that RSM and ROMS run individually and alternatively, exchanging forcing fields only when one model run is completed, then the other model can commensurate the next run. Frequency of coupling can be done every 6 hours, daily, every 5 days or even every month, depending on timescales of interest.

For SCOAR, ROMS could either directly use surface flux fields provided by RSM, which is calculated from the non-local, BL parameterization scheme (RSM BL physics package), or it can use the Tropical Ocean Global Atmosphere Coupled Ocean Atmosphere Response Experiment (TOGA COARE) algorithm (Fairall et al., 1996) to calculate the surface momentum, latent and sensible heat fluxes from near-surface meteorological variables like air temperature, surface pressure, humidity, 10m winds, precipitation and cloudiness (bulk parameterization). RSM is only forced on the surface by SST, which is given by ROMS.

Under bulk parameterization scheme, wind stress (τ) that is imposed on to the ocean is typically computed as $\tau = \rho C_d|U_a|U_a$, where ρ is the air density, C_d is the drag coefficient and U_a is the wind at 10m height. This assumes that ocean current speed is generally an order of magnitude smaller than wind speed.

However, it has been noted that accounting for the relative motion of the wind to the ocean current when calculating wind stress could have a significant impact on the wind stress curl (Duhaut and Straub, 2006). Thus, SCOAR allows the option of accounting for the motion of the ocean currents by parameterizing wind stress as $\tau = \rho C_d |U_a - U_o|(U_a - U_o)$, where U_o is the ocean current.

The exchange of SST and surface fluxes between the ocean and atmosphere within SCOAR allows the the study of mesoscale coupled air-sea feedbacks. However, a new method to investigate mesoscale SST influence in a fully-coupled framework is introduced. This is done by employing the same mesoscale, coupled system and providing an online, 2-D spatial, locally weighted scatterplot smoothing (lowess/loess) filter (Cleveland, 1979; Schlax et al., 2001) to smooth out the mesoscale patterns at each coupling time step. The smoother can be utilized independently on atmospheric forcing fields and oceanic SST forcing, or it can be used to smooth both ways during each coupling step. Using an online, 2-D spatial filter on a coupled model would preserve the large-scale coupling while extinguishing the mesoscale coupling. This allows for comparative studies that would provide a sense of how large-scale coupling differs from full-coupling, and extracts the importance of mesoscale coupling. The interactive smoothing technique can also be used to determine the impact of the SST-induced flux anomalies (based on the difference between large-scale coupling and full-coupling) on the ocean eddies themselves.

Another application of the 2-D spatial smoother is to observe how mesoscale SST features can affect the atmospheric boundary layer (ABL). A more deterministic approach to isolate the effects of these mesoscale SST patterns is to apply the 2-D smoother upon the raw SST fields from a fully-coupled SCOAR run (Control SCOAR) and use these daily smoothed SST fields as a surface forcing onto the atmosphere (Smoothed RSM). The difference in the two runs will highlight the influence of mesoscale SST on the overlying atmosphere, as well as isolate mesoscale coupling. In a similar manner, the 2-D spatial smoother can also be implemented on forcing fields in uncoupled ocean experiments (Smoothed ROMS) to investigate the effects of mesoscale on the ocean eddy statistics. This combination of coupled and uncoupled smoothing strategy enables one to not only investigate the impact of mesoscale on the atmosphere and ocean, but also the effect of mesoscale coupling upon the atmosphere and ocean.

Essentially, the lowess filter is a locally weighted polynomial regression that for a given point, takes a subset of data (data within a certain radius from the point) and fits a low-degree polynomial using weighted least squares. It performs the weighted regression for each data point. The weighting function of the lowess filter gives higher weight to points that are closer to the desired point and and lesser weight as one goes further from the desired point. Traditionally, the weighting function is a tri-cubic weight function defined as

$$w(x) = (1 - |x|^3)^3$$

where x is a distance measure of the subset data to the desired point and $|x| < 1$ condition must be satisfied. When implemented into SCOAR, x is the ratio of the distance between any localized subset data point and the desired point to the specified radius of influence. The smoothing with this particular weighting function is roughly equivalent to using a running average of length approximately 0.6x(radius of influence).

Figure 2.2 gives an example of the performance of a 2.5-degree lowess filter upon the SST field for the HCS study. The top left and right panels show the averaged April 2007 SST field for Control SCOAR and Smoothed RSM respectively. The bottom left panel presents the difference between the two, which indicates that the lowess filter effectively removes patterns and filaments of scales roughly 2 degrees and less. The bottom right panel shows the SST power spectrum of latitudinal band, 20°S-36°S, for Control SCOAR and Smoothed RSM. The power spectrum indicates that the lowess filter preserves much of the energy at low wavenumber and rolls off as wavenumber increases. A ratio between the power spectrum of Smoothed RSM to Control SCOAR gives an estimate of the variance retained after smoothing, which provides a gauge of the cut-off wavelength for the lowess filter. In this case, the lowess filter cuts off 80% of the energy at wavelength of ~180km.

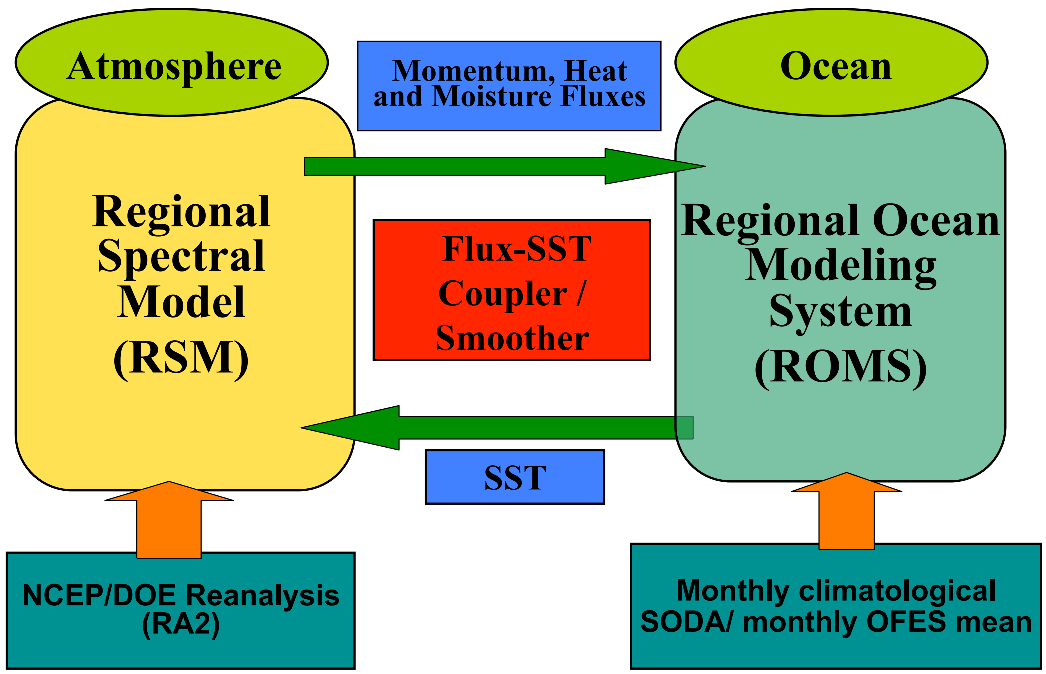

Figure 2.1: Schematic of the components in SCOAR, where the atmosphere (RSM) and ocean (ROMS) interacts through a SST-flux coupler. A 2-D spatial smoother has been implemented into the SST-flux coupler. This schematic is adapted from Seo et al. (2007b).

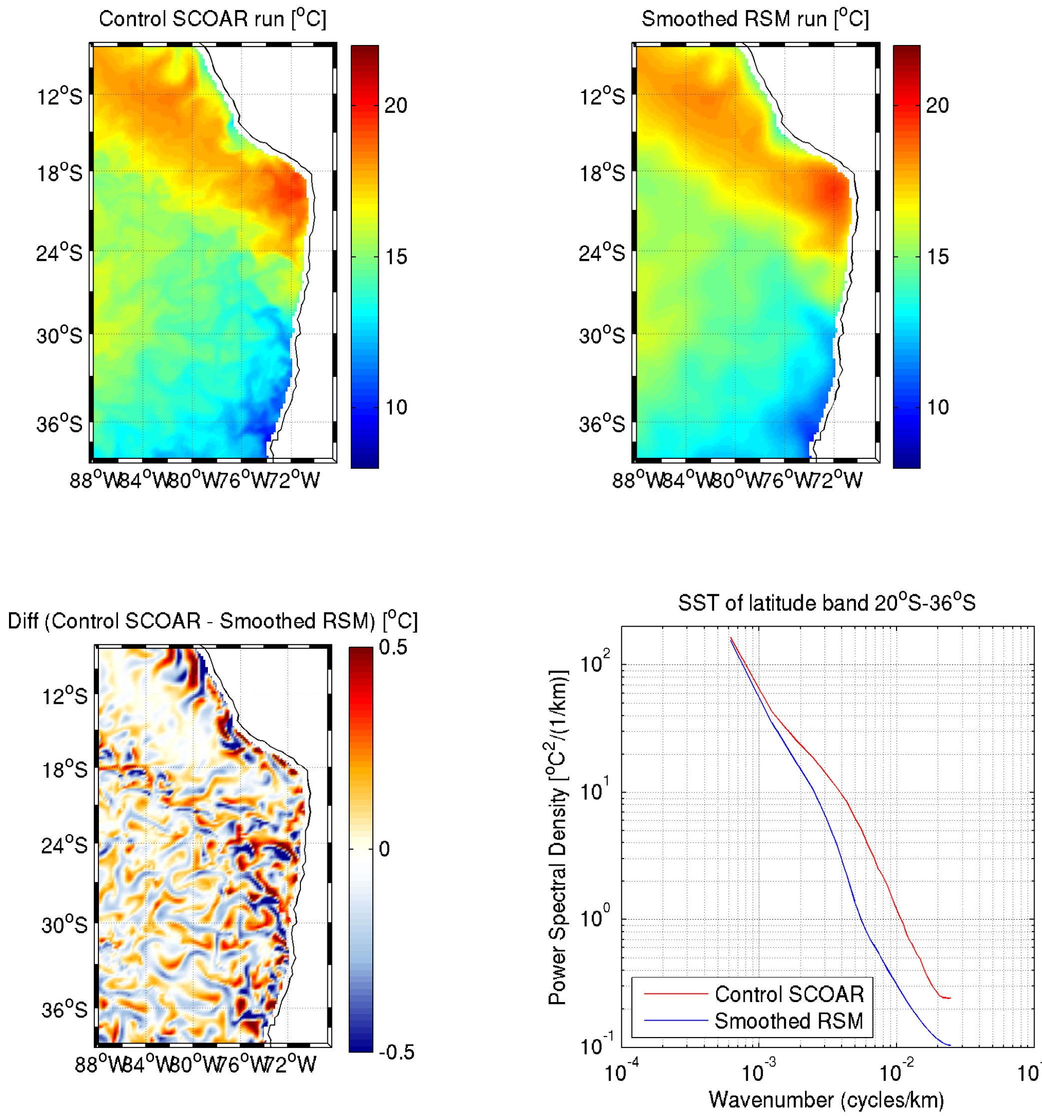

Figure 2.2: Averaged SST [°C] distribution during April 2007, over entire model domain for Control SCOAR (top left), Smoothed RSM (top right) and their difference (bottom left). The HCS region covers 88°W-68°W, 8°S-38°S. Bottom right panel: Power spectrum of SST for Control SCOAR (red) and Smoothed RSM (blue) in the latitudinal band, 20°S-36°S.

Chapter 3

Mesoscale Ocean-Atmosphere Coupling in the Humboldt Current System

3.1 Atmospheric Wind Forcing and Coastal Upwelling

The Humboldt current flows along the western coast of Chile and Peru in a northward and northwestward direction. It covers approximately 8% of the worlds surface ocean, and yet it provides an estimated 18-20% of the worlds fish catch (Sherman and Hempel, 2008). The availability of nutrients that supports the high productivity in the Humboldt Current System (HCS) is governed by the upwelling nutrient flux, of which, one factor of nutrient flux is dependent on upwelling that is driven by the winds. Nutrient flux can be affect by many factors such as nutrient availability in subsurface ocean, upwelling of nutrient-rich subsurface water, lateral advection of nutrient-poor/rich water, etc. In this particular study, it is assumed that wind-driven upwelling of cold, subsurface, nutrient-rich water is the main contributor to nutrient flux.

Sea surface temperatures (SST) are commonly used as a passive tracer for upwelled waters. Figure 3.1 shows the SST distribution over the Southeast

Pacific ocean, with names of several coastal locations, including coastal upwelling zones (indicated by cooler SSTs) at San Juan, Coquimbo and Punta Lavapie. In this study, the contribution of two wind-driven upwelling processes (Smith, 1968), namely Ekman transport and Ekman pumping, onto the total upwelling in various upwelling zones along the Peru and Chile coast, is assessed. Ekman transport along an eastern boundary of the ocean is the offshore transport of water pushed by equatorward, alongshore winds due to the Earths rotation. This offshore transport creates a mass deficit that is replaced by the upwelling of subsurface water along the coast. Ekman pumping (suction) is generated by negative (positive) wind stress curl that causes divergence (convergence) at the ocean surface, which then induces the upward (downward) motion of the water beneath.

The coastal Ekman upwelling transport (M_{Ek}, m^3/s per meter of coast) can be calculated as follows (Smith, 1968; Castelao and Barth, 2006),

$$M_{Ek} = \frac{\vec{\tau} \cdot \hat{a}}{\rho_w f}$$

where $\vec{\tau}$ is the wind stress vector, $\hat{a}$ is a unit vector along the coast for each zone, ρ_w is the density of seawater (1024kg/m^3) that is taken to be constant, and f is the Coriolis parameter that is a function of latitude. Coriolis parameter is given by $f = 2\Omega \sin\phi$, where $\Omega = 7.2921 \times 10^{-5} rad/s$ is the rotation rate of the Earth and ϕ is latitude. Using a method modified from Pickett and Panduan (2003), the Ekman transport along each coastal grid point for each zone is computed. Each zone has a coastal slope in which a straight line is fitted through the ocean point right next to land at the southmost and northmost end of the zone. The bearing of the coastal slope (angle α) is computed (Figure 3.2) and using this angle, the alongshore wind component is calculated.

Likewise, the Ekman pumping velocity (w_{Ek}) can be computed as follows (Smith, 1968; Halpern, 2002),

$$w_{Ek} = \frac{\nabla \times \vec{\tau}}{\rho_w f} + \frac{\beta \tau_x}{\rho_w f^2}$$

where τ_x is the zonal component of wind stress and β is the change in f with respect to latitude that can be approximated as $\beta = 2\Omega \cos\phi / R_{Earth}$, where R_{Earth} is the radius of the Earth (6378km).

Integration of w_{Ek} over some distance offshore from each coastal grid point was performed to get units of transport (W_{Ek}, m^3/s per meter of coast) that can be compared to Ekman upwelling transport. Over California Current System, the zero wind stress curl line would extend to about 200-300km offshore (Pickett and Panduan, 2003), which indicates the extent of transport by Ekman pumping. Similarly, using satellite-derived wind stress curl fields over the Humboldt Current System, this would extend to approximately 100-200km offshore. An estimate of the total wind-driven upwelling is obtained by taking the sum of both transports ($T_{Ek} = M_{Ek} + W_{Ek}$).

For this study, the Scripps Coupled Ocean-Atmosphere Regional (SCOAR) model is used. The model domain covers a regional grid from 88°W to 68°W and 8°S to38°S. The atmospheric and ocean model have the same horizontal grid with 20km resolution. However, the atmosphere has 28 vertical layers whilst the ocean has 30 layers. The vertical coordinates for the ocean model were stretched to give higher resolution to the surface layers. The ocean spin up (in uncoupled mode) is forced by National Center for Environmental Prediction Reanalysis-II (NCEP) winds from 1980-2000 to allow equilibration before any runs are performed. Daily averages are saved for both the oceanic and atmospheric state.

A comparative study is performed by using wind fields from SCOAR and NCEP R2 to investigate the contribution of coastal Ekman upwelling transport versus Ekman pumping transport to the total wind-driven upwelling along the coast. The wind fields are validated with Quick Scatterometer (QuikSCAT) winds at 0.5° resolution (Freilich et al., 1994; Liu, 2002). Satellite-observed winds over the ocean within 50km of the coast are not as accurate, and thus wind-driven coastal upwelling based on satellite observations are not used.

Figure 3.3 shows the seasonal cycle of wind stress field averaged over 2000-2007, for satellite observations. Satellite-derived wind stress fields indicate a consistent southerly/southeasterly winds off the coast of Peru and Chile throughout the year, with variations of the strength and location of the maxima. There is an anitcyclonic high around 85°W that migrates meridionally (about 30°S in summer and around 35°S in winter) and brings south-southwesterly winds to Chile at Concepcion during winter and westerly winds in other seasons. Coastal atmospheric jets seasonally form around San Juan (Peru) during fall (AMJ) through winter (JAS). In Chile, the coastal atmospheric jets typically form during spring (OND) and summer (JFM) along Coquimbo and Punta Lavapie (Garreuad and Munoz, 2005; Renault et al., 2009). Model-derived wind stress fields from SCOAR (Fig. 3.4) show similar spatial distribution and magnitude, which indicates the ability of SCOAR to downscale large-scale winds and provide the appropriate forcing over the ocean. For NCEP R2 (Fig. 3.5), the location of the maximum wind stress field has shifted offshore, which would affect the contribution of Ekman upwelling transport to the total upwelling, particularly along the coast.

The seasonal cycle of wind stress curl field derived from satellite observations is presented in Figure 3.6. It shows that near and along the coast, wind stress curl fields are negative and extend to approximately 100km offshore. Wind stress fields are generally positive further offshore from Chile, and mostly negative further offshore from Peru. Negative wind stress curl in the Southern Hemisphere is associated with upwelling due to Ekman pumping. SCOAR (Fig. 3.7) exhibits similar spatial patterns of wind stress curl, with stronger and narrower negative wind stress curl hugging along the coast. The exception is around Pisco/San Juan and Coquimbo, where there is a positive wind stress curl along the coast. This indicates that the wind stress maxima is located right on the coast rather than just near the coast. As for NCEP R2 (Fig. 3.8), wind stress curl following the coastline is mostly negative and extends to about 600km offshore, beyond which wind stress curl becomes positive throughout. During austral spring and summer, wind stress curl is positive along the coast in the southern part of the domain. The wider and more intense negative wind stress curl along the coast would impact the contribution of Ekman pumping on the total upwelling.

For five locations (marked on Fig. 3.1) along the coast of Peru and Chile, namely San Juan, Arica, Taltal, Tongoy and Punta Lavapie, the coastal Ekman upwelling transport (CEUT), Ekman pumping transport (EPT) and total wind-driven upwelling transport is computed based on the wind forcing from SCOAR and NCEP R2. For the CEUT along each location, the alongshore wind stress component of the grid point right next to the coast is used. Positive (negative) Ekman upwelling transport indicates offshore (onshore) transport that induces an equivalent upwelling (downwelling) right at the coast. For the transport due to Ekman pumping, the Ekman pumping velocity is integrated from the coast to approximately 100km offshore. Again, positive (negative) transport is associated with upwelling (downwelling) waters.

Beginning with San Juan, Figure 3.9 shows the CEUT, EPT and total wind-driven upwelling based on SCOAR and NCEP R2. Here, SCOAR exhibits a consistent, positive CEUT with a distinct seasonal cycle that peaks during the wintertime. The high wind stress upon the waters at this location produces CEUT of roughly 1.5 m^3/s per meter in summer and about 4 m^3/s per meter in winter. NCEP R2 on the other hand does not have a seasonal cycle in CEUT, but it has a rather constant, equatorward, alongshore wind that produces about 0.5 m^3/s per meter CEUT. With respect to EPT, the location of the wind stress maxima is particularly important. SCOAR reveals a maximum on the coast and weakening of winds within about 100km offshore, which leads to negative EPT (downwelling). The EPT also has a seasonal cycle that ranges between -1.4 (in winter) to -0.2 m^3/s per meter (in summer). NCEP R2 has a similar seasonal and range in magnitude of EPT, but of the opposite sign. This indicates strengthening winds while extending offshore. A seasonal cycle is evident in the total transport for both SCOAR and NCEP R2. During winter, total transport in SCOAR is greater than NCEP R2 by a factor of 1.5 to 2, and only slightly greater by about 10% during summer. This would have implications on the nutrient flux brought to the surface ocean, and affect the nutrient availability for biological production. CEUT contributes about 80% of the total transport in SCOAR, while EPT contributes about 60% of the total transport in NCEP R2. This shows that while both SCOAR and NCEP R2 can induce a similar seasonal cycle in total upwelling transport, the mechanism for the upwelling is different.

Arica is situated at the border of Peru and Chile, on a geographical bend that is characterized by a wind stress minimum. Figure 3.10 reflects a steady, equatorward alongshore wind gives rise to a constant 0.2 m^3/s per meter CEUT in

SCOAR. NCEP R2 shows a seasonal reversal of winds at the coast that induces offshore transport (upwelling) during summer and onshore transport (downwelling) during winter, with CEUT of roughly ± 0.5 m^3/s per meter. NCEP R2 also shows a seasonal cycle in EPT that in contrast to CEUT, produces negative EPT (downwelling) in summer and positive EPT (upwelling) in winter, with EPT magnitude of about ± 0.3 m^3/s per meter. SCOAR has a marginally variable EPT centered around 0.1 m^3/s per meter. As such, the total transport for SCOAR is about 0.3 m^3/s per meter throughout the whole time series. For NCEP R2, the CEUT provides about 70% of the total transport, thereby allowing upwelling (downwelling) favorable conditions during winter (summer). This reflects the importance of the spatial distribution of wind forcing used as it can produce quite different conditions for nutrient flux.

South of Arica, the coastline is orientated north-south over roughly 800km and Taltal provides a typical example for this stretch. For the coastal water off Taltal, a time series of the total wind-driven upwelling transport and its two components are shown in Figure 3.11. In SCOAR, weak winds uniformly blow northwards and produce CEUT of about 0.3 ± 0.1 m3/s per meter. In NCEP R2, a seasonal cycle of the winds bring stronger negative CEUT of about -0.6 m3/s per meter during fall season. In contrast, EPT in this area has a seasonal cycle in SCOAR that ranges between 0.3 to 1.2 m3/s per meter with its peak in summer, while in NCEP R2, it is a more steady 0.3 ± 0.1 m^3/s per meter EPT. As a result, the combined transport in SCOAR produces upwelling favorable conditions throughout, with a seasonal cycle that ranges between 0.5 to 1.5 m^3/s per meter. On the other hand, the total transport in NCEP R2 flips between negative (downwelling favorable conditions) and positive (upwelling favorable conditions). 2000-mid 2003 have generally negative total transport that peak at -0.5 m^3/s per meter during fall. Similarly, 2006-2007 also exhibit negative total transport that peak in winter. As for mid 2003- 2005, total transport in NCEP R2 is about 0.2 ± 0.3 m^3/s per meter. This emphasizes the importance of wind product used to force the ocean, as the difference in wind stress magnitude off Arica and shift in the wind stress maxima has lead to opposite physical conditions for nutrient flux.

Progressing further south to the region of Coquimbo, particularly right off the coast of Tongoy. Within NCEP R2, a seasonal cycle appears in both CEUT and EPT. CEUT are generally negative (onshore transport; downwelling) that peaks at about -1.5 m^3/s per meter in winter and approximately 0.8 m^3/s per meter in summer, while the EPT reaches about 0.6 m^3/s per meter in winter and around -0.3 m^3/s per meter in summer. This results in a seasonal cycle of the total transport in NCEP R2 that provide downwelling favorable conditions during winter and upwelling favorable conditions during summer. As for SCOAR, CEUT is positive throughout with no distinct seasonal cycle but has an annual peak of about 2 m^3/s per meter in spring. EPT is generally negative and without a distinct seasonal cycle either, but there is an annual peak of -0.4 m^3/s per meter in spring too. The combined effect in SCOAR is an erratic, positive total transport (upwelling favorable conditions) centered about 1 ± 0.5 m^3/s per meter. Again, the difference in the magnitude of the wind stress field and shift in the its maxima has led to differing conditions for nutrient flux, with NCEP R2 providing alternating conditions for favorable nutrient flux, while SCOAR consistently provides upwelling favorable conditions for this location.

The southmost headland of the domain is Punta Lavapie, for which changes in the directional flow of winds coincides with the migration of the subtropical high that brings westerly winds during fall and winter and southwesterly winds in spring and summer. This leads to a seasonal cycle in CEUT for SCOAR that allows for upwelling favorable CEUT of about 0.7 m^3/s per meter in spring and summer, and small negative (almost zero) CEUT transport in fall and winter. EPT for SCOAR is positive and centered at 0.2 ± 0.2 m^3/s per meter, without any seasonal cycle. The sum total transport in SCOAR shows a clear seasonal cycle with summer peaks of approximately 1.5 m^3/s per meter and nearly zero during fall and winter. EPT contributes roughly 30% to the total, summertime, upwelling favorable transport. For NCEP R2, there are distinct seasonal cycles seen in CEUT and EPT that are out of phase. The magnitudes of CEUT peaks are a factor of -1.5 to -2 greater than EPT. CEUT of roughly 2.5 m^3/s per meter provides upwelling favorable conditions during summer and approximately -1.8

m^3/s per meter in winter supports downwelling favorable conditions. As for EPT, an average of 1 m^3/s per meter in winter is suitable for upwelling, while -1.1 m^3/s per meter in summer is conducive for downwelling. The total wind driven transport in NCEP R2 is surprisingly similar to SCOAR, with about 1.5 m^3/s per meter peaks in summer that favor upwelling conditions, and more negative transports (compared to SCOAR) of around -0.5 m^3/s per meter in winter. Even though the total transport in SCOAR and NCEP R2 are comparable in this case, this suggests caution for attributing upwelling to a particular mechanism.

In all, the good agreement of the spatial distribution and magnitude of the wind fields seen in SCOAR and observations reveals the ability of SCOAR to downscale NCEP R2 winds well. Comparison of SCOAR winds to NCEP R2 winds along coastal regions show the differences of their influence on wind-driven upwelling variability and thus the importance of wind products used to force ocean models. The total upwelling transport in SCOAR and NCEP R2 have seasonally opposite signs at Taltal, Tongoy (Coquimbo) and Arica, which reflects the importance of the spatial distribution of wind forcing used. In particular, near the coast where differences in wind stress magnitude and location of wind stress maxima, which in turn affects wind stress curl fields, can greatly influence the wind-driven upwelling processes and thus affect at least one factor of nutrient flux. At San Juan and Punta Lavapie, where the seasonal cycle in total upwelling transport is similar and comparable in magnitude, spatial pattern of wind forcing still play an important role in distinguishing the wind-driven upwelling process that support the upwelling conditions.

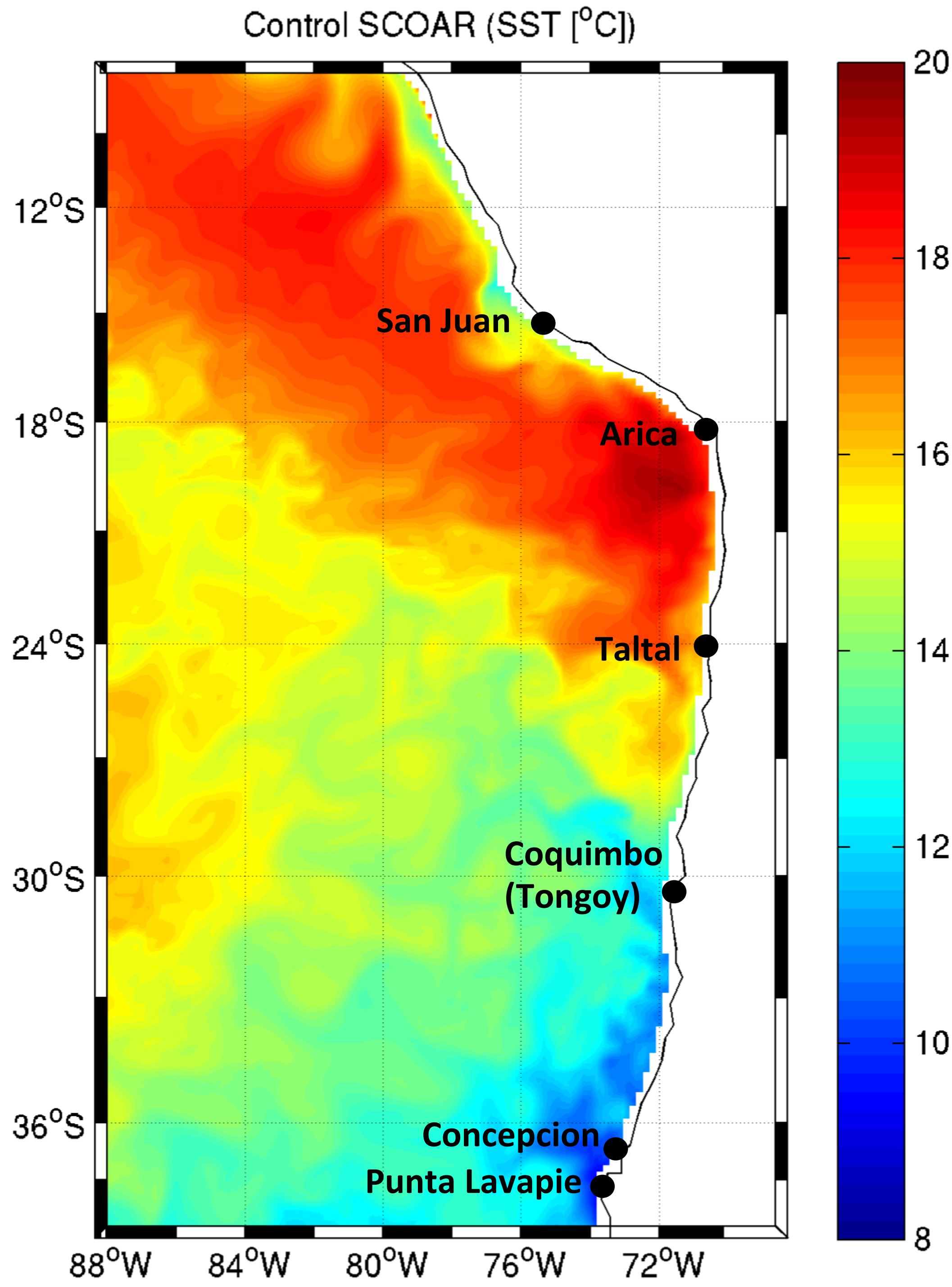

Figure 3.1: Averaged SST distribution for April 2007 based on Control SCOAR, with names of particular coastal locations along Peru and Chile.

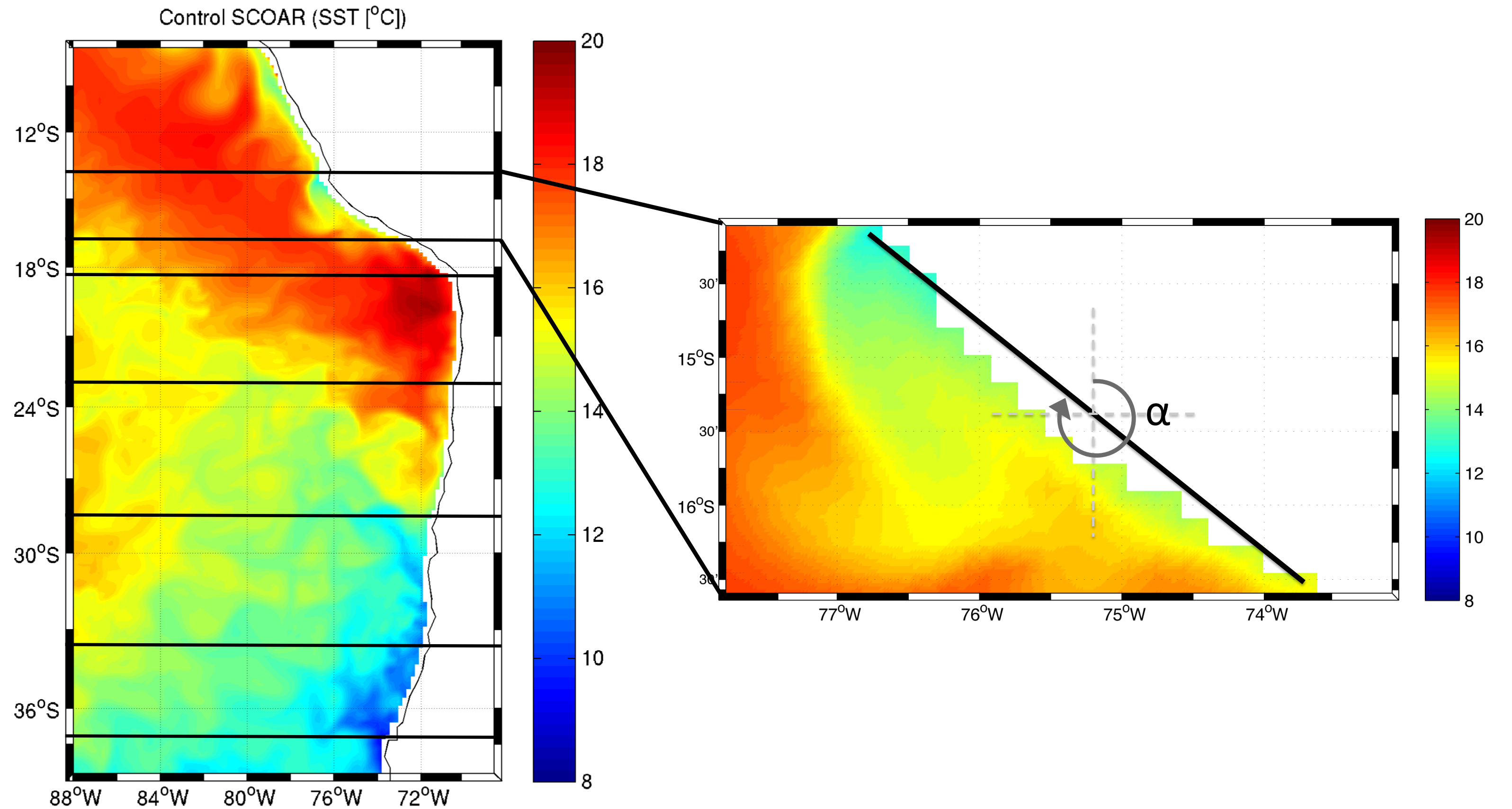

Figure 3.2: Left panel: Division of zones to fit a straight line along each coastal zone. Right panel: Zoom-in view of one zone to show the straight line fitted to the coast and the coastal slope bearing, α.

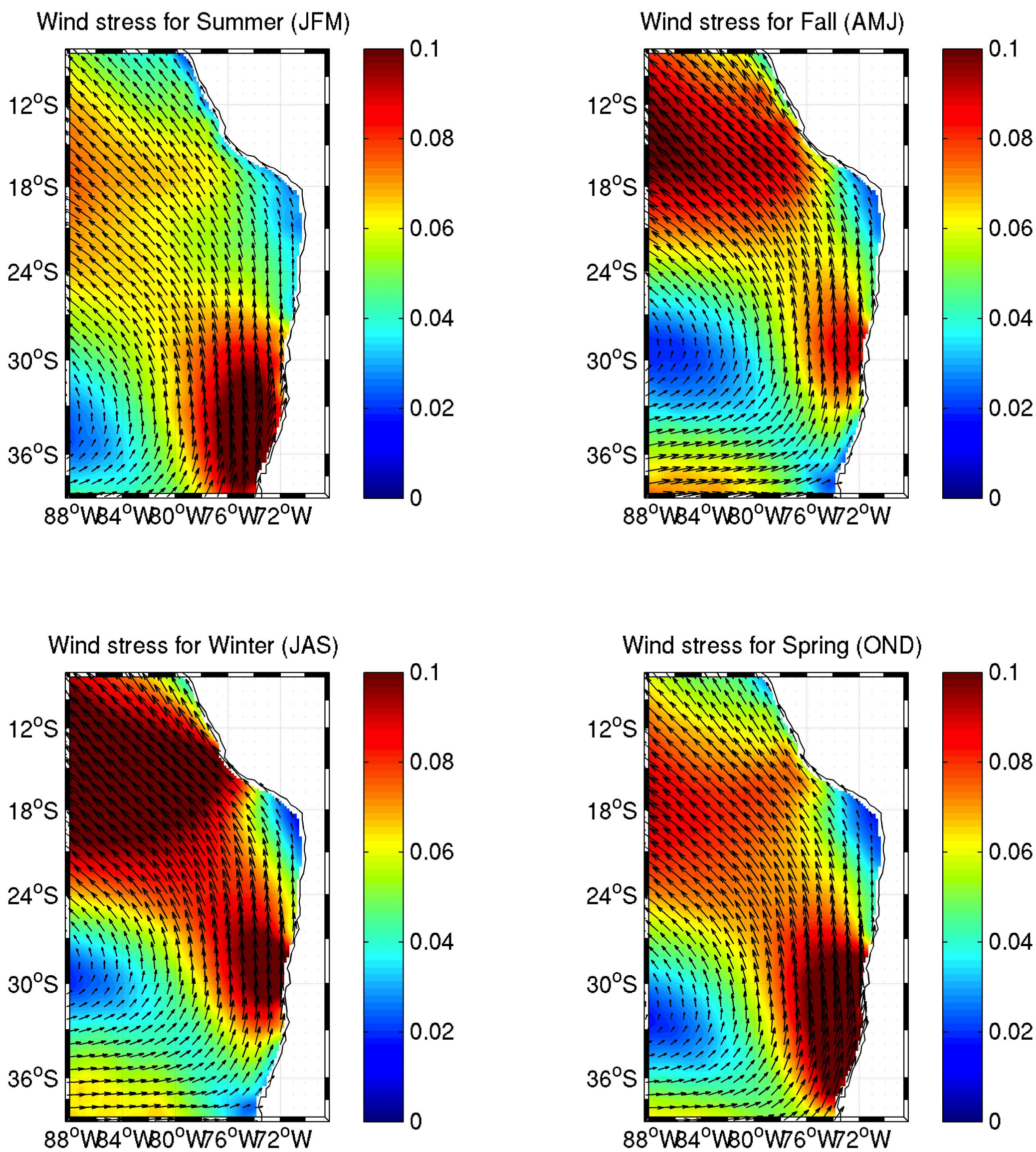

Figure 3.3: Seasonal wind stress field (N/m^2) derived from satellite observations over the HCS region averaged from 2000-2007. Austral summer (JFM; top left), fall (AMJ; top right), winter (JAS; bottom left), and spring (OND; bottom right).

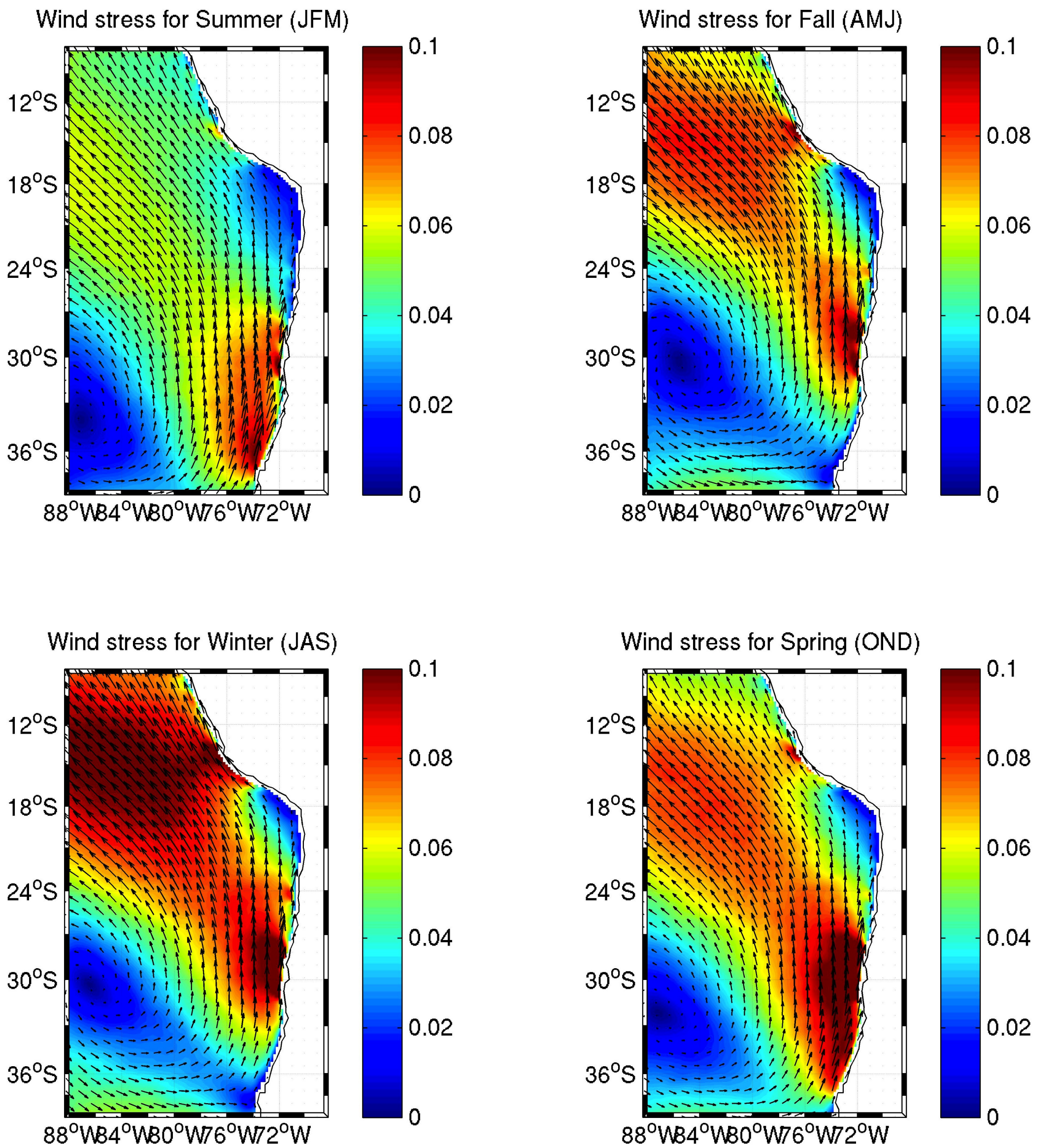

Figure 3.4: Seasonal wind stress field (N/m^2) over the HCS region averaged from 2000-2007 for SCOAR. Austral summer (JFM; top left), fall (AMJ; top right), winter (JAS; bottom left), and spring (OND; bottom right).

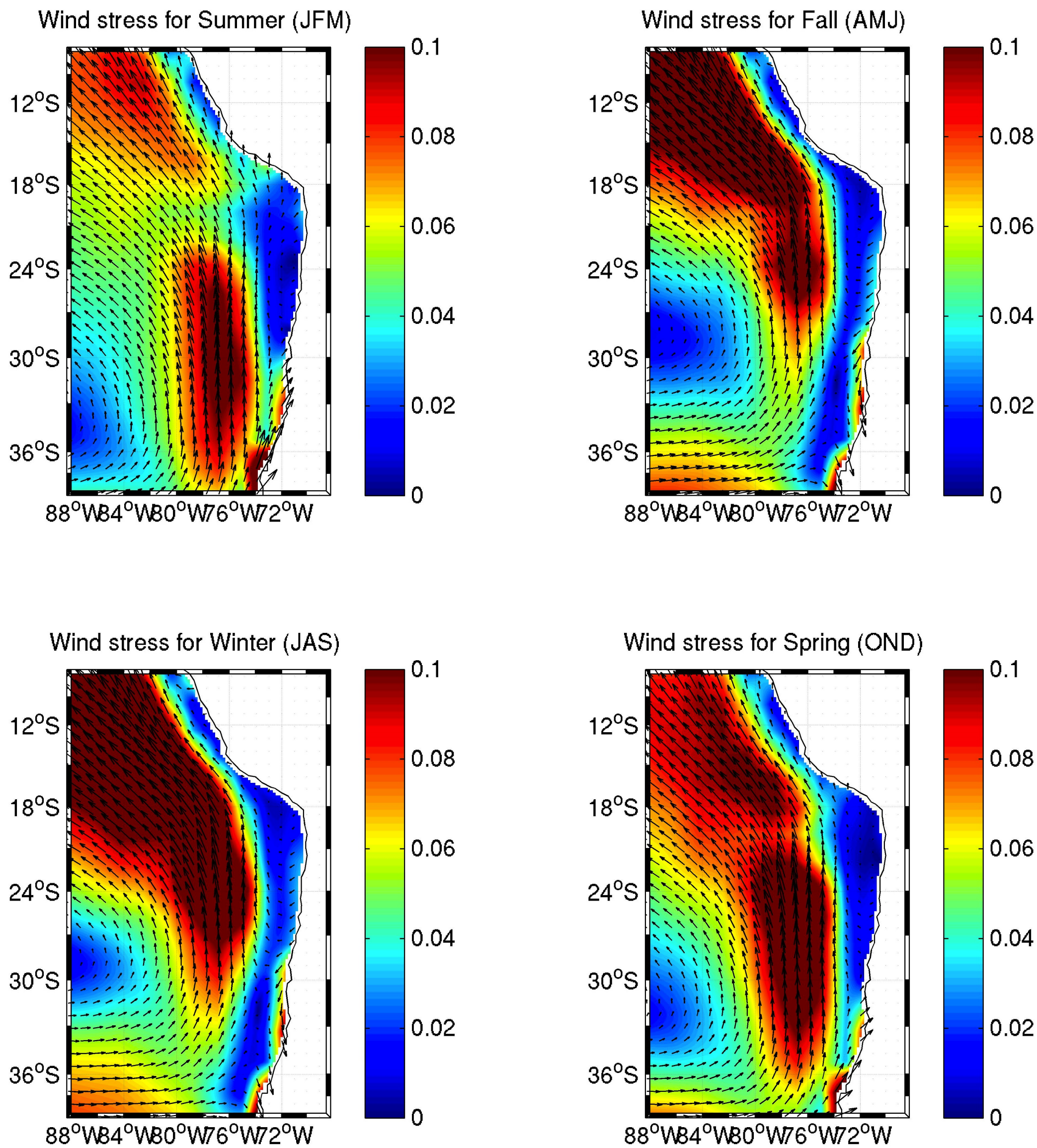

Figure 3.5: Seasonal wind stress field (N/m^2) based on NCEP R2 over the HCS region averaged from 2000-2007. Austral summer (JFM; top left), fall (AMJ; top right), winter (JAS; bottom left), and spring (OND; bottom right).

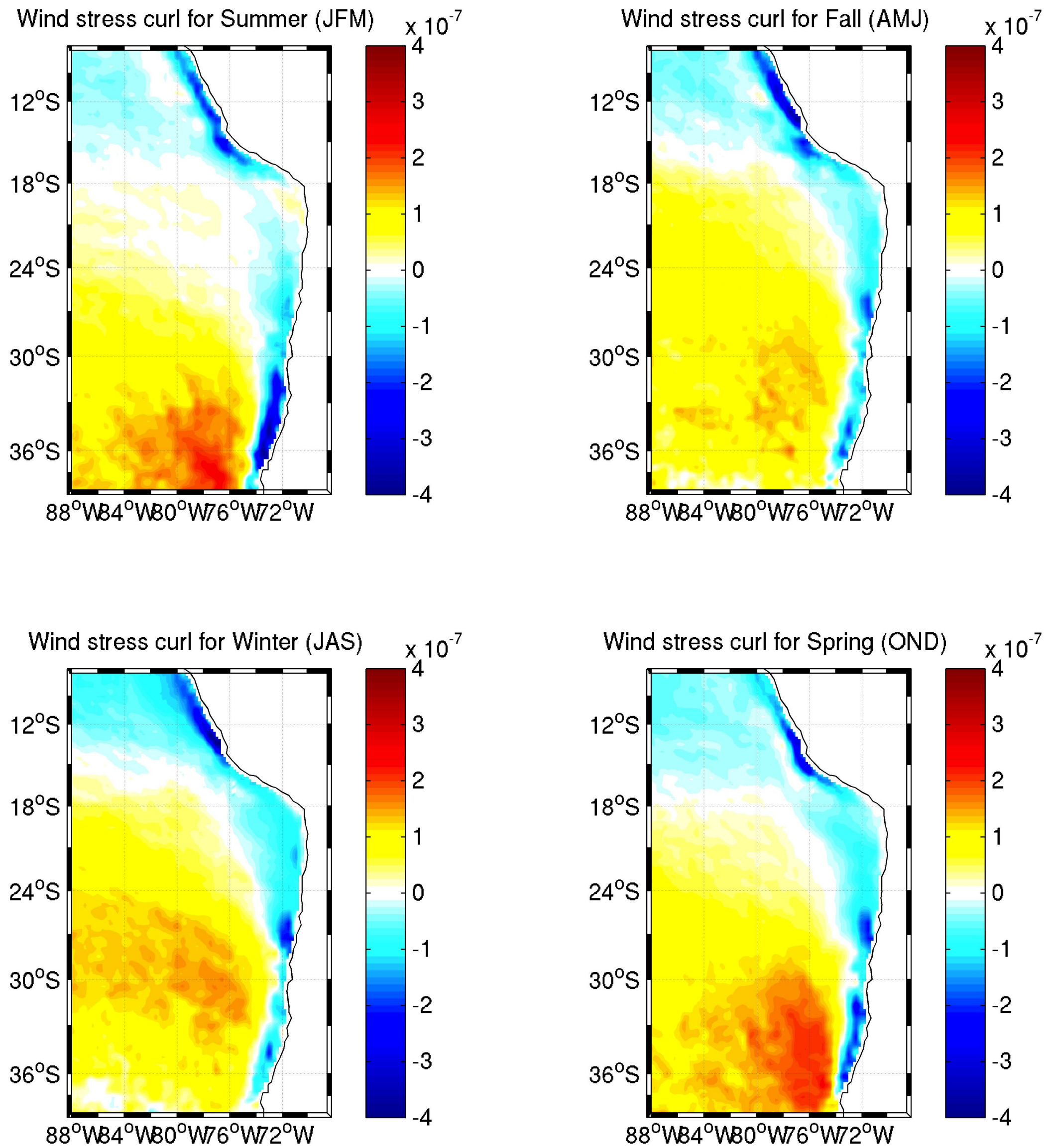

Figure 3.6: Seasonal wind stress curl field (N/m^2 per m) derived from satellite observations over the HCS region averaged from 2000-2007. Austral summer (JFM; top left), fall (AMJ; top right), winter (JAS; bottom left), and spring (OND; bottom right).

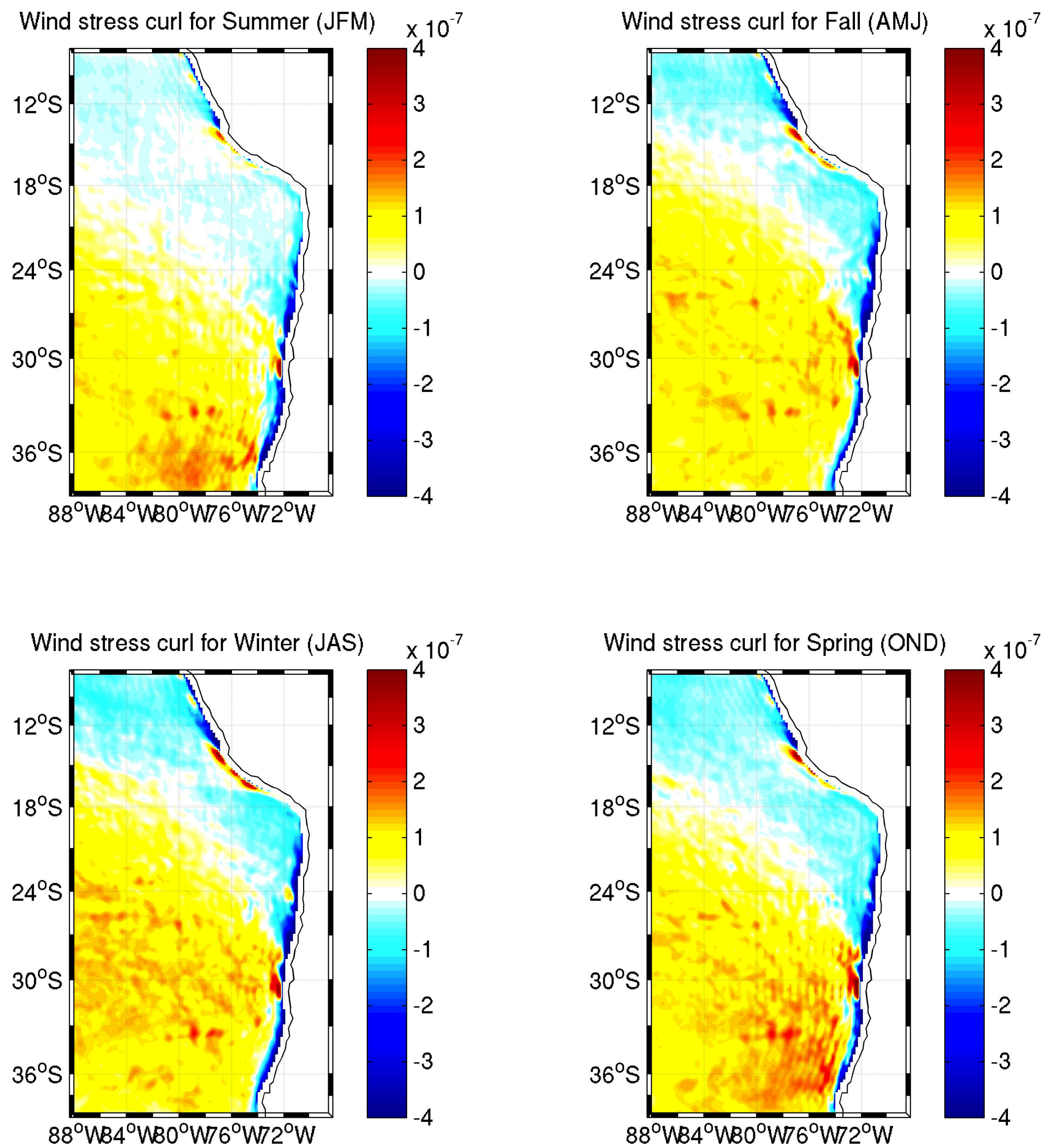

Figure 3.7: Seasonal wind stress field (N/m^2 per m) over the HCS region averaged from 2000-2007 for SCOAR. Austral summer (JFM; top left), fall (AMJ; top right), winter (JAS; bottom left), and spring (OND; bottom right).

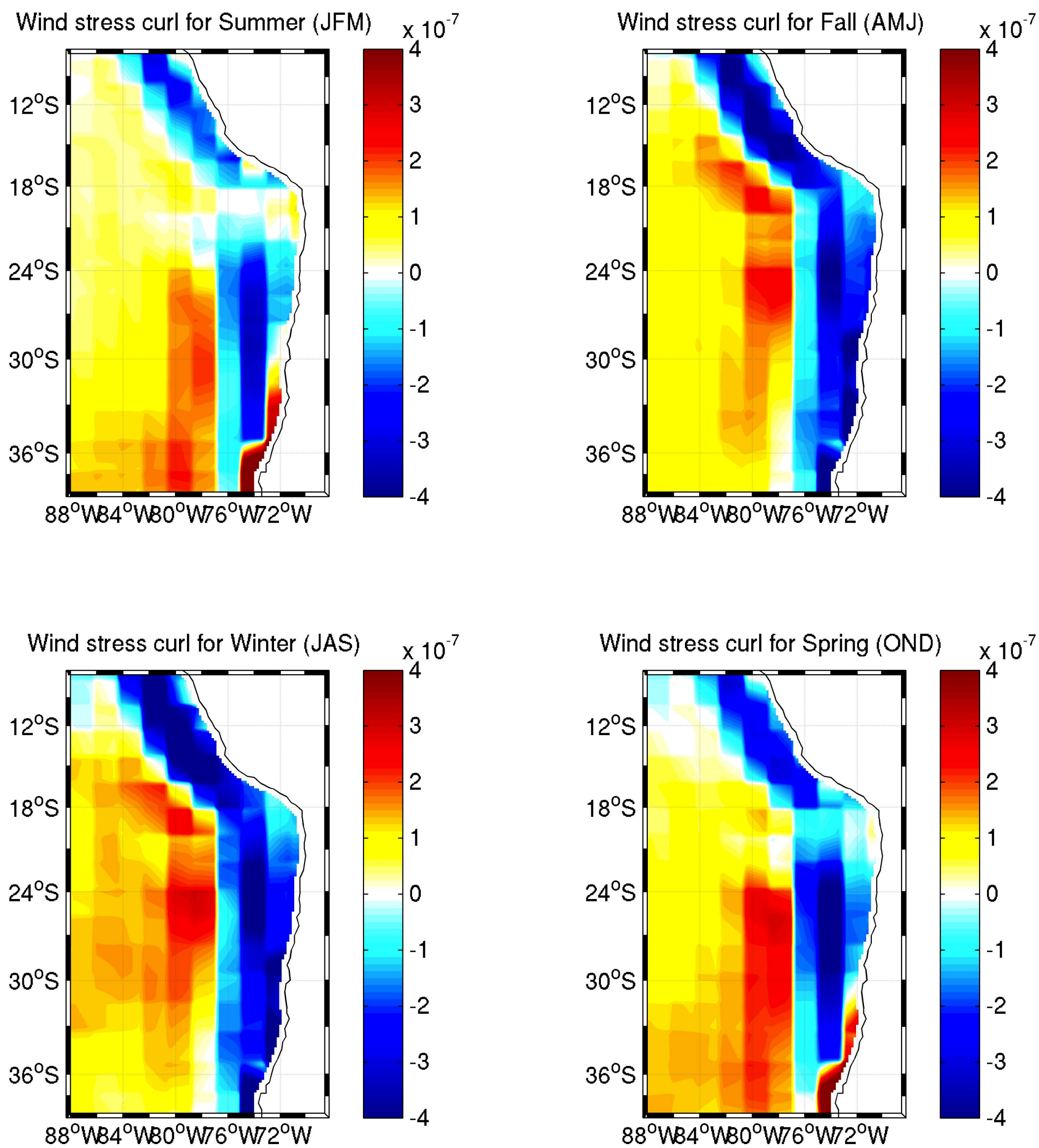

Figure 3.8: Seasonal wind stress field (N/m^2 per m) based on NCEP R2 over the HCS region averaged from 2000-2007. Austral summer (JFM; top left), fall (AMJ; top right), winter (JAS; bottom left), and spring (OND; bottom right).

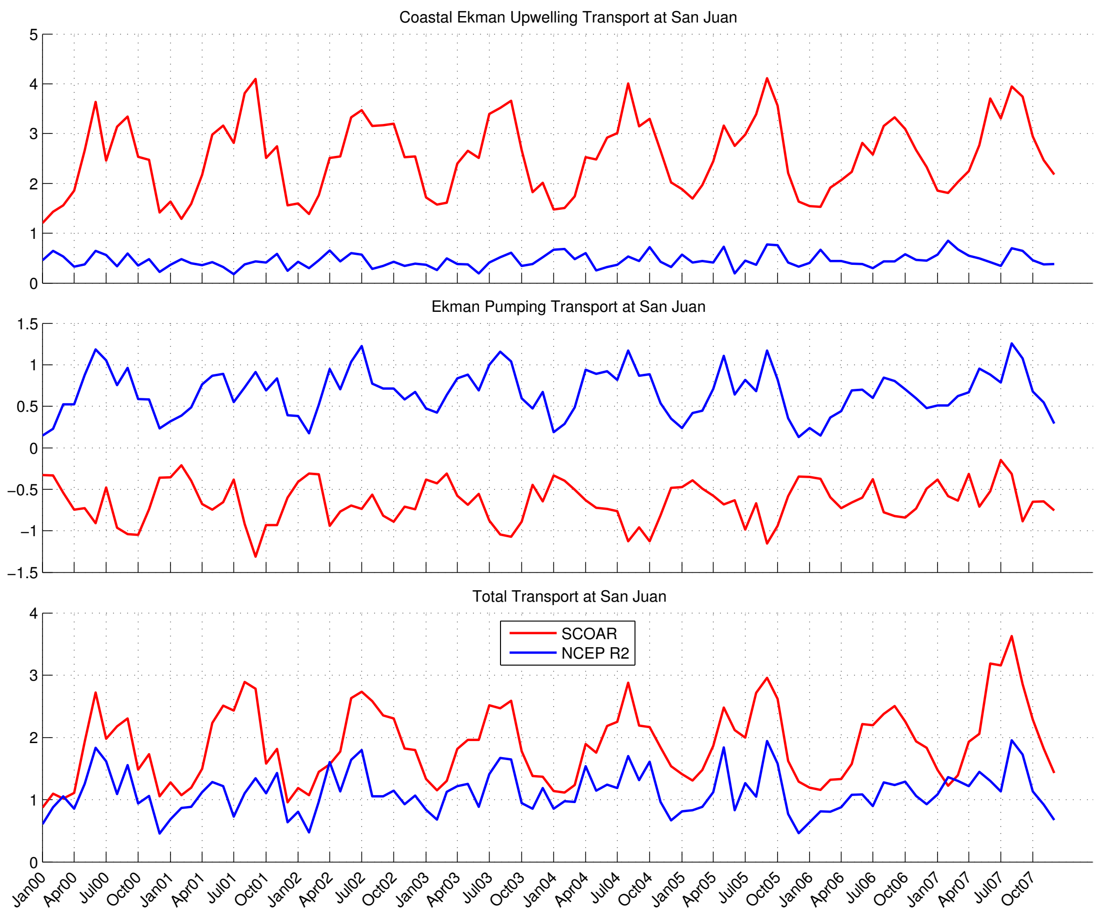

Figure 3.9: Time series of coastal Ekman upwelling transport (top), Ekman pumping transport (middle) and total wind-driven upwelling transport (bottom) at San Juan based on SCOAR (red) and NCEP R2 (blue) over the time period of 2000-2007. Transport are in units of m^3/s per meter of coast

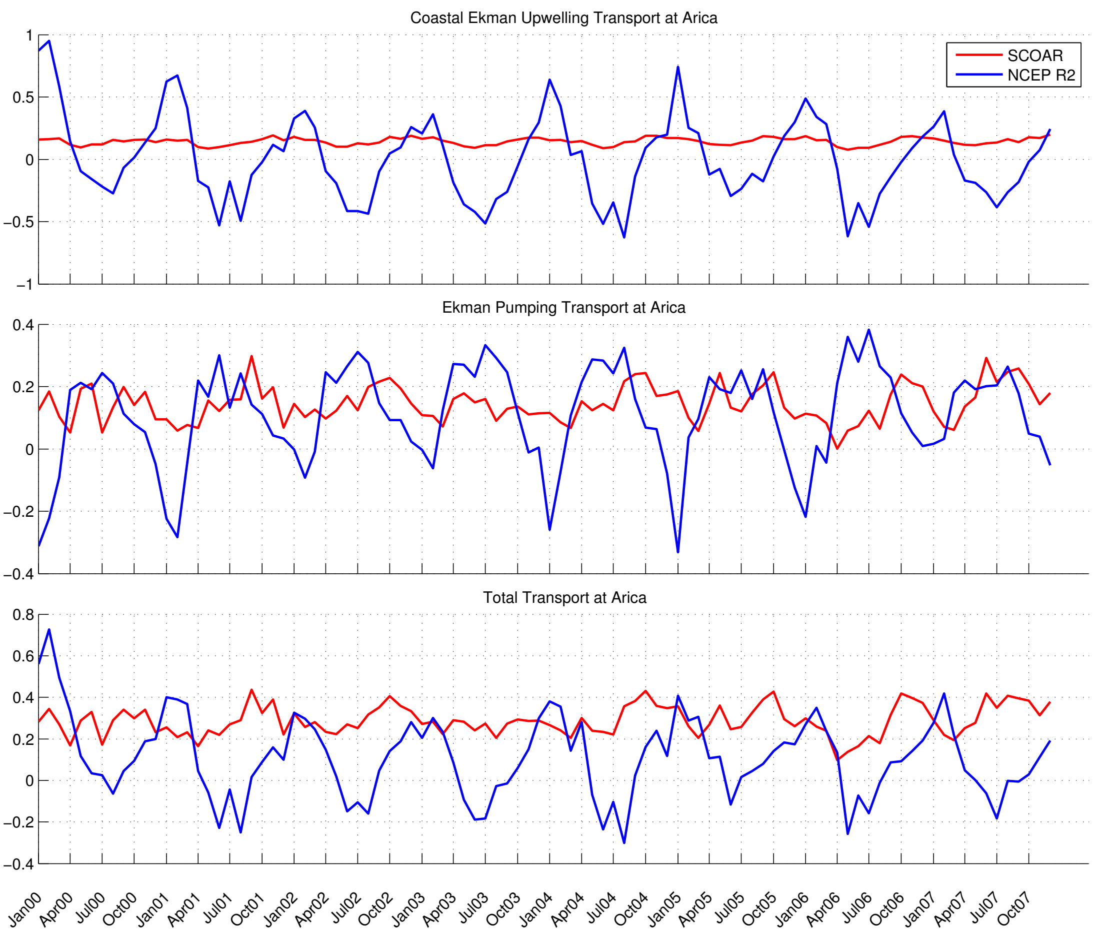

Figure 3.10: Same as Figure 3.9 but for the coastal water off Arica.

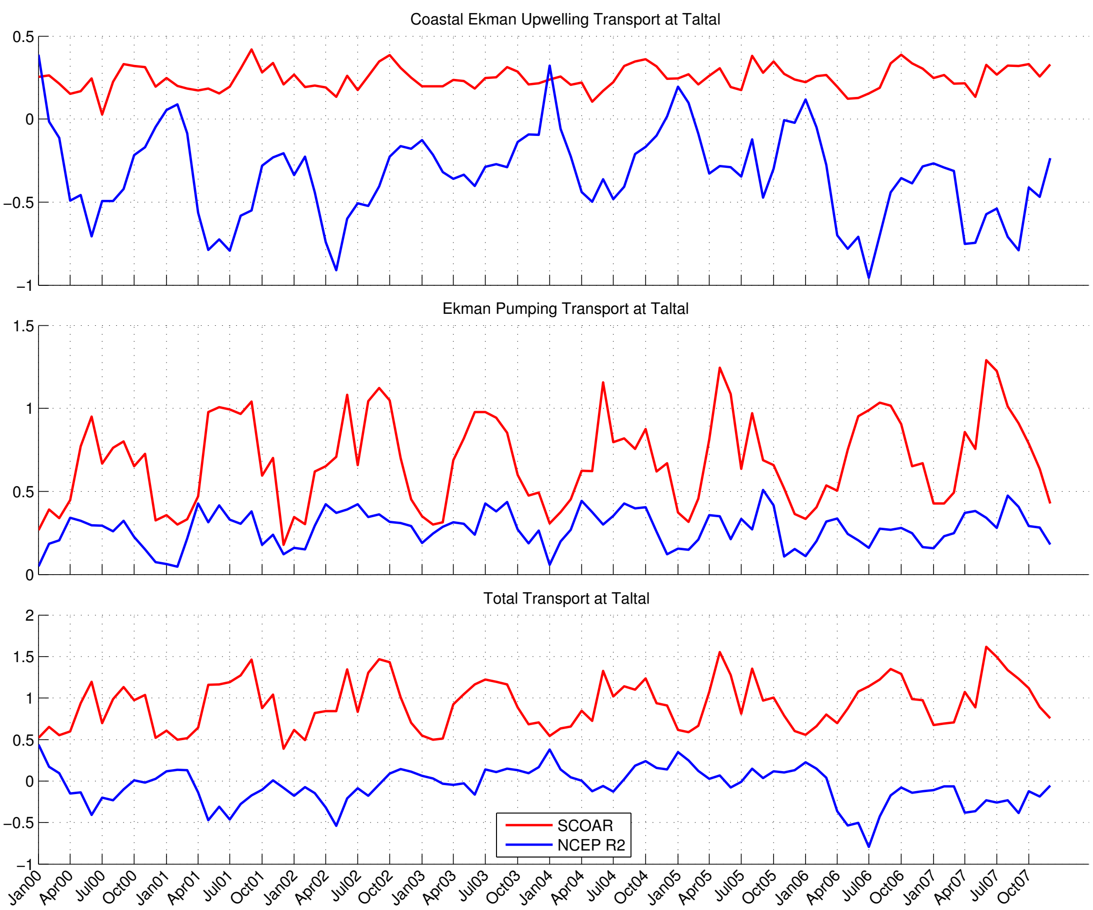

Figure 3.11: Same as Figure 3.9 but for the coastal water off Taltal.

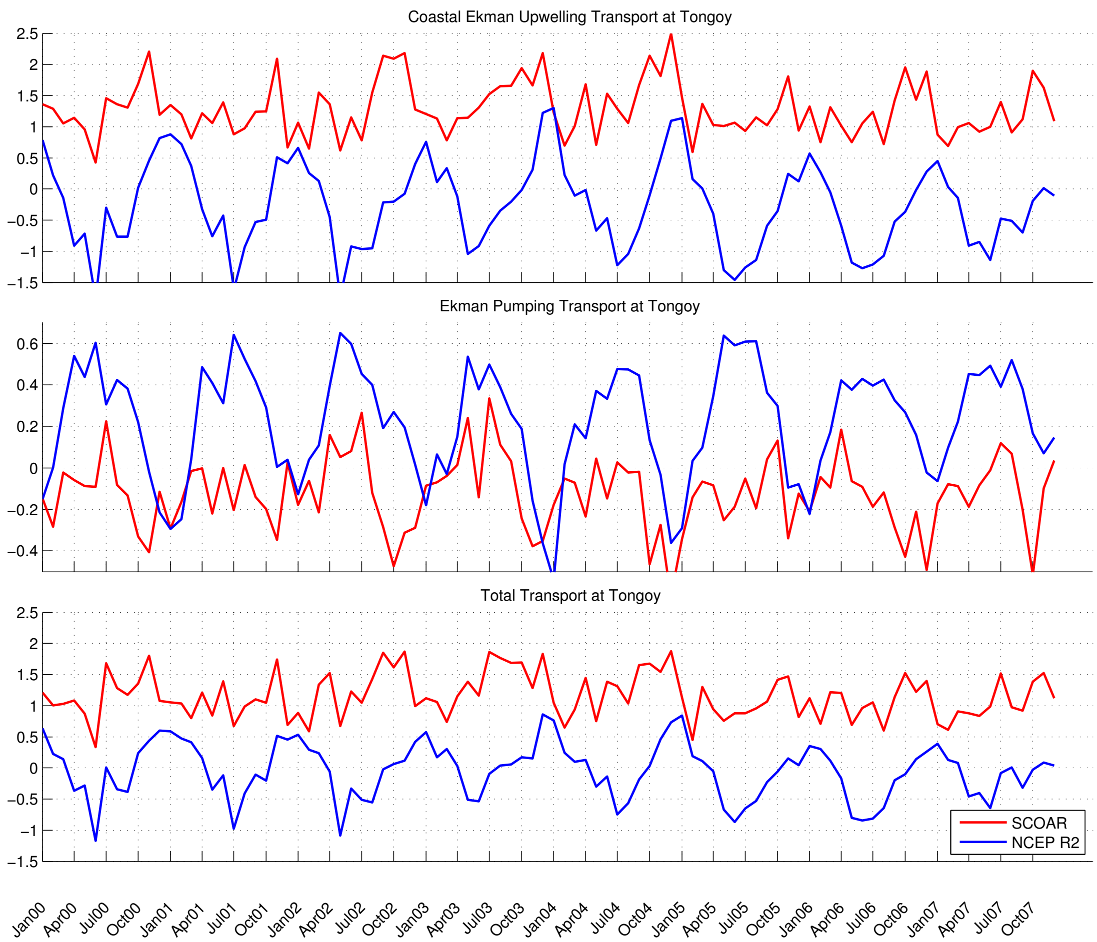

Figure 3.12: Same as Figure 3.9 but for the coastal water off Tongoy.

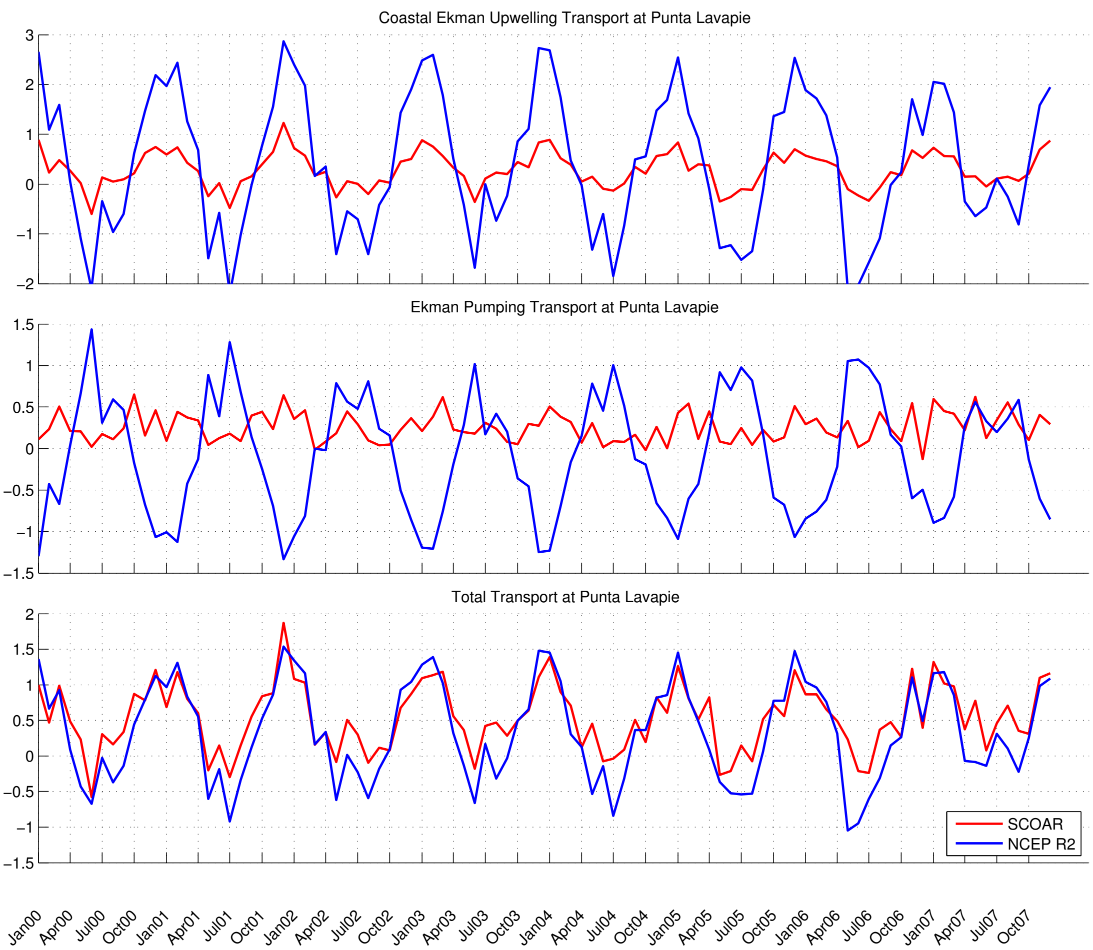

Figure 3.13: Same as Figure 3.9 but for the coastal water off Punta Lavapie.

3.2 Air-sea interaction of coastal water off Peru

Many observations have shown strong influence of mesoscale sea surface temperature (SST) patterns on wind stress fields over the global ocean, whereby areas with colder SST or cold filaments are generally overlaid with wind stress minima and places with warmer SST covary with strong wind stress (Xie, 2004; Chelton et al., 2001; Veechi et al., 2004; Small et al., 2008). Such SST-wind coupling dynamics is described very well in (Wallace et al., 1989). Over warmer SST, the atmospheric boundary layer (ABL) is less stable, thereby inducing vertical mixing that deepens the BL and brings momentum from aloft to the surface and accelerates the winds on the surface. Over colder SST, the ABL is more stable and vertical shear is enhanced, which leads to decreased vertical mixing and thinning of the ABL, thereby decelerating the surface winds (Samelson et al., 2006).

In regions with strong SST gradients, this idea can be extrapolated to see its impact on wind stress fields, namely wind stress derivatives. Figure 3.14 illustrates these mechanisms, which where first described by Chelton et al. (2001). When winds blow along the isotherms, on the warmer SST side they strengthen and exert a higher wind stress and on the cooler side they weaken to exert lower wind stress, thereby inducing a wind stress curl associated with the crosswind component of the SST gradient. When the winds blow along the SST gradient, e.g. from colder to warmer waters, lower wind stress is exerted over colder waters and higher wind stress over warmer waters, inducing a wind stress divergence associated with the downwind component of the SST gradient. Likewise, if winds are blowing from warmer to colder waters, then a wind stress convergence associated with the downwind component of SST gradient is generated.

Quantification of air-sea coupling using SST gradients and wind stress derivatives has been widely accomplished with many satellite observations over the world's ocean, including the Gulf Stream, California Current System, Agulhas Return Current, tropical Atlantic Ocean, and the Antarctic Circumpolar Current (Chelton et al. (2004, 2007); O'Neill et al. (2003, 2005)). However, such analysis has not been performed over the Southeast Pacific region, particularly just off the coast of Peru and Chile, because it was thought to exhibit only weak coupling.

This region, however, is vitally important to global climate because of its effect on the Walker Cell, which controls both the mean state of the tropical Pacific and ENSO variability in key ways. Even weak feedbacks between mesoscale ocean variability and the atmosphere in this region could have profound influences on global climate.

Ocean-atmosphere coupling in the HCS are identified through satellite observations and SCOAR. Satellite-derived SST products are obtained from the fusion of Tropical Rainfall Measuring Mission (TRMM) Microwave Imager (TMI) data, which is available from November 1997 (Wentz et al., 2000), and from the Advanced Microwave Scanning Radiometer on the Earth Observing System (EOS) Aqua satellite (AMSR-E) data, that available from May 2002 (Wentz and Meissner, 2000; Chelton and Wentz, 2005). Both TMI and AMSRE data have been combined and optimally interpolated to give daily SST products at 0.25° resolution (Reynolds et al., 2004). This data is available on the Remote Sensing Systems (RSS). Wind stress products are derived from the Quick Scatterometer (QuikSCAT) satellite (Freilich et al., 1994; Liu, 2002), that was in operation from July 1999 till November 2009. It has a 0.5° resolution, and is also available through RSS.

The fully-coupled SCOAR model with a daily coupling is used for this study and is here forth denoted as Control SCOAR. In experimental simulations that attempt to remove the mesoscale SST impact on the air-sea coupling, an online, 2.5-degrees, 2-D spatial lowess filter is applied to the SST field that forces RSM at each coupling step (daily). In this case, it is called Smoothed SCOAR, which represents large-scale coupling. This procedure allows large-scale SST coupling to be preserved while extinguishing the mesoscale eddy impacts on the overlying atmosphere. Note that the eddy circulation in the ocean is not smoothed and full coupling still occurs in these runs. Through this strategy, ocean-atmosphere coupling on the full scale (inclusion of the large scale and mesoscale) and only on the large scale can be assessed and used to understand the relative roles of large-scale coupling and mesoscale coupling on full-scale coupling.

Using TMI-AMSRE SST data and QSCAT wind stress fields for 2003-2007, monthly downwind SST gradient and crosswind SST gradient, along with corresponding wind stress divergence and convergence are computed. These calculations are also performed with the outputs from Control SCOAR and Smoothed SCOAR. Figure 3.15 shows an example of wind stress divergence (in colors) overlaid with contours of downwind SST gradients averaged over April 2007, for Control SCOAR, Smoothed SCOAR and satellite observations respectively. Both Control SCOAR as well as satellite observations provide a prominent example of downwind SST underlying wind stress divergence, and vice versa, on the oceanic mesoscale. In Smoothed SCOAR, some overlay exists, but it is not as distinct as Control SCOAR, suggesting that smoothing SST fields would reduce the coupling.

For a better quantification of the air-sea coupling, bin scatter plots (Fig. 3.16) of the wind stress divergence against downwind SST gradient is created, and a linear regression is performed on the mean of the each bin (Xie, 2004; Chelton et al., 2004). The error bars show one standard deviation of the wind stress divergence for each bin. The slope of the linear fit (hereon called the coupling coefficient, s_d), with its associated standard error and r^2 coefficient are all evaluated for each case. For April 2007, the coupling coefficients are found to be s_d=0.9±0.2 for Control SCOAR, s_d=0.1±0.3 for Smoothed SCOAR, s_d=1.2±0.1 for satellite observations. Control SCOAR produces a comparable coupling coefficient to satellite observations, while Smoothed SCOAR does not have the coupling which indicates the importance of the mesoscale to the air-sea coupling.

These calculations are then extended for each month in 2003-2007. The monthly coupling coefficients (s_d) for Control SCOAR (red) and satellite observations (black) along with their confidence intervals measured by the standard error are plotted on Fig. 3.17. s_d is considered significant if its associated r^2 coefficient is greater than 0.6 and p-value (based on students t-test) is less than 0.05. If this criteria is not met, s_d is considered insignificant (green dots) and their standard errors are not shown. Since Smoothed SCOAR produces s_d that are all flagged by this criteria, they have been omitted from the figure. The results reveal a seasonal pattern to the air-sea coupling coefficients in Control SCOAR (red) and satellite observations (black). Satellite observations indicate stronger coupling in austral summer and fall, while Control SCOAR shows stronger coupling in austral fall and winter. While s_d are comparable in most austral fall months, the model does not capture the seasonal cycle predicted by observations. As for Smoothed SCOAR, coupling is insignificant, reinforcing the role of the oceanic mesoscale on the coupling of downwind SST gradient and wind stress divergence. Observation based s_d evaluated in HCS is weaker than its counterpart in the California Current System (CCS) by roughly a factor of 0.5 in summer months (Chelton et al., 2007), suggesting air-sea coupling is not strong in the HCS.

In a similar fashion, the coupling between crosswind SST gradients and wind stress curl (Chelton et al., 2001, 2004) is analyzed. Figure 3.18 shows a colormap of the wind stress curl (N/m^2 per 10000km) overlaid with contours of crosswind SST gradients averaged over April 2007, for Control SCOAR, Smoothed SCOAR and satellite observations respectively. Likewise, it can be seen that both Control SCOAR and satellite observations have indications for air-sea coupling. Performing the linear fit to the bin scatter plot (Fig. 3.19), coupling coefficients (s_c) for crosswind SST gradients to wind stress curl are found to be s_c=0.7±0.1 with r^2 correlation of 0.8 for Control SCOAR, s_c=0.5±0.1 (r^2=0.5) for Smoothed SCOAR, s_c=0.7±0.1 (r^2=0.8) for satellite observations. Like the previous analysis, Smoothed SCOAR indicates the importance of oceanic mesoscale on air-sea coupling. The calculations are extended through 2003-2007 which reveals a seasonal cycle of the air-sea coupling in Control SCOAR and satellite observations (Fig. 3.20). Observations derived air-sea coupling show peaks in austral summer seasons and usually extending to April. However, air-sea coupling based on Control SCOAR have significant coupling in austral winter seasons. While positive s_c values between Control SCOAR and observations are comparable, the model is unable to capture the seasonal cycle in this case either. Air-sea coupling (s_c) in Smoothed SCOAR is found to be mostly insignificant (flagged with r^2 <0.6) and thus not plotted in Fig. 3.20. Again suggesting that ocean mesoscale plays an important role in the coupling of crosswind SST gradient with wind stress curl. For summer months, s_c from observations are approximately a factor of 0.6 lower than those found in CCS (Chelton et al., 2007), which continues with the idea that

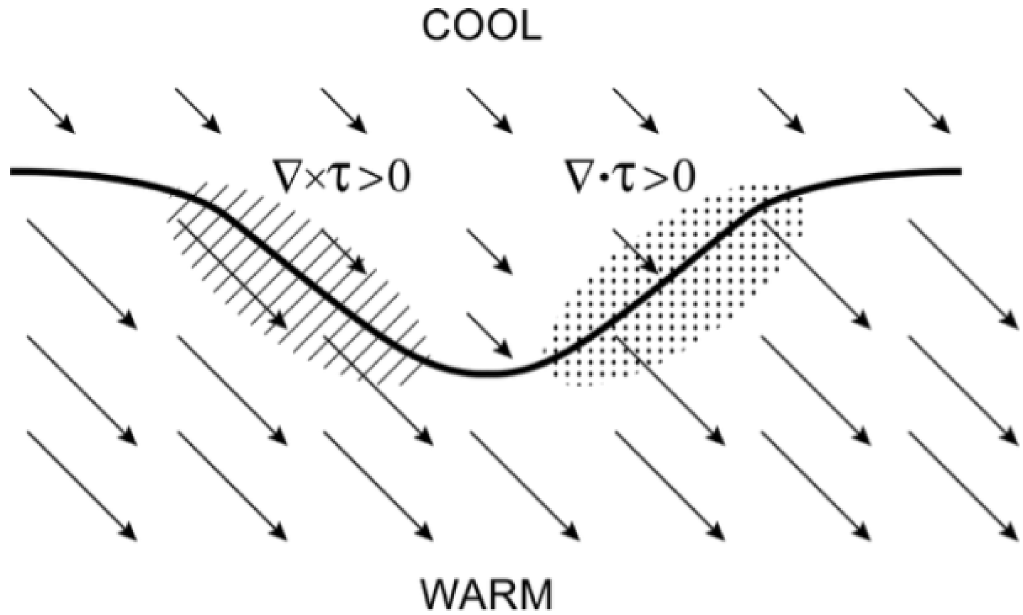

Figure 3.14: Illustration of the influence of SST on overlying surface winds in the vicinity of a meandering SST front from *Chelton et al., 2007*. The magnitude of wind stress are represented by the length of the vectors. They are weaker over cool water and stronger over warm water, which leads to the generation of wind stress divergence and curl. Winds blowing parallel to the isotherms (hatched region) generates strongest wind stress curl and winds blowing perpendicular to the isotherms (stippled regions) induces strongest wind stress divergence.

the intensity of air-sea coupling in the HCS is rather weak.

In short, the Control SCOAR produces comparable seasonal coupling coefficients to those observed in satellite observations. However, Smoothed SCOAR (large-scale coupling) does not produce any significant SST-wind stress coupling throughout the whole run. This shows the critical role of mesoscale coupling to produce any ocean-atmosphere coupling seen in Control SCOAR (full-coupled mode).

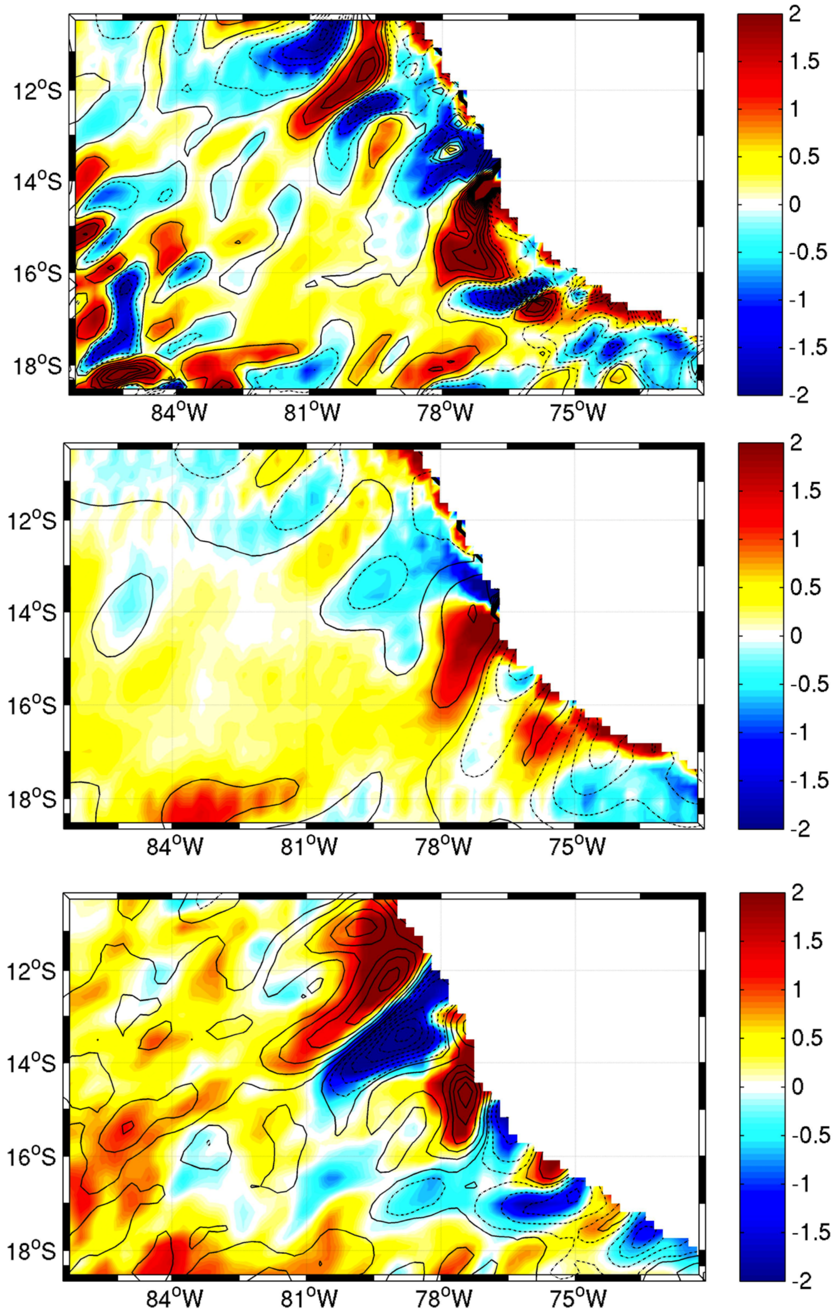

Figure 3.15: Colormap of wind stress divergence (N/m^2 per 10000km) averaged for April 2007, overlaid with contours of downwind SST gradients (°C per 100km) over the Peru domain for Control SCOAR, Smoothed SCOAR and satellite observations. Solid (dashed) contours indicate positive (negative) downwind SST gradients at 0.4°C per 100km intervals. The Peru region covers 86°W-72°W, 10°S-18°S.

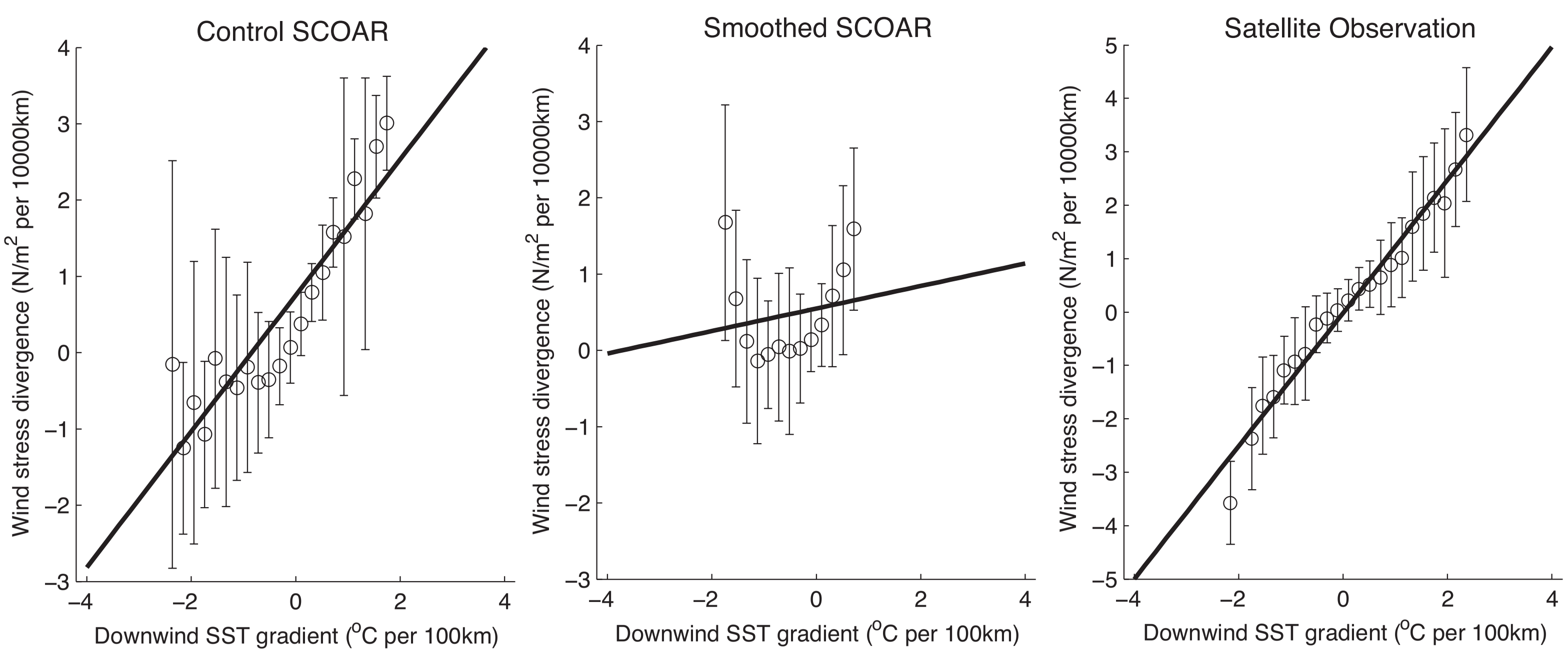

Figure 3.16: Bin scatter plot of wind stress divergence (N/m^2 per 10000km) against downwind SST gradients (°C per 100km), averaged for April 2007 over the Peru domain for Control SCOAR, Smoothed SCOAR and satellite observations. Error bars are one standard deviation of wind stress divergence in each bin.

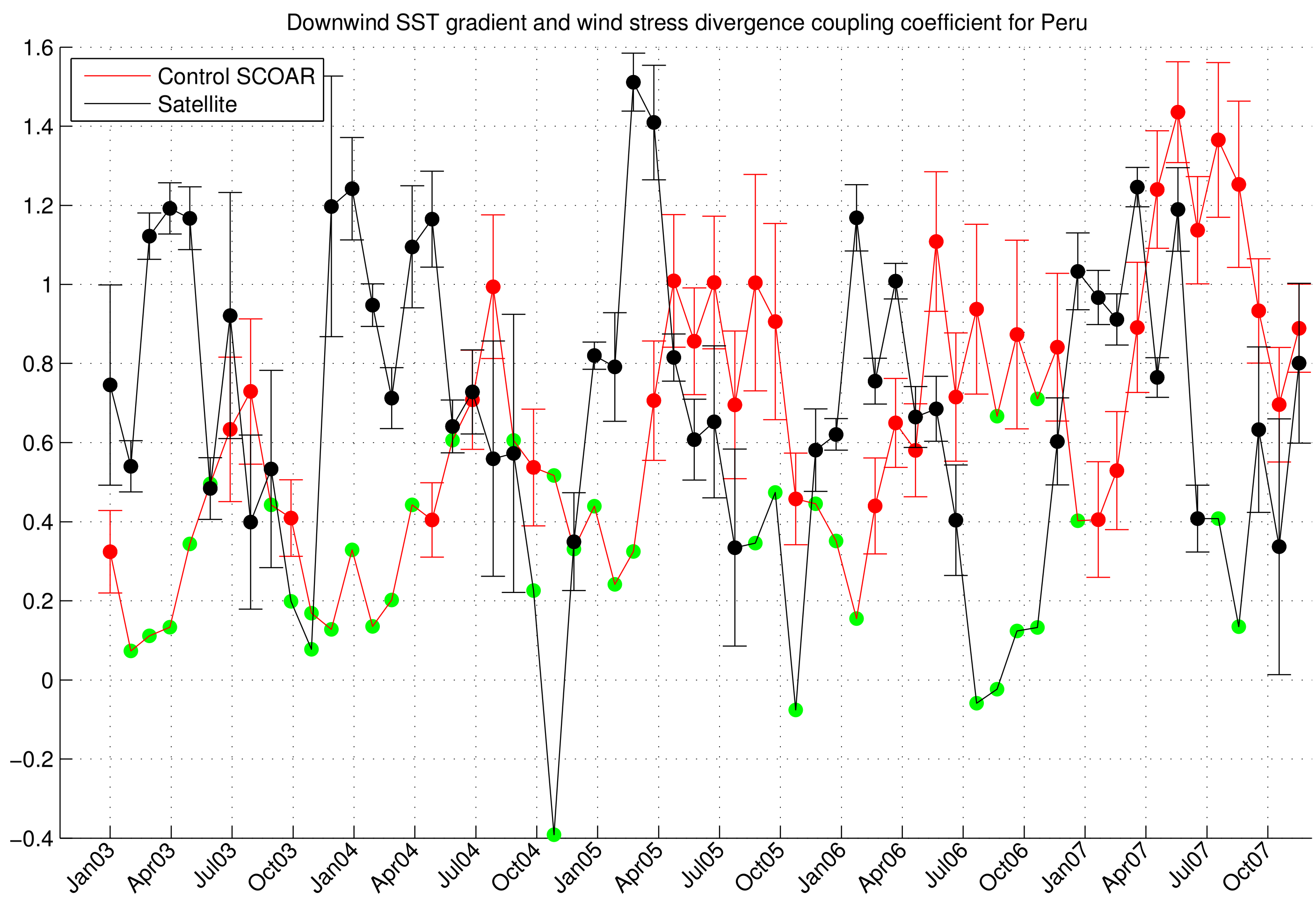

Figure 3.17: Time series of monthly coupling coefficients (s_d,) over the Peru domain for Control SCOAR (red) and satellite observations (black). Green dots indicate that the slopes have r^2 correlation less than 0.6 and/or p-values greater than 0.05. Error bars are standard errors of the slopes.

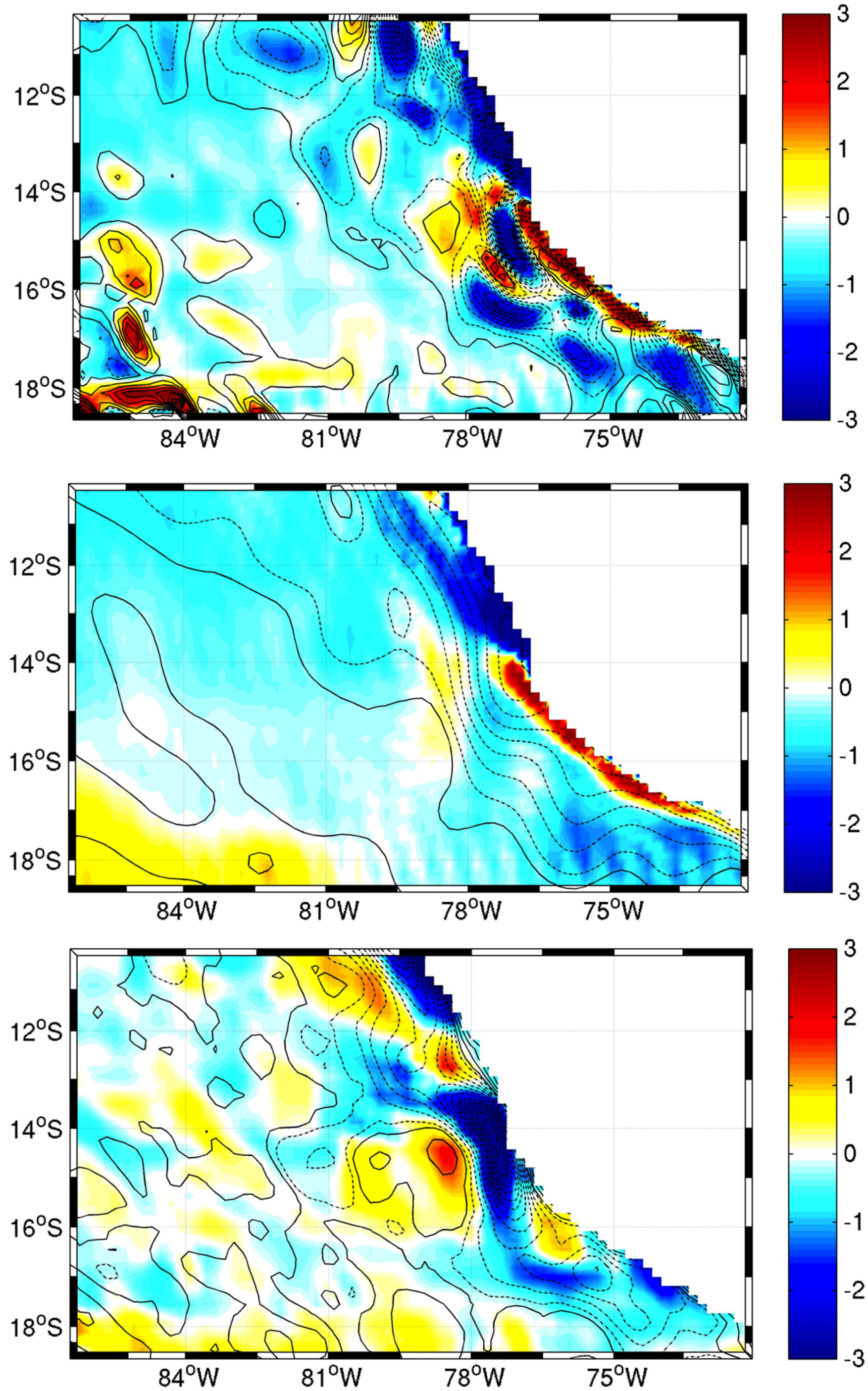

Figure 3.18: Colormap of wind stress curl (N/m^2 per 10000km) averaged for April 2007, overlaid with contours crosswind SST gradients (°C per 100km) over the Peru domain for Control SCOAR, Smoothed SCOAR and satellite observations. Solid (dashed) contours indicate positive (negative) crosswind SST gradients at 0.4°C per 100km intervals.

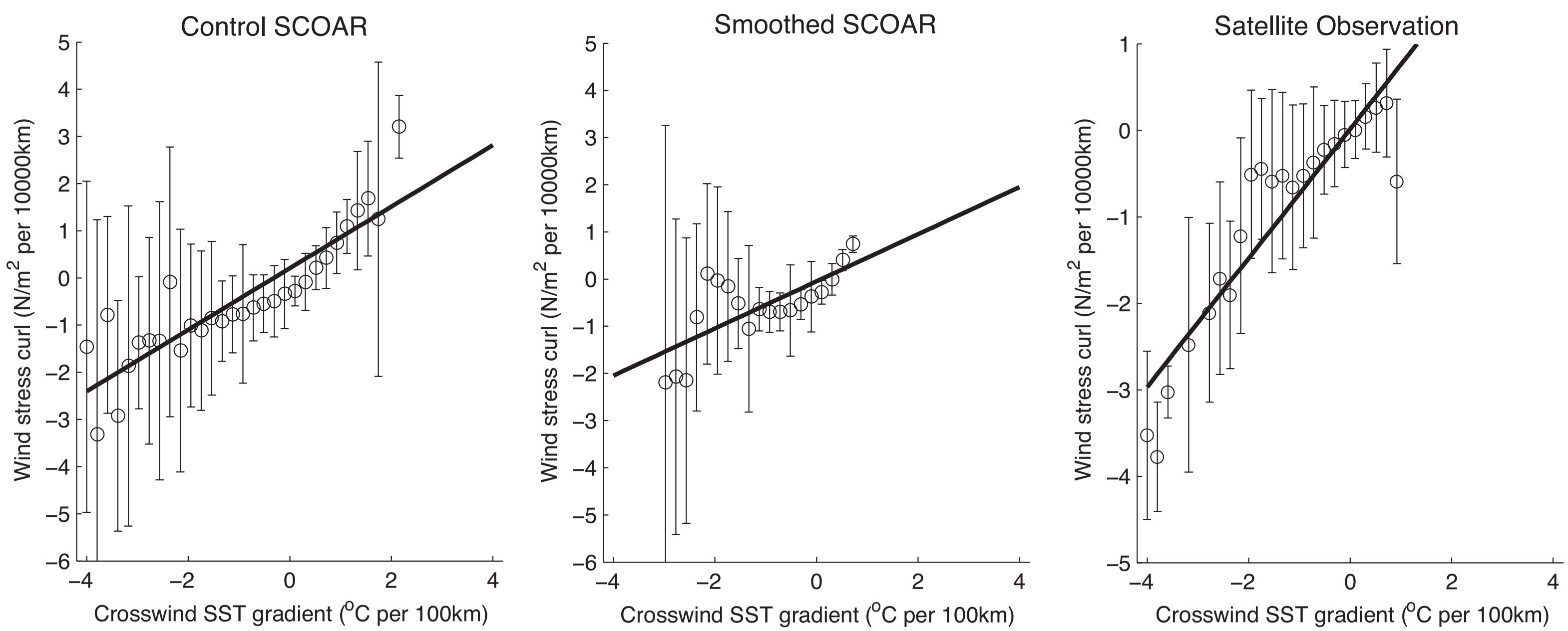

Figure 3.19: Bin scatter plot of wind stress curl (N/m^2 per 10000km) against crosswind SST gradients (°C per 100km), averaged for April 2007 over the Peru domain for Control SCOAR, Smoothed SCOAR and satellite observations. Error bars are one standard deviation of wind stress curl in each bin.

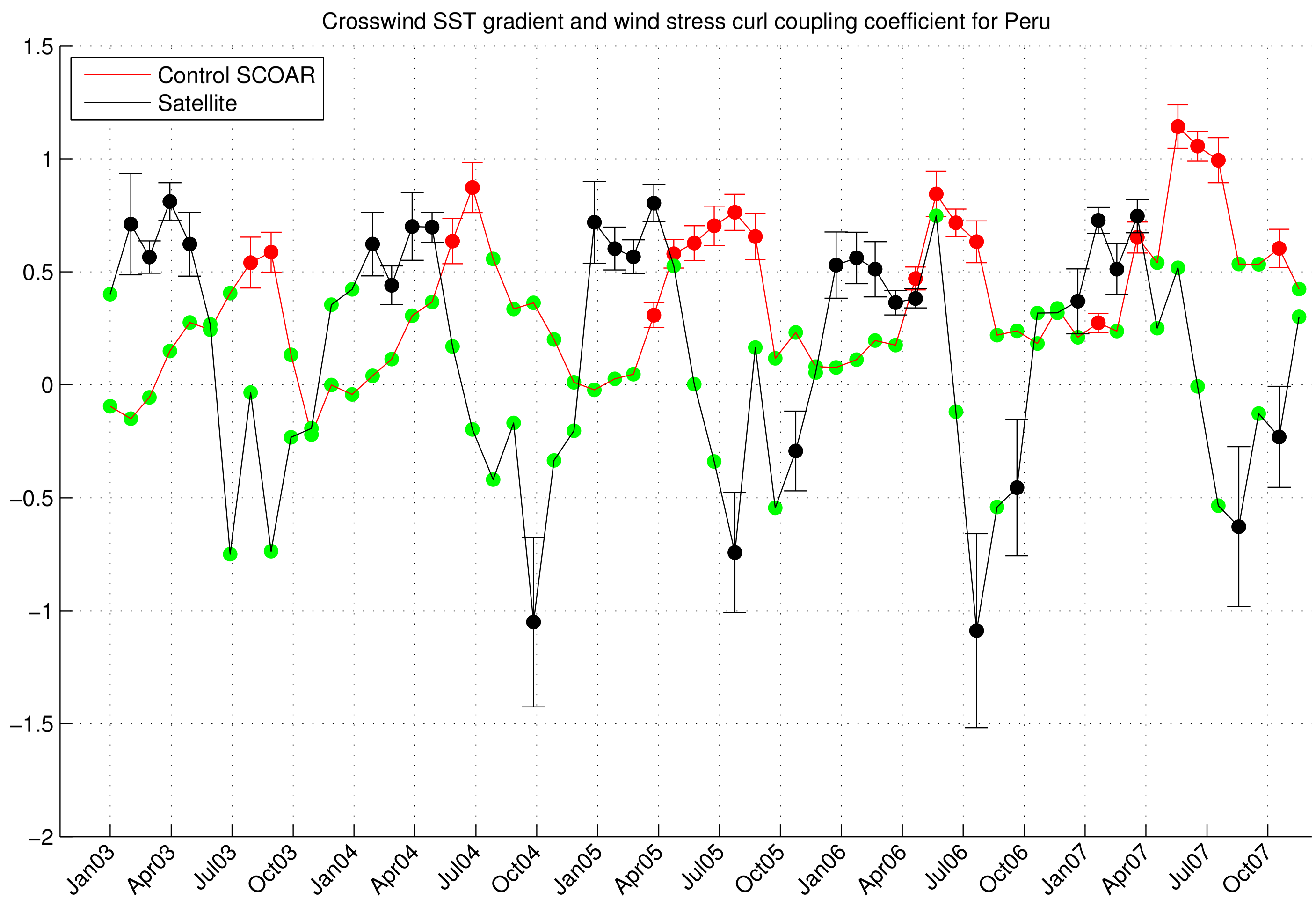

Figure 3.20: Time series of monthly coupling coefficients ($s_{c,}$) over the Peru domain for Control SCOAR (red) and satellite observations (black). Green dots indicate that the slopes have r^2 correlation less than 0.5 and/or p-values greater than 0.05. Error bars are standard errors of the slopes.

3.3 Atmospheric Response to Mesoscale SST

Heat loss at the air-sea interface through latent and sensible heat flux can play a significant role on the heat budget of the surface ocean. Observations have indicated coupling between SST and surface heat fluxes (Veechi et al., 2004) and models have shown that latent heat flux out of the ocean (into the atmosphere) have a positive correlation with mesoscale SSTs in various parts of the World ocean(Seo et al., 2007a,b).

Latent heat flux out of the ocean can be diagnosed according to the bulk parameterization of Fairall et al. (1996) as

$$LH = \rho L C_H U_a (q_s - q_a)$$

where ρ is air density, L is the latent heat of vaporization of water, C_H is the bulk exchange coefficient, U_a is the wind speed at 10m, q_a is the specific humidity of air near the surface and q_s is the saturation specific humidity based on SST. It should be noted that latent heat flux in SCOAR is computed using the non-local BL parameterization scheme in RSM (Hong and Pan (1996)), while the relation between the variability of latent heat flux and mesoscale SST patterns can be analyzed through the bulk parameterization given above and parameters that covary with SST, on which latent heat flux depends on.

A positive linear relation between SST and latent heat flux indicates the influence of SST on latent heat flux in a direct and/or indirect manner. A direct impact of an increase in SST that would raise q_s, and thus the latent heat flux out of the ocean. This is under the assumption that all other parameters have insignificant changes. Another possibility is the increase in SST would lead to greater instability of the overlying atmosphere that supports turbulent downward mixing of momentum from winds aloft to the surface that would enhance U_a and thus also increase latent heat flux. This would result not only in a positive linear relation between SST and latent heat flux, but also a positive linear relation of wind speed with SST, as well as wind speed with latent heat flux.

Figure 3.21 shows the distribution of SST, wind speed and latent heat flux averaged over April 2007 from Control SCOAR. It indicates the complicated nature of the relationship between latent heat flux, wind speed and SST. The SST distribution is diagonally divided into two regions, with warmer SSTs to the north, and cooler SSTs that decreases as one gets closer to shore. Cooler SSTs are found just off the coast of San Juan (15°S) and along Punta Lavapie (37°S), running north to Coquimbo (30°S). At the bight right off Arica (18°S), a SST maximum is seen. The winds are generally in the northwest direction (based on Fig. 3.4) that decreases with higher latitudes. Higher winds in the open ocean north of 24°S generally coincide with warmer SSTs. South of 24°S, winds weaken as one goes offshore and southwards, while SST increases as one goes offshore. Coastal jets with increased winds are seen along San Juan (15°S) and Coquimbo (30°S) that collocate with cooler SSTs, which suggest wind-driven upwelling at these locations. Much reduced winds are found around Arica (18°) which coincide with the SST maximum. Luff winds around 32°S is located under the anti-cyclonic, subtropical high. The distribution of latent heat flux can be divided into three regions: coastal region off Peru, intensified latent heat flux that runs diagonally in a northwest direction. and the southern region (south of intensified region). Low amounts of latent heat flux into the atmosphere is see right along the coast of Peru that roughly collocates with low SST, but not with wind speed. At the SST maximum off Arica (18°), where wind speed is low, latent heat flux varies wildly. In the intensified latent heat flux region, high latent heat flux generally coincide with high SST and wind speed. For the southern region, latent heat flux generally decreases with latitude, alike wind speed. However, a zonal gradient in latent heat flux is not seen, unlike in SST and wind speed.

A better measure of the relationships between latent heat flux, SST and wind speed are shown in Figure 3.22. as scatterplots of latent heat flux against SST (left), wind speed against SST (middle) and latent heat flux against wind speed (right) for April 2007 for the whole HCS domain. A linear regression is performed on each scatterplot to obtain coupling coefficients (s_{full}) and its associated r^2 correlation coefficient. For latent heat flux against SST, a positive linear relation of s_{full}=5.2W/m^2 per °C is found, with a only small fraction of the variance explained (r^2=0.31). Similarly, positive linear relationship is found for wind speed and SST (s_{full}=0.6m/s per °C), with an associated r^2=0.28. As for latent heat flux and wind speed, s_{full}=4.1W/m^2 per m/s with r^2 of 0.24. Even though a positive linear relationship is found for all three cases, the spread of the data points are large, and the fraction of variance explained (r^2 correlation coefficient) for each case is small. This would render the coupling coefficient insignificant, suggesting that under a full-coupling scenario (Control SCOAR), SST does contribute but it is not the main driver to latent heat flux, whether directly through increased flux or indirectly through turbulent mixing.

Likewise, the same linear regression analysis is performed for Smoothed SCOAR (Figure 3.23), and the results are very similar to Control SCOAR. The data points from Smoothed SCOAR are smeared within the confines of the spread in data points from Control SCOAR, which leads to similar coupling coefficients and associated r^2 correlation coefficients between Control SCOAR and and Smoothed SCOAR. For latent heat flux and SST, it is found that s_{large}= 5.0W/m^2 per °C with r^2=0.31 . As for wind speed and SST, s_{large}=0.6m/s per °C with r^2=0.29 . And for latent heat flux against wind speed, s_{large}=4.0W/m^2 per m/s with r^2=0.25. Again, the fraction of variance explained for each case is small, indicating the insignificance of the coupling coefficients (s_{large}). This also suggests that SST can contribute but is not the main driver of latent heat flux when only large-scale coupling is considered (Smoothed SCOAR).

While the direct and indirect impact of SST on latent heat flux is insignificant under full coupling and large-scale coupling, this does not preclude the insignificance of mesoscale SST impact on latent heat flux. In order to extract the mesoscale SST impact, a comparative study is made between Control SCOAR and Smoothed RSM (using smoothed SST fields from Control SCOAR to force the atmosphere (RSM)). Figure 3.24 illustrates an example of the smoothing applied to the Control SCOAR SST field for April 2007. The right most panel of Fig. 3.24 accounts for the percentage difference of the SST fields between the two cases and ranges between ± 5%. At latitudes above 18°S, most of the differences occur along the coast and stretches to roughly 2° offshore. A diagonal offshore corridor of SST differences divides 2 regions, one of negligible SST differences to the north and one of larger SST smoothing to the south. South of 21°S, larger SST difference concentrate from the shoreline to approximately 6° offshore, with reduced SST difference beyond that.

Figure 3.25 shows the latent heat flux for April 2007 for the two cases. At first glance, it seems that the latent heat flux has been directly smoothed out from Control SCOAR (left panel) onto Smoothed RSM (middle panel). However, the middle panel is a reflection of the latent heat flux into the atmosphere from implementing smoothed SST fields. The right panel gives the percentage of change in latent heat flux into the atmosphere from the two cases. It highlights similar features to the percentage of SST changed in Fig. 3.24 but with a greater range in the percentage latent heat change of ±30%. Above 18°, the difference in latent heat flux is also confined along the shoreline and extends 2-4° offshore. A diagonal corridor of latent heat difference stretches from the shoreline around (72°W, 23°S) to roughly (88°W,16°S), with intensified percentage change in latent heat flux to the south of it.

Since latent heat flux is also affected by surface wind speed, similar plots are made for wind speed (Fig. 3.26. Again, the middle panel gives the wind speed distribution when forced by smoothed SST fields from Control SCOAR, and the right panel is the percentage of change in wind speed between Control SCOAR and Smoothed RSM. With the exception of a diagonal corridor of negligible (less than 1%) wind speed percentage change, the rest of the domain show mesoscale wind speed changes that ranges between ± 5%.

Looking at the maps of percentage change in SST (Fig. 3.24), in wind speed (Fig. 3.26) and in latent heat flux (Fig. 3.25), the mesoscale patterns are strikingly similar. As such, scatter plots of these 3 quantities in relation to one another are made in Figure 3.27 to provide a better quantification on the impact of the mesoscale SST features. Similar to the coupling coefficients defined previously, the coupling coefficients (s_{meso}) here are defined by the slope to the linear fit of the scatterplots. Note that s_{meso} extracts out the impact of only the mesoscale SST upon the the latent heat flux, while previously, s_{full} includes coupling on the large scale and mesoscale, and s_{large} is only for coupling at the large scale.

The coupling between of the difference in latent heat flux to the difference in SST is s_{meso}=19W/m^2 per °C (with r^2=0.86), which is a significant coupling. It suggests that SST is the main driver of latent heat flux at the mesoscale. A significant linear fit of the difference in wind speed and difference in SST is also observed, with s_{meso}=0.27m/s per °C at r^2=0.70. This indicates the influence of warmer (colder) mesoscale SST on enhancing (reducing) surface winds that is most likely due to the increased (decreased) vertical turbulent mixing that transports momentum from winds aloft to the surface. There is also significant coupling between the difference in latent heat flux and the difference in wind speed, with s_{meso}=57W/m^2 per m/s at r^2=0.85. This reinforces the idea that mesoscale SST can have a direct influence on latent heat flux, as well as through increased (decreased) atmospheric instability that leads to greater (smaller) surface winds, and thus enhances(reduces) latent heat flux.

The calculation for mesoscale coupling coefficients, s_{meso}, are extended to each month from 2000-2007 and shown in Figure 3.28. There is no clear seasonal cycle in s_{meso}, although a trend is seen from 2006 onwards that has not been accounted for. In general, mesoscale coupling between wind speed and SST is significant, which promotes the influence of SST on atmospheric stability and surface winds at the mesoscale. Mesoscale coupling between latent heat flux and SST is significant throughout. When both mesoscale coupling are significant, chances are that both direct and indirect influence of SST to latent heat flux are at work. At times when mesoscale coupling of wind speed and SST are insignificant (flagged by r^2 <0.5), the indirect influence of mesoscale SST through atmospheric stability and surface winds would not be significant, suggesting that the direct influence of mesoscale SST on latent heat flux is the main process by which mesoscale SST drives latent heat.

Using the strategy of smoothing SST fields from Control SCOAR and applying it to an uncoupled atmosphere (Smoothed RSM), mesoscale coupling is extracted. Coupling between latent heat flux, SST and wind speeds are not seen in the fully-coupled mode (Control SCOAR) and large-scale-coupled mode (Smoothed SCOAR). However, coupling on the mesoscale (Smoothed RSM) is extracted and significant coupling is found between latent heat flux, SST and wind speeds, reinforcing the important role of mesoscale SST on ocean-atmosphere interactions.

A similar analysis is conducted to identify the imprints of mesoscale SST on the overlying atmosphere, particularly the atmospheric boundary layer. However, the effects are found to be local and small ($\sim$5% or less) and did not appear to generate a rectified response, either spatially or temporally (not shown).

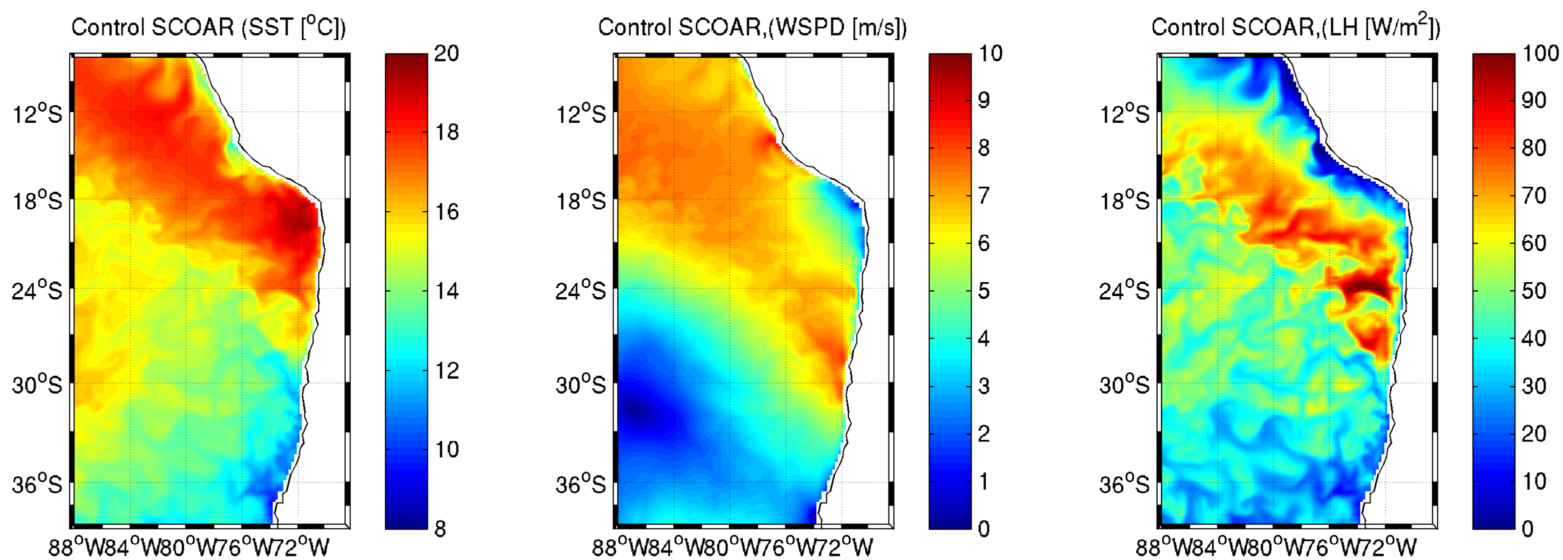

Figure 3.21: Averaged SST distribution ([°C]; left), wind speed distribution ([m/s]; middle) and latent heat flux into the atmosphere distribution ([W/m^2]; right), over April 2007 from Control SCOAR.

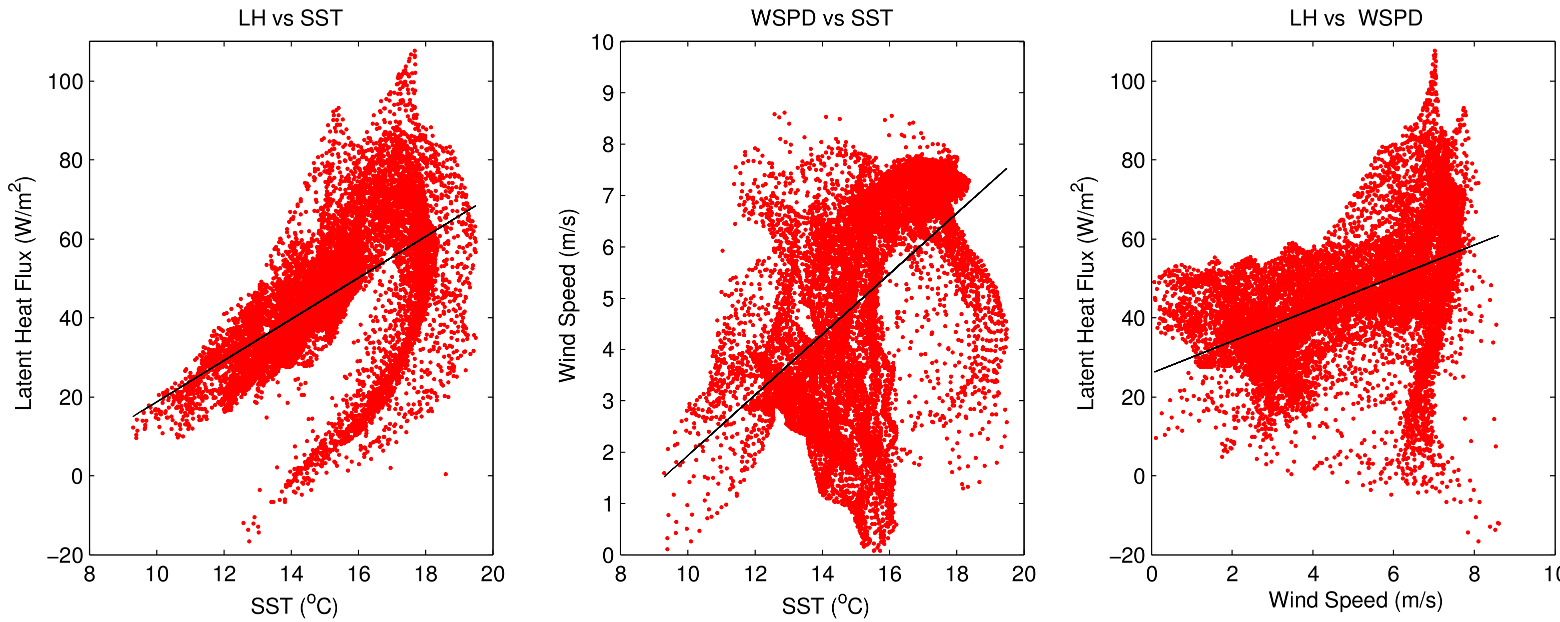

Figure 3.22: Scatter plots of latent heat flux against SST (left), wind speed against SST (middle), and latent heat flux against wind speed (right). All based on averaged April 2007 values from Control SCOAR. The slope of the linear fits give the coupling coefficients, s_{full}.

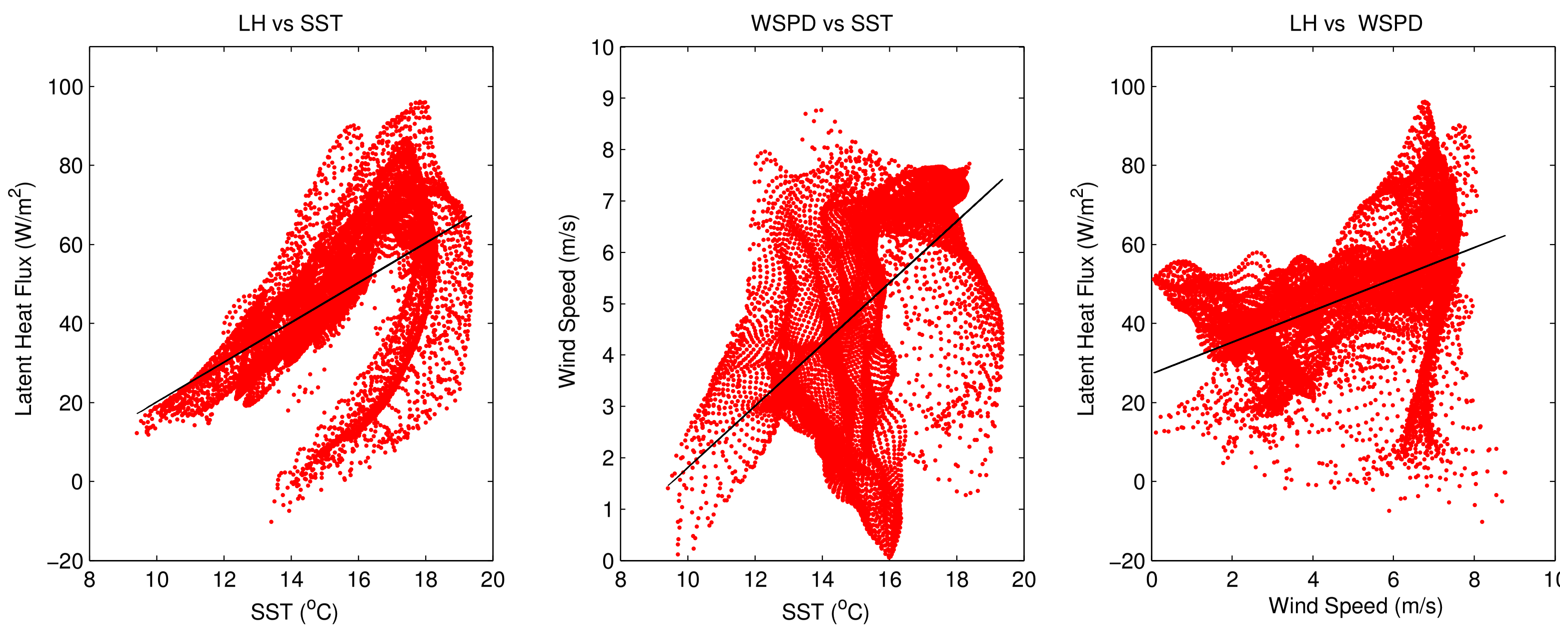

Figure 3.23: Same as 3.22 except that it is based on Smoothed SCOAR, with coupling coefficients, s_{large}.

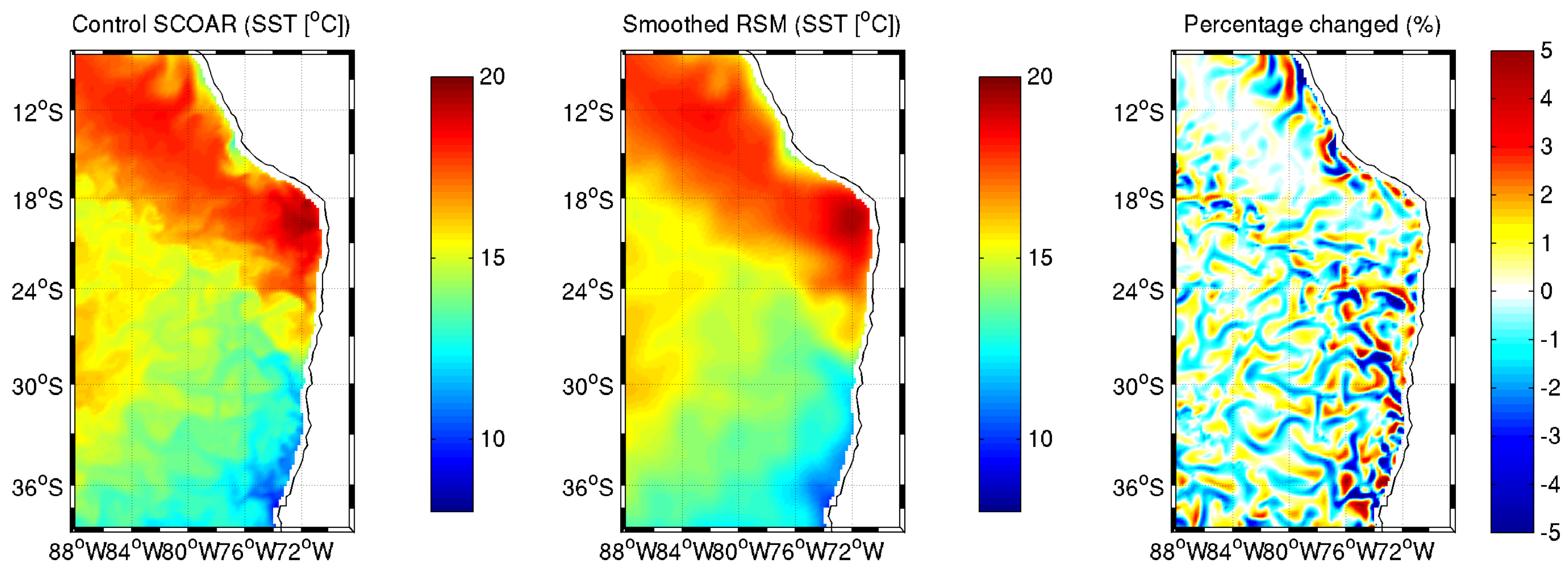

Figure 3.24: April 2007, averaged SST [°C] distribution over entire model domain for Control SCOAR (left), Smoothed RSM (center) and the percentage of their difference (right).

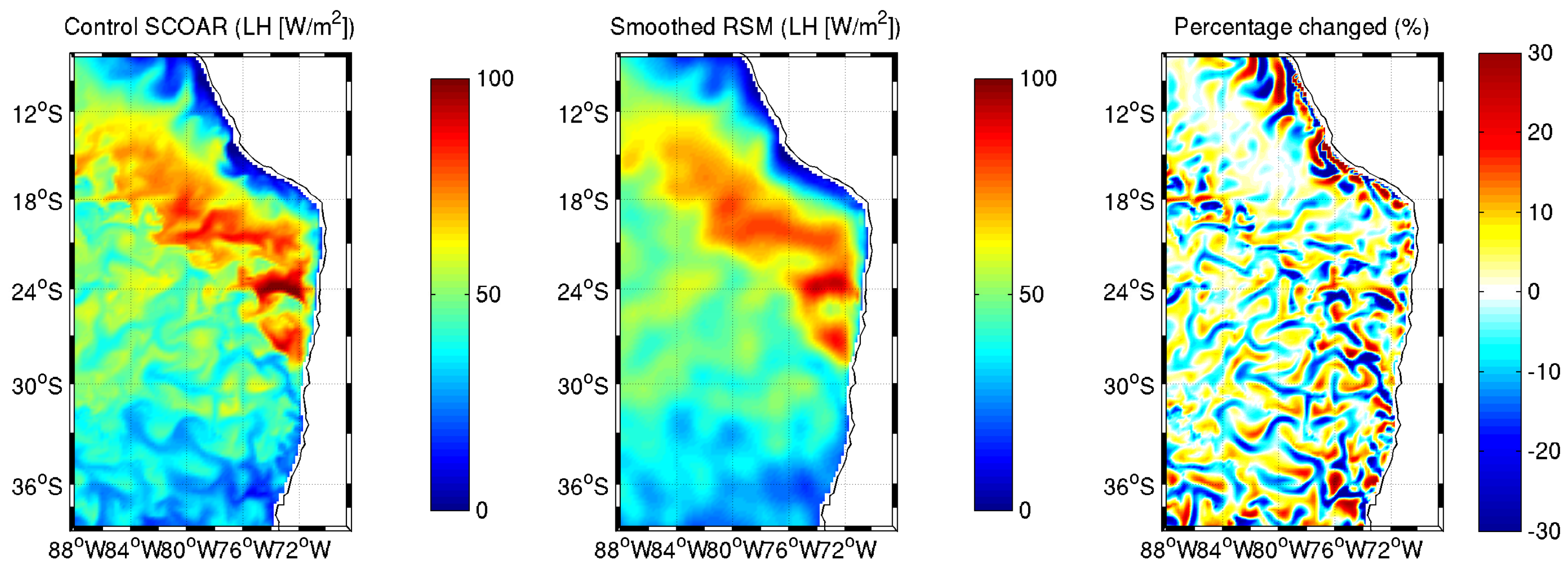

Figure 3.25: Same as 3.24 but for latent heat flux out of the ocean/into atmosphere [W/m^2].

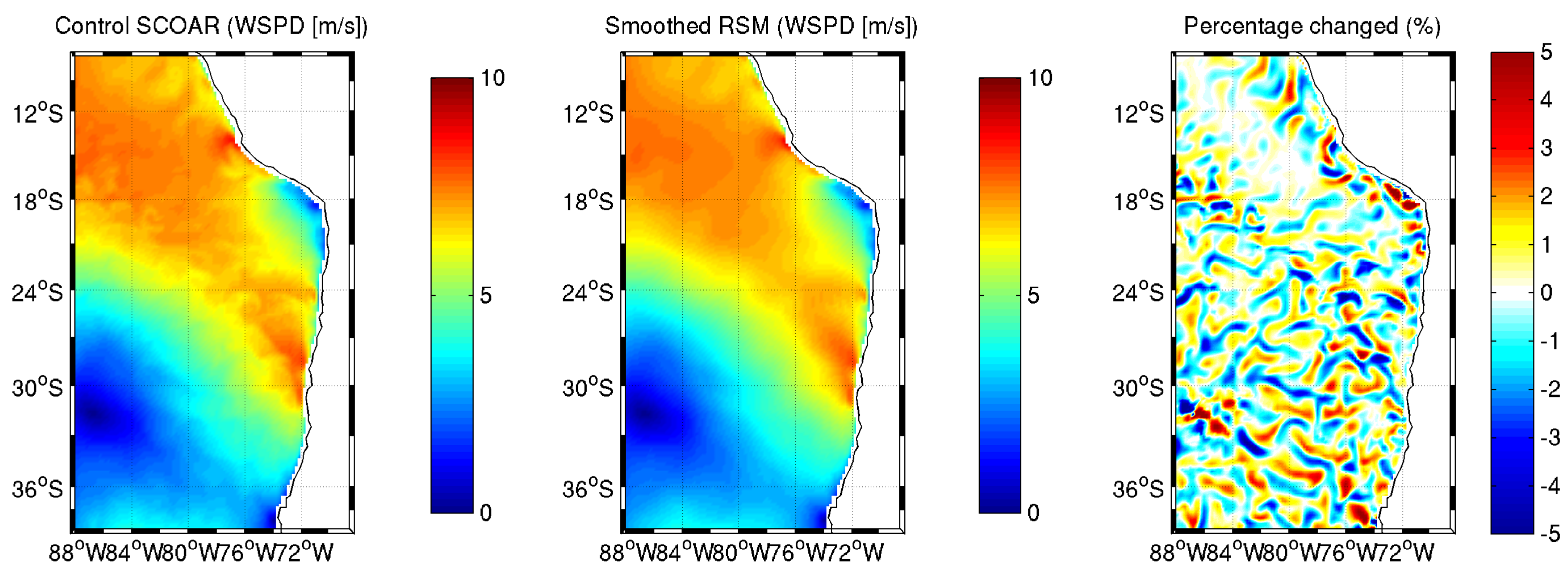

Figure 3.26: Same as 3.24 but for wind speed [m/s].

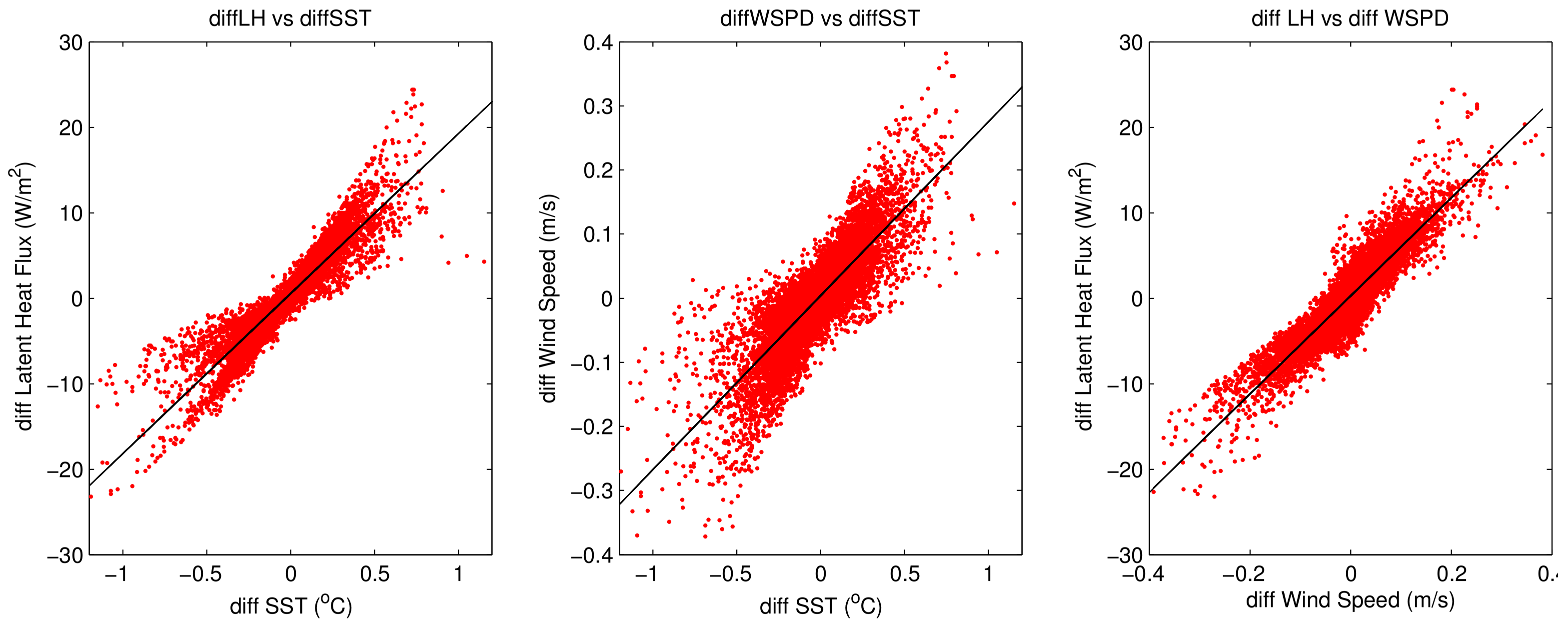

Figure 3.27: Scatter plots of difference in latent heat flux against difference in SST (left), difference in wind speed against difference in SST (middle), and difference in latent heat flux against difference wind speed (right). All are based on averaged April 2007 values from Control SCOAR-Smoothed RSM. The slope of the linear fits give the coupling coefficients, s_{meso}.

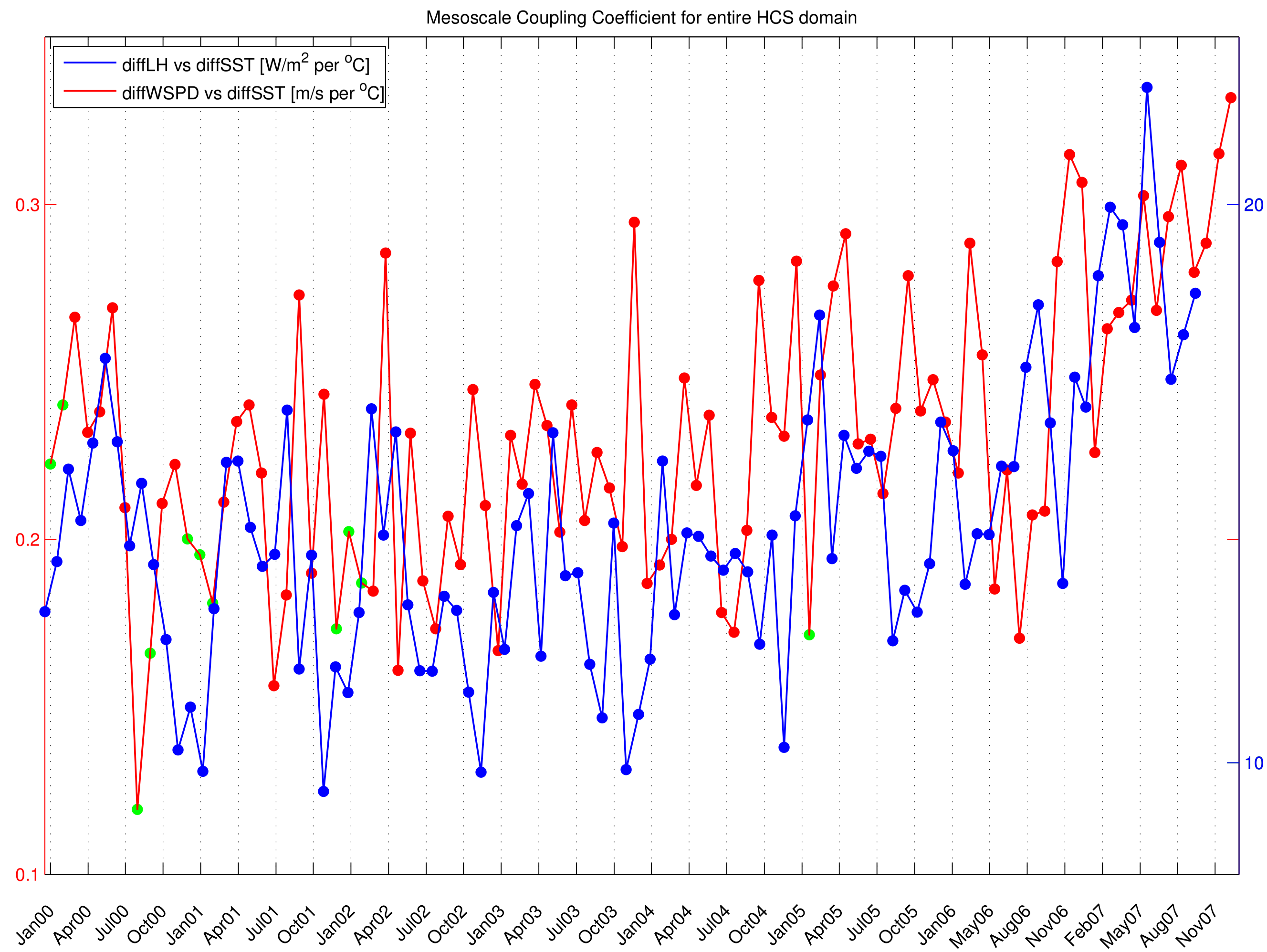

Figure 3.28: Time series of monthly mesoscale coupling coefficients (s_{meso}) for difference in latent heat against difference in SST(blue; [W/^{2} per °C]; right axis) and difference in wind speed against difference in SST (red; [m/s per °C]; left axis). Green dots indicate that the slopes have r^2 correlation less than 0.5 and/or p-values greater than 0.05.

3.4 Ocean Eddy Statistics

Spall (2007) proposed that SST-wind stress coupling can have an impact on the baroclinic instability in the ocean. Within an idealized framework, he showed that along gradients in SST, with winds blowing from warm to cold waters, the SST-wind stress coupling would act to increase the wavelength and growth rate of the most unstable waves. Conversely, with winds blowing from cold to warm waters, SST-wind stress coupling would reduce the wavelength and the growth rate of the most unstable waves. As such, under a fully-physics and dynamical framework, a comparative study using Control SCOAR and Smoothed SCOAR allows an investigation of the impact of full coupling, which has SST-wind stress coupling based on previous section, versus semi-large-scale coupling, which does not have SST-wind stress coupling, upon the ocean eddies. A reminder that the main difference between the two run is that in Smoothed SCOAR, the atmosphere only sees a smoothed version of the SST field from ROMS, but ROMS is allowed to freely evolve at the same grid resolution as that in Control SCOAR. In addition, a third run (Smoothed ROMS) is added to assess the influence of spatially-smoothed surface forcing on the ocean. Smoothed ROMS is an uncoupled ocean (ROMS) run that is daily forced by spatially-smoothed surface atmospheric fields from Control SCOAR. It uses the same Lowess filter that had been used to smooth SST fields in Smoothed SCOAR.

Figure 3.29 shows the root-mean-square (RMS) distribution of SST for Control SCOAR (left), Smoothed SCOAR (middle) and Smoothed ROMS (right). Control SCOAR and Smoothed SCOAR have very similar SST variability distribution. Both show larger SST variability in the southwest portion of the domain, as well as along the coast, particularly around San Juan region and Taltal. On the other hand, Smoothed ROMS has much reduced SST variability along the coast. In the open water, the SST variability of Smoothed ROMS reveal a spatial pattern that resembles Control SCOAR and Smoothed SCOAR. The reduced SST variability along the the coast is likely due to the smoothing of the forcing fields. Figure 3.30 shows the seasonal wind stress pattern used in Smoothed ROMS, which has reduced the magnitude of the wind stress along the coast and a shifted maximum wind stress offshore when compare to Fig. 3.4.

The RMS distribution of SSH for Control SCOAR and Smoothed SCOAR are also similar to one another (Figure 3.31). North of 13°S and along the coast, variability of SSH is minimal. In the open water, there are two regions of SSH variability, one between 14°S-22°S and a more intensified region between 25°S-36°S. Smoothed ROMS have a similar distribution of SSH variability (bottom left of Fig. 3.31) to the coupled cases, with the exception of a broader minimum in RMS of SSH along the coast from 27°S-38°S. The power spectrum of SSH for latitudinal band 25°S- 36°S is shown for the 3 cases (bottom right of Fig. 3.31). Note that the power spectrum is computed using roughly 130,000 data record series (45 records for each day of 2000-2007). The power spectrum for Control SCOAR and Smoothed SCOAR are almost identical, suggesting that the change in the spatial scale of coupling does not produce a rectified response on ocean eddies. On the other hand, Smoothed ROMS has higher power than the coupled cases, for wavelengths larger than 250km.

A further understanding of ocean eddy activity can be quantified using vorticity. Figure 3.32 presents RMS of vorticity over the model domain for Control SCOAR, Smoothed SCOAR and Smoothed ROMS. Again, the coupled cases show similar RMS distribution, with greater variability in vorticity seen in upwelling regions such as San Juan, Coquimbo and Punta Lavapie, where instability sets up and eddies are generated. A diagonal divider from (72°W,28°S) to (88°W,16°S) separates a region of minimal vorticity variability to the north, and a region of intensified variability in ocean eddies to the south. South of 32°S, the vorticity variability in the open sea dips by a factor of half from the intensified region. As for Smoothed ROMS, the general RMS distribution of vorticity is also similar to the coupled case. However, along the coast, this variability has been significantly reduced, which is likely again due to the smoothed forcing fields. The power spectrum of the vorticity in latitudinal band 21°S-32°S for Control SCOAR (contains SST-wind stress coupling) and Smoothed SCOAR (does not have SST-wind stress coupling) are off the same shape and peak at the same wavelength (200-300km), with only a very weak increase in energy of eddies in the mesoscale band for Control SCOAR compared to Smoother SCOAR. This suggests that the SST-wind stress coupling does not have a strong impact on the ocean eddies in the HCS. It is likely that the weak SST gradients and SST-wind stress coupling found in HCS contribute to the lack of a strong response of the ocean eddies .

The power spectrum of the vorticity shows that the coupled case contains less energy than the uncoupled Smoothed ROMS run for wavelengths larger than 250km. This may indicate that air-sea feedback works to reduce this energy. However, this is not definitive because of the spatial structure of the atmospheric forcing along the coast. In Smoothed ROMS, the shift of wind stress peak offshore (Fig. 3.30) changes the mean field of the forcing along the coast and sets up a different mean state for ocean circulation and eddy generation. As such, the instability properties that arise from a different mean state have changed, and the ocean eddies cannot be directly compared to one another. The difference in the power spectrum between the uncoupled Smoothed ROMS and the coupled case could thus be attributed to different mean state of the ocean that generate more energetic instabilities and/or the absence of air-sea coupling feedback has allowed for more energetic ocean eddies.

The feedback on the ocean from full coupling (Control SCOAR) and large-scale coupling (Smoothed SCOAR) does not produce significant difference on the ocean eddy statistics in the HCS. This suggests that removal of mesoscale features onto the atmosphere does not produce any rectification that would affect the ocean eddies. It is possible that the SST gradients in HCS, as well as the SST-wind stress coupling, may not be strong enough to produce similar results to what Spall (2007) found.

This chapter, in part, is being prepared for publication. Dian Ariyani Putrasahan, Arthur J. Miller, and Hyodae Seo. I am the primary investigator and author of this paper.

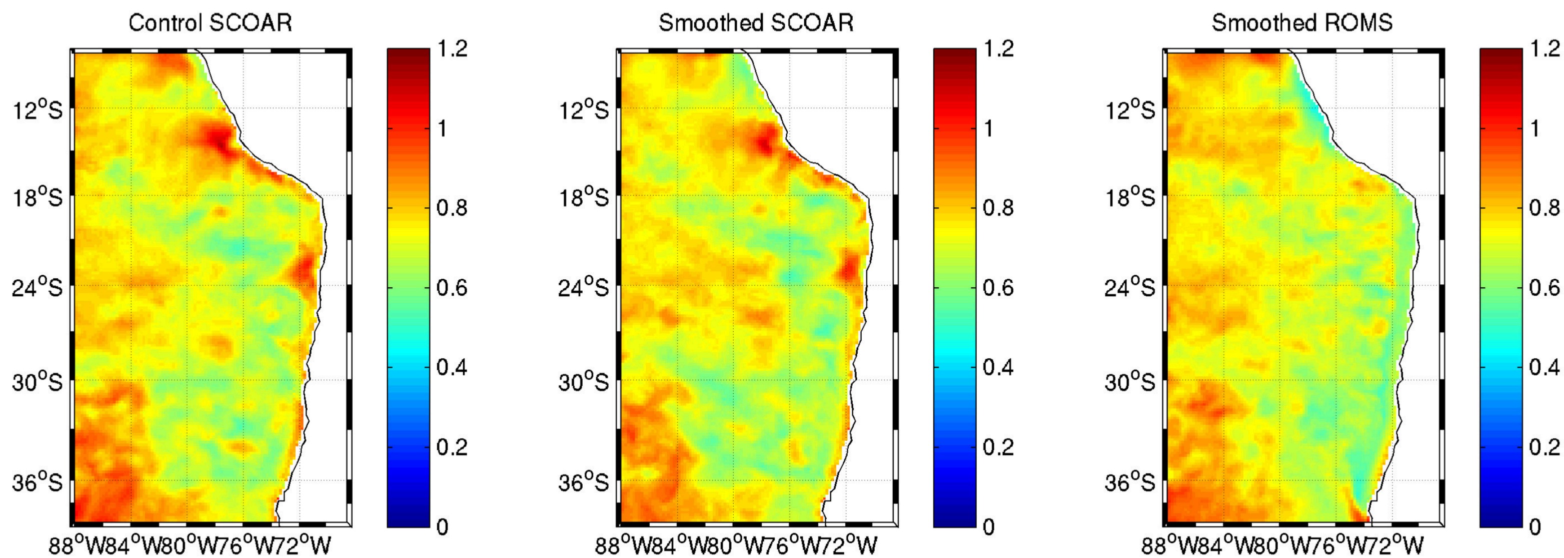

Figure 3.29: Spatial distribution of root-mean-square (RMS) of SST (°C) for Control SCOAR (left), Smoothed SCOAR (middle) and Smoothed ROMS (right) for the time period of 2000-2007.

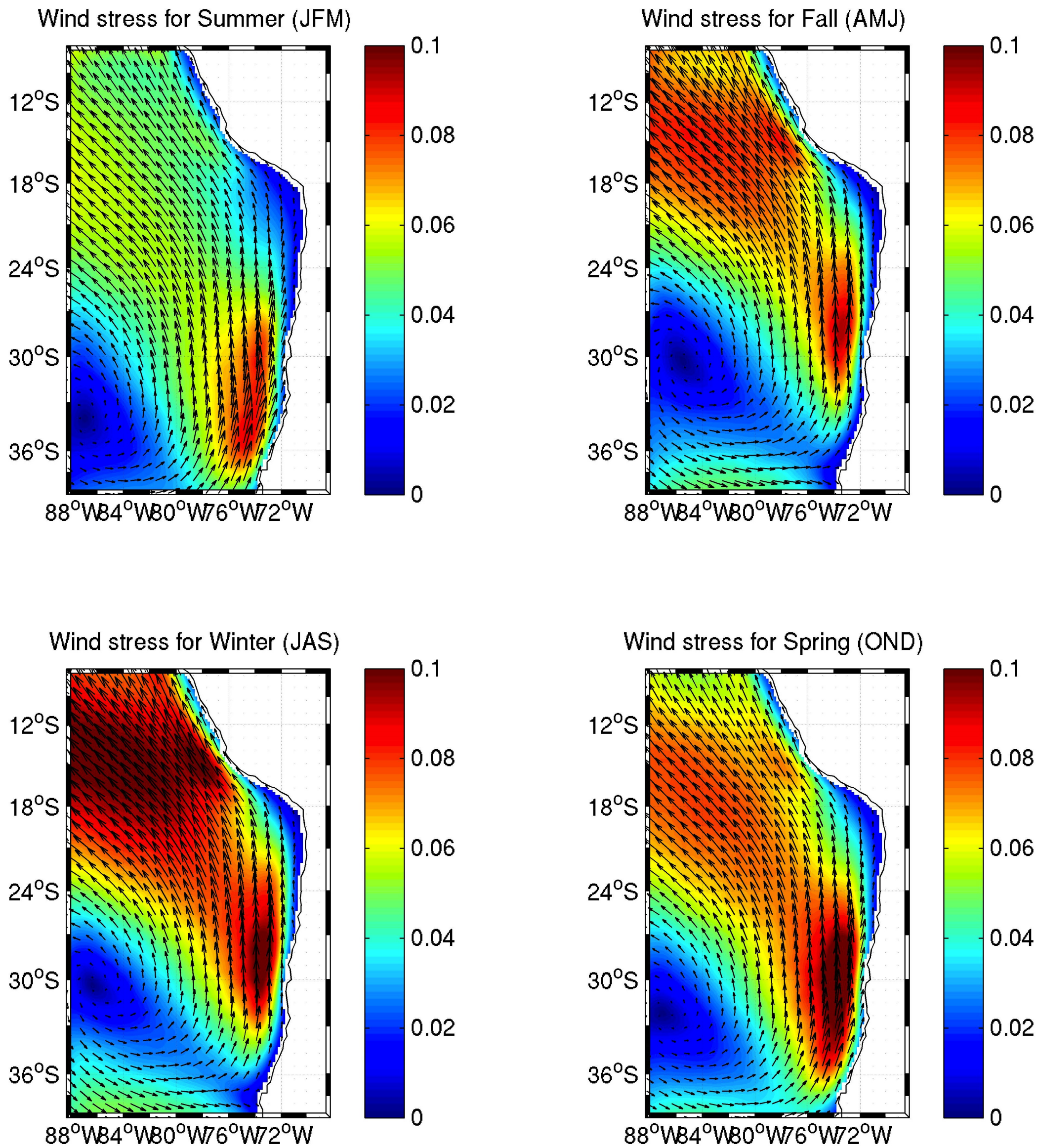

Figure 3.30: Seasonal wind stress field (N/m^2) based on Smoothed ROMS over the HCS region averaged from 2000-2007. Austral summer (JFM; top left), fall (AMJ; top right), winter (JAS; bottom left), and spring (OND; bottom right).

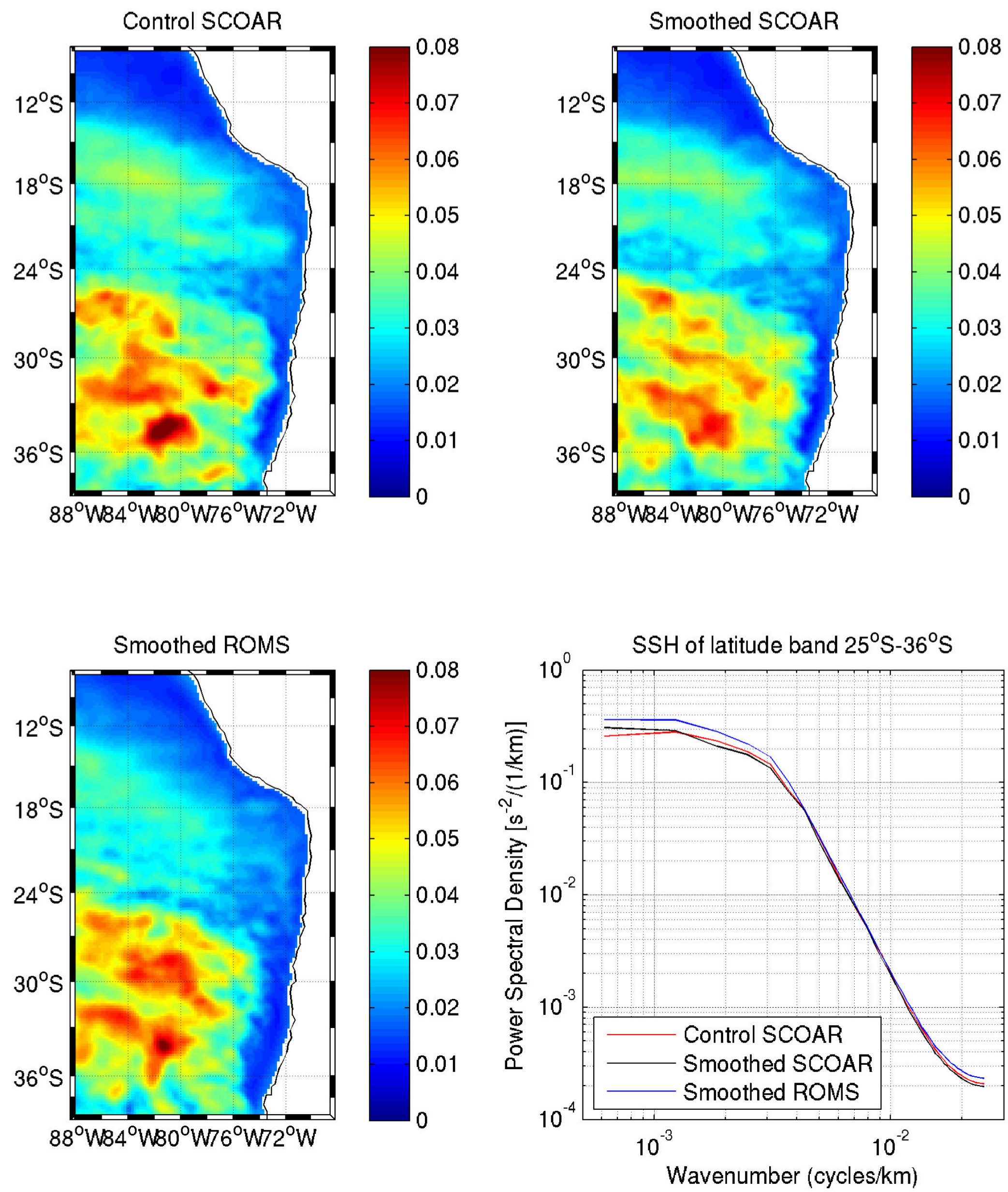

Figure 3.31: Spatial distribution of root-mean-square (RMS) of SSH (°C) for Control SCOAR (top left), Smoothed SCOAR (top right) and Smoothed ROMS (bottom left) for the time period of 2000-2007. Bottom right panel shows the power spectrum of SSH for latitude band 25°S-36°S for Control SCOAR (red), Smoothed SCOAR (black) and Smoothed ROMS (blue).

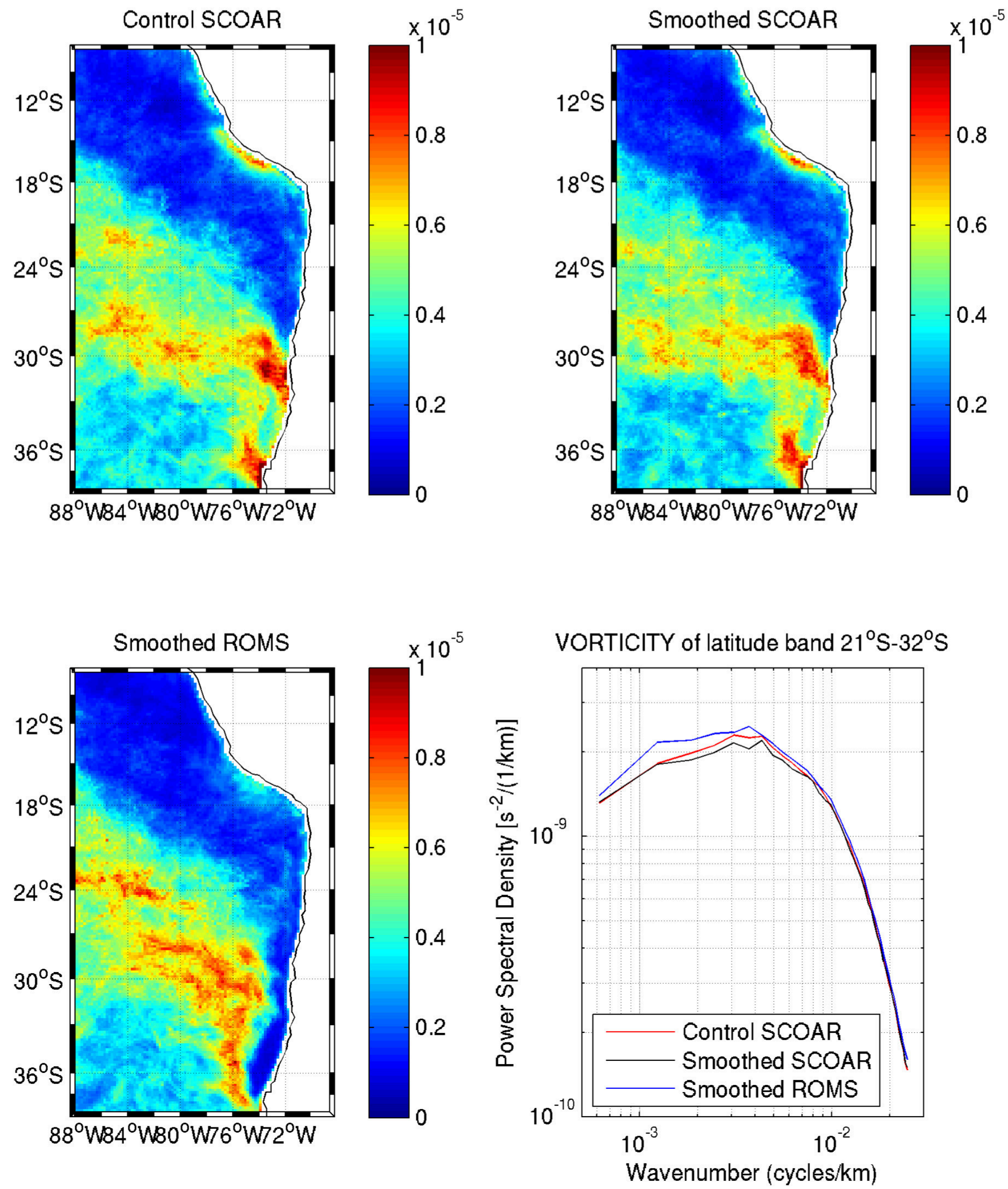

Figure 3.32: Spatial distribution of root-mean-square (RMS) of surface vorticity (s^{-1}) for Control SCOAR (top left), Smoothed SCOAR (top right) and Smoothed ROMS (bottom left) for the time period of 2000-2007. Bottom right panel shows the power spectrum of surface vorticity for latitude band 25°S-36°S for Control SCOAR (red), Smoothed SCOAR (black) and Smoothed ROMS (blue).

Chapter 4

Isolating Mesoscale Coupled Ocean-Atmosphere Interactions in the Kuroshio Extension Region

4.1 Coupled Ocean-Atmosphere Interactions

4.1.1 Abstract

The Kuroshio Extension region is characterized by energetic oceanic mesoscale and frontal variability that alters air-sea fluxes that can influence large-scale climate variability in the North Pacific. We investigate this mesoscale air-sea coupling using a regional eddy-resolving coupled ocean-atmosphere (OA) model that downscales observed large-scale climate variability. The model simulates many aspects of the observed seasonal cycle of OA coupling strength for both momentum and surface heat fluxes. We introduce a new modeling approach to study the scale-dependence of two well-known mechanisms for surface wind response to mesoscale sea surface temperatures (SST), namely, vertical mixing mechanism (VMM) and pressure adjustment mechanism (PAM). We compare the fully coupled model to the same model with an online, 2-D spatial smoother applied to remove mesoscale SST field felt by the atmosphere. Both VMM and PAM are found to be active during the strong wintertime peak in coupling strength seen in model and in ob-

servations. For VMM, large-scale SST gradients surprisingly generate coupling between downwind SST gradient and wind stress divergence that is often stronger than coupling on the mesoscale, indicating their joint importance in OA interaction in this region. In contrast, coupling between crosswind SST gradient and wind stress curl occurs only on the mesoscale, and not over large-scale SST gradients, indicating the essential role of ocean mesoscale. For PAM, model results indicate that coupling between the Laplacian of sea level pressure and surface wind convergence occurs for both mesoscale and large-scale processes, but inclusion of the mesoscale roughly doubles the coupling strength.

4.1.2 Introduction

In the western North Pacific Ocean, where major ocean currents meet along the eastern coast of Japan, meandering sea surface temperature (SST) fronts form. From the south, a strong and warm western boundary current hugs the Southeastern coast of Japan and separates around 35°N to form the Kuroshio Extension (KE) (Mizuno and White, 1983). Within the KE, pronounced SST fronts produce climatological SST gradients steeper than 3 °C/100km (Tokinaga et al., 2009), with synoptic fronts that are much stronger, that consequently impact the surface flux exchanges with the atmosphere. The long-term variability of these flux anomalies in the KE region are known to be important in influencing large-scale decadal North Pacific climate feedback processes (Miller and Schneider, 2000; Latif, 2006; Kwon et al., 2010; Frankignoul et al., 2011).

Satellite observation-based studies have shown the strong influence of the mesoscale SST distribution upon the overlying atmospheric wind and wind stress patterns (Xie, 2004; Small et al., 2008; Chelton and Xie, 2010). Observations have also indicated coupling between SST and surface heat fluxes [e.g. Veechi et al. (2004); Thum et al. (2002); Liu et al. (2007)] and models have shown that latent and sensible heat fluxes have a negative correlation with mesoscale SSTs in various parts of the World Ocean [e.g. Seo et al. (2007a); Seo et al. (2008); Haack et al. (2008); Bryan et al. (2010)]. It is important to understand the character and mechanisms controlling these regional mesoscale flux anomalies in order to gain further insight into coupling processes controlling large-scale climate variations.

Two prominent mechanisms have been proposed to explain the response of wind in SST frontal regions, namely the vertical mixing mechanism (VMM) and the pressure adjustment mechanism (PAM). The VMM suggests that warmer (colder) SST reduces (enhances) the stability of the overlying atmosphere, which enhances (inhibits) the downward transfer of momentum through mixing, that would thus increase (decrease) surface winds [Wallace et. al, 1989] over the SST anomalies. When winds blow parallel or perpendicular to an SST front, it can lead to wind stress divergence along the downwind, or curl along the crosswind SST gradients (Chelton et al., 2001, 2004). In contrast, the PAM suggests that warm (cold) SST anomalies induce low (high) surface pressure anomalies that would promote convergence (divergence) of surface winds over the SST anomalies (Lindzen and Nigam, 1987). The relative importance of these two processes (Takatama et al., 2011) may potentially alter the way the atmosphere responds to oceanic variability in the KE region.

In this study, we analyze observations of SST and wind stress along with objectively analyzed surface heat fluxes to estimate seasonal air-sea coupling over the KE region. In order to interpret these observations, we execute novel regional ocean-atmosphere coupled modeling experiments that include and exclude the impact of oceanic mesoscale eddies, in order to isolate their effect on the strength of ocean-atmosphere (OA) coupling. In addition, the modeling strategy allows us to quantify the spatial scale over which the coupling processes reflected individually by VMM and PAM may be important.

4.1.3 Satellite Observation

Satellite observations are used to identify OA coupling in the KE region and verify the model output. For the satellite data, SST measurements are obtained from fusion of data from the Tropical Rainfall Measuring Mission (TRMM) Microwave Imager (TMI), which was launched in November 1997 (Wentz et al., 2000), and from the Advanced Microwave Scanning Radiometer on the Earth Observing System (EOS) Aqua satellite (AMSR-E), that was launched in May 2002

(Wentz and Meissner, 2000; Chelton and Wentz, 2005). We use the daily, 0.25° resolution, combined TMI and AMSRE data that are available from Remote Sensing Systems (RSS). Wind stress products are derived from the Quick Scatterometer (QuikSCAT) satellite (Freilich et al., 1994; Liu, 2002), which was in operation from July 1999 till November 2009. We use daily, 0.5° resolution wind stress products, which are also available through RSS. The Woods Hole Oceanographic Institution (WHOI) Objectively Analyzed air-sea Heat Fluxes (OAflux) project provides surface latent and sensible heat fluxes constructed from observed satellite fields and three atmospheric reanalyses, at 1o resolution from 1985 onwards (Yu and Weller, 2007).

4.1.4 Coupled model experiments

The Scripps Coupled Ocean-Atmosphere Regional (SCOAR) model is employed to perform the coupled air-sea interaction studies in the KE region. The model consists of the Experimental Climate Prediction Center (ECPC) Regional Spectral Model (RSM, Juang and Kanamitsu (1994)) as the atmospheric component, the Regional Ocean Modeling System (ROMS, Haidvogel et al. (2000); Shchepetkin and McWilliams (2005)) as the oceanic part, and a flux-SST coupler built by Seo et al. (2007b) to bridge the two. Currently, the coupling works in a sequential manner, such that RSM and ROMS run individually and alternatively, exchanging forcing fields at specified increments. For this study, the ocean and atmosphere are coupled on a daily timescale. The SCOAR model is chosen because it has been shown to be effective in capturing mesoscale coupling in tropical and mid-latitudinal oceans (Seo et al., 2007b, 2008).

The model domain chosen covers a regional grid of the western North Pacific that includes Japan and the Kuroshio Extension (125°E-165°E, 31°N-47°N). The atmospheric and ocean model have the same horizontal grid with 25 km resolution and matching land-sea mask. The atmosphere has 28 vertical layers whilst the ocean has 30 layers. The vertical coordinates for the ocean model were stretched to give higher resolution to the surface layers. The ocean spin up (in uncoupled mode) is forced by National Centers of Environmental Prediction Reanalysis-2 (NCEP R2, Kanamitsu et al. (2002a)) winds from 1980-2000 to allow equilibration before any runs are performed. NCEP R2 is used as boundary conditions for the atmosphere, such that the model provides a downscaling of observations. Oceanic boundary conditions are taken from monthly Japan Agency for Marine-Earth Science and Technology (JAMSTEC) Ocean General Circulation Model for the Earth Simulator (OFES) dataset provided by The Earth Simulator Center, JAMSTEC [Sasaki et al., 2006]. We run the coupled model for 8 years (commencing in 2000), giving one year to allow the coupled system to equilibrate, thereby providing a 7-year (2001-2007) daily output of the oceanic and atmospheric state. This model run overlaps the satellite observed time period for 2003-2007.

In order to isolate the impact of mesoscale SST on the coupling, we employ a novel strategy. We execute a Smoothed SCOAR run, in which we interactively smooth the SST that is felt by the atmosphere, over the same time period and same resolution as the fully coupled Control SCOAR run. Note that the actual SST in the ocean model is left unchanged but evolves instead under the influence of the atmosphere that has seen only the smoothed SST field. In the experiments that remove the mesoscale air-sea interactions, an online 2-D spatial, locally weighted scatterplot smoothing (lowess) filter (Cleveland, 1979; Schlax et al., 2001) is applied to the SST field that forces RSM at each coupling step. This procedure allows large-scale SST coupling to be preserved while extinguishing the mesoscale eddy impacts on the atmospheric boundary layer. This technique allows us to separate the spatial scales of air-sea coupling by comparing with the fully-coupled run. Here we choose a 5-degree lowess filter, which yields an effective cutoff wavelength of 3 deg (300 km) in latitude and longitude.

4.1.5 Results and Discussion

The Control SCOAR produces a strong Kuroshio current and vigorous mesoscale eddy field that yields meandering SST fronts (Fig. 4.1a) similar to those observed in nature. The Smoothed SCOAR run also produces a strong Kuroshio and a similarly energized mesoscale in the ocean (not shown). The smoothed SST seen by the atmosphere in Smoothed SCOAR (Fig. 4.1b) however, while exhibiting broad-scale SST anomalies, does not capture the mesoscale features in SST, as anticipated by this strategy. For our analysis, we focus on the strongly energetic open-ocean eddy region (34°N-40°N, 145°E-163°E, boxed domain in Fig. 1a), which is far from the (physical) western boundary as well as the (specified) open boundaries.

a. SST-wind stress coupling through vertical mixing mechanism

The strength of the VMM can be quantified following Chelton et al. (2001) by estimating the linear relationship between wind stress divergence and downwind SST gradients, and represented as the coupling coefficient, s_d. At each grid point in the box, we computed these fields, binned them, and plotted the mean from each bin in a scatter diagram with error bars indicating plus-or-minus one standard deviation. A regression coefficient (here called the coupling coefficient) was then computed from the slope of the linear fit to the mean values of each bin, along with the standard error of the slope, a p-value and a squared correlation coefficient (r^2). We consider a slope to be significant if the p-value is less than 0.05 and at least 50% of the variance is explained in the linear relation (equivalent to r^2 greater than 0.5), the latter criterion being a measure of the physical usefulness of the relation. Note that no spatial highpass filtering of the observations or the model output was performed in this procedure, unlike previous studies (Chelton et al., 2001, 2004; O'Neill et al., 2005). This allows us to retain the influence of large-scale coupling in VMM and help us in the assessment of the relative role of the large scale and mesoscale SST on coupling strength.

Fig. 4.2a shows an example of coupling between wind stress divergence and downwind SST gradients for January 2006. Over the active mesoscale eddy region, the Control run, Smoothed run and observations all exhibit significant coupling, with s_d=1.12±0.02, s_d=1.71±0.09, s_d=1.07±0.11, respectively. The rough comparability between model and observation is an indication that SCOAR is reasonably representing the surface flux coupling processes in the simulations. Control SCOAR and Smoothed SCOAR each produce coupling coefficients that, surprisingly, are within 50% of each other. The range of SST gradients in Smoothed

SCOAR (± 3 °C/100km) is smaller than in the Control SCOAR(± 5 °C/100km), yet even these weaker large-scale temperature gradients can have a significant influence on the regional wind stress divergence.

This analysis was repeated for every month of 2003-2007 and a time series of the coupling coefficients is plotted in Fig. 4.2b, along with the standard error of each coupling coefficient represented by the error bars. All three cases, Control SCOAR, Smoothed SCOAR and observations, indicate that the coupling has a seasonal cycle with a pronounced and significant peak in the winter season (DJFM) when the large-scale and mesoscale fronts seasonally intensify. During summer months, the fronts are weaker and the coupling is near zero and not significant. In winter months, the model, however, typically exhibits coupling estimates that are higher than observations by roughly a factor of two. Possible reasons for this model-data mismatch are (i) model errors, (ii) noise in the observations, (iii) systematic undersampling in the observations due to smoothing of the mesoscale features that may produce a stronger response, or (iv) model-data differences in the random mesoscale SST distribution.

The scale-dependence experiments indicate that the coupling coefficient is not entirely attributable to coupling at the oceanic mesoscale. Rather, even large-scale SST gradients can produce a potentially important impact on the regional atmospheric boundary layer (ABL) response. Surprisingly, the magnitude of the coupling coefficient in Smoothed SCOAR is larger than in Control SCOAR. Yet, because the range of SST gradients is smaller, the largest flux anomalies occur in Control SCOAR, which is indicative of the strong impact of the local mesoscale SST anomalies in influencing the ABL.

The crosswind SST gradient relationship with wind stress curl (Chelton et al., 2001, 2004) was also investigated following this same procedure. Fig. 4.3a reveals significant wintertime coupling of these variables for Control SCOAR and observations. Again, the model tends to produce coupling coefficients (s_c) that are similar, or somewhat larger, in amplitude than the observations. When considering Smoothed SCOAR, however, the coupling coefficients are either nearly zero or indistinguishable from zero, based on the error bars, for all seasons (Fig. 4.3b). The smoothing has revealed the vital importance of mesoscale SST on this relationship. Large-scale model SST gradients are incapable of imprinting their signature on the large-scale wind stress curl field. This may be due to the wind stress curl field of synoptic-scale geostrophic winds obscuring the influence of the large-scale SST. This is in contrast to the results for large-scale SST gradients affecting wind stress divergence. The divergence field associated with intrinsic synoptic-scale variability maybe sufficiently small to allow even the large-scale SST imprint to be detected.

b. SST-wind coupling through pressure adjustment mechanism

We next investigate the pressure adjustment mechanism in the KE region by computing the linear relationship of 10m wind convergence and sea level pressure (SLP) Laplacian (Minobe et al., 2008, 2010; Takatama et al., 2011; Shimada and Minobe, 2011) over the same active eddy region as the previous SST-wind stress analysis. The strength of the coupling is measured by the slope of the linear fit to the bin-scatter plot of corresponding variables, and we designate the slope as the coupling coefficient, s_p. Both Control SCOAR and Smoothed SCOAR exhibit a significant linear relation of wind convergence to SLP Laplacian (Fig. 4.4a), with coupling coefficients of s_p=2.38±0.09 and s_p=1.58±0.07 respectively for the month of January 2006. A larger coupling coefficient in Control SCOAR suggests that the mesoscale coupling heightens the linear relationship of SLP laplacian to wind convergence.

For each month of 2003-2007, we computed the coupling coefficient that reflects the PAM and its time evolution. Fig. 4.4b illustrates the seasonal cycle of this coupling, with peaks during winter seasons. Control SCOAR consistently produces higher coupling coefficients than Smoothed SCOAR, suggesting that large-scale coupling through this mechanism is not as significant as mesoscale coupling.

c. SST-latent heat flux coupling

The latent heat flux out of the ocean and into the atmosphere is a major source of energy for winter-time synoptic variability in the atmosphere. As such, the extent to which the distribution of SST, rather than intrinsic atmospheric variability, alters the amount of heat exchange is important. SST can affect the surface latent heat flux by changing the saturation humidity, by altering the stability of the ABL, and by the indirectly changing the wind speed variations via VMM. Increased winds over warmer waters would enhance evaporative cooling, thereby decreasing SST (negative feedback). We study the impact of SST distribution on surface heat fluxes by examining the spatial changes in surface latent heat flux (|dLH|=dLH/dx and dLH/dy) with spatial changes in SST (|dSST| = dSST/dx and dSST/dy) and quantify the presence of such linear relations by creating a bin-scatter plot (Veechi et al., 2004; Seo et al., 2008). This was performed over the same active eddy region as with SST-wind stress analysis.

In the KE region, a significant negative linear relationship between |dLH| and |dSST| is seen in Control SCOAR, Smoothed SCOAR, as well as in observation (Fig. 4.5a), with associated coupling coefficients of s_l=-16.2±0.3, s_l=-17.5±0.9, s_l=-13.1±0.6 respectively for a typical winter month, January 2006. This reinforces the ability of SCOAR to simulate surface flux coupling in this region. Control SCOAR and Smoothed SCOAR have similarly sized coupling coefficients, implying contributions of both large-scale and mesoscale coupling to the surface heat flux-SST relationship. The coupling between surface heat fluxes and SST is significant year-round (Fig. 4.5b). There is a clear seasonal cycle to the coupling, with the steepest negative relation in winter and weak coupling in summer. The amplitude of the variability of s_l in the observations is smaller than in the model, with weaker coupling (factor of 0.7) in winter months and stronger coupling in summer months (factor of 2.0) for the observations, compared to model output. Similar results were obtained for sensible heat flux and SST coupling (not shown).

4.1.6 Summary

Regional coupled OA interactions were explored in the KE region using both observations and a coupled model. Within the KE region, the simulations reveal strong coupling between SST anomalies and winds, wind stresses and surface heat fluxes, with amplitudes, seasonal variations and wintertime maxima that exhibit many similarities with observations. Exploration of the importance of spatial scales on the strength and nature of the coupling was achieved by using a novel modeling strategy. A 2-D interactive spatial smoother, acting only on the SST seen by the atmosphere but not altering the actual oceanic state in any direct way, allows a straightforward analysis of the scale of OA coupling by comparing the output with a fully coupled run.

Two mechanisms of coupling were explored, the VMM and PAM. The Control SCOAR simulations reveal that both mechanisms are active and significant, especially in winter. Differences in the strength of coupling between the Control and Smoothed SCOAR runs indicate how the spatial scale of SST fronts affects the OA coupling via these two mechanisms. Intuitively, one might expect that the VMM would be most active on the ocean mesoscale and less significant on the large scale. Instead, the models revealed that the VMM, as expressed in the coupling between downwind SST gradients and wind stress divergence, acts strongly on both the large scale and mesoscale. In this case, large-scale SST cannot be ignored. In contrast, the VMM, as expressed in the coupling between crosswind SST gradients and wind stress curl, is extinguished over large-scale SST gradients in Smoothed SCOAR. In this case, the ocean eddies are vital. For PAM, one might expect the large-scale coupling to be dominant in establishing the PAM. Instead, the PAM is far more active on the ocean mesoscale. For latent heat flux-SST coupling, both mesoscale and large-scale features are found to be important. More detailed study is in progress to explain the consequences of these features.

The role of mesoscale coupling on the evolution of oceanic instabilities and large-scale circulations has previously been explored using perturbation wind stress and wind stress curls [e.g. Spall (2007); Hogg et al. (2009)]. The new technique introduced here opens the door for further studies to isolate the impact of ocean mesoscale eddies on the surface flux coupling processes with the atmosphere in other regions around the globe. It can also be extended to study the impact of the oceanic mesoscale on tropospheric response [e.g. Liu et al. (2007); Minobe et al. (2010)] and consequent downstream ocean-atmosphere interactions [e.g. Taguchi et al. (2009); Frankignoul et al. (2011)]. Simulations are currently in progress to address these issues and their importance in decadal climate variability in the Pacific. Finally, the interactive smoothing technique can also be applied to the atmospheric forcing fields seen by the ocean to determine the impact of the SST-induced flux anomalies on the ocean eddies themselves.

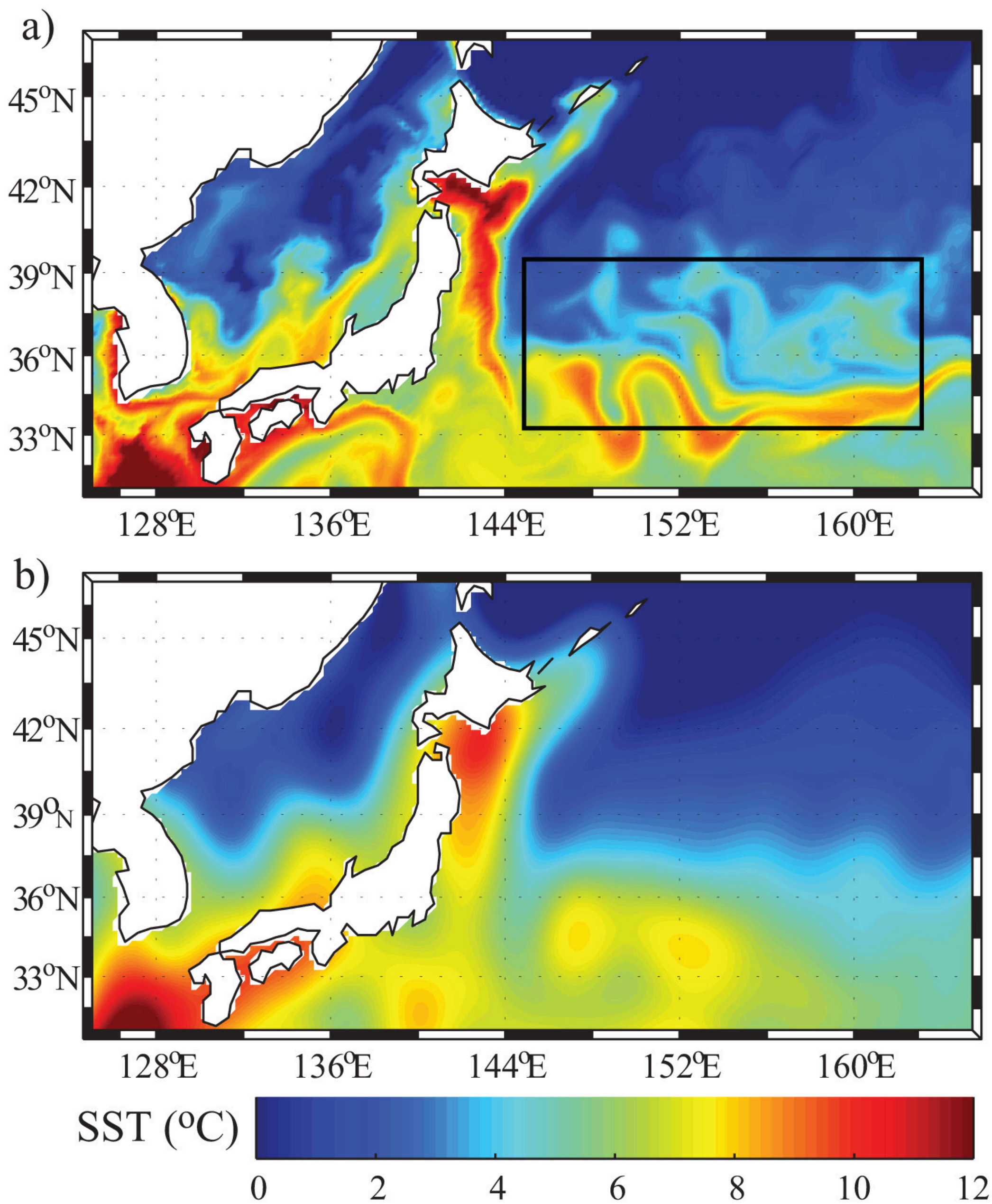

Figure 4.1: Averaged SST distribution during January 2006, over entire model domain for Control SCOAR (top) and Smoothed SCOAR (bottom). Boxed region is the active eddy region (KE region, [34°N-40°N, 145°E-163°E]) for which analysis are performed.

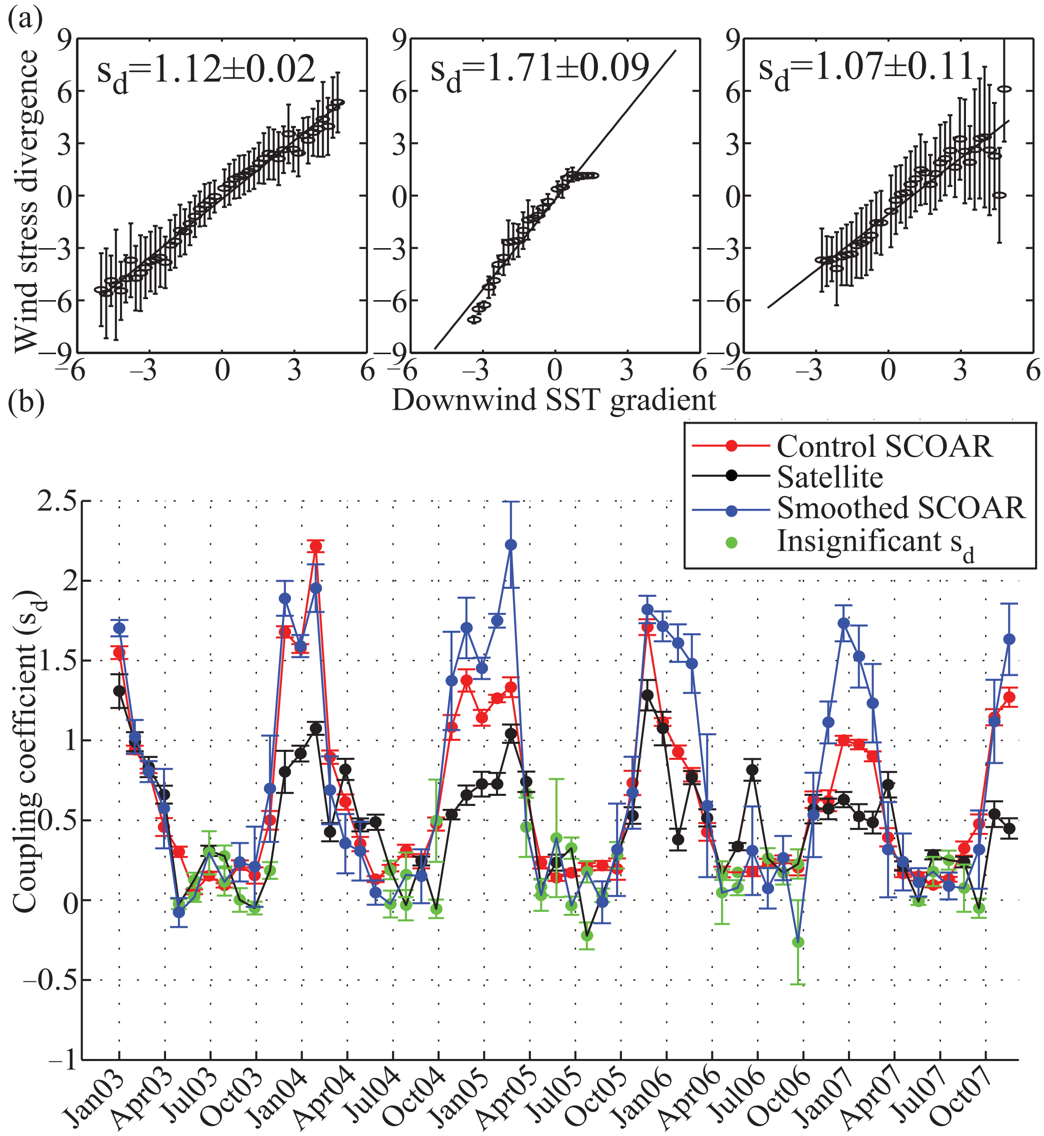

Figure 4.2: (a) Linear fit to the bin-scatter plot of wind stress divergence (N/m^2 per 10,000km) against downwind SST gradients (^{o}C per 100km) over the KE region (34°N-40°N, 145°E-163°E), averaged during January 2006, for Control SCOAR (left), Smoothed SCOAR (middle) and observations (right), along with their coupling coefficients (s_d). Error bars are one standard deviation from the mean of each bin; (b) Time series of monthly s_d for 2003-2007, for Control SCOAR (red), Smoothed SCOAR (blue) and observations (black). Error bars represent standard error of the slopes. Green dots indicate s_d with r^2 value smaller than 0.5 and p-value greater than 0.05

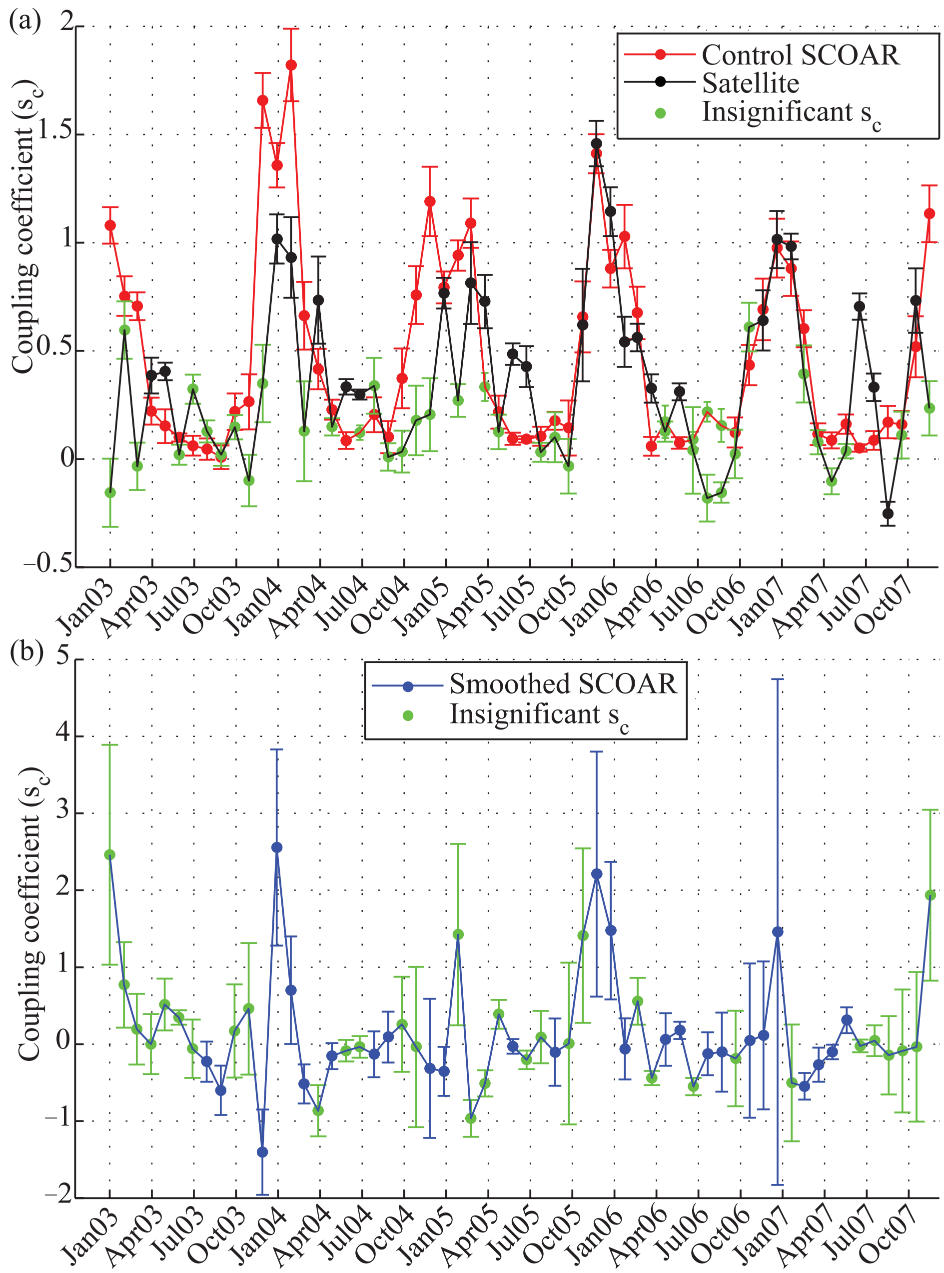

Figure 4.3: (a) Time series of monthly coupling coefficients between crosswind SST gradients (°C per 100km) and wind stress curl (N/m^2 per 10,000km), s_c, for 2003-2007, for Control SCOAR (red) and observations (black). Error bars represent standard error of the slopes. Green dots indicate s_c with r^2 value smaller than 0.5 and p-value greater than 0.05; (b) Same as above except this is for Smoothed SCOAR (blue). Error bars represent standard error of the slopes. Green dots indicate s_c with r^2 value smaller than 0.5 and p-value greater than 0.05

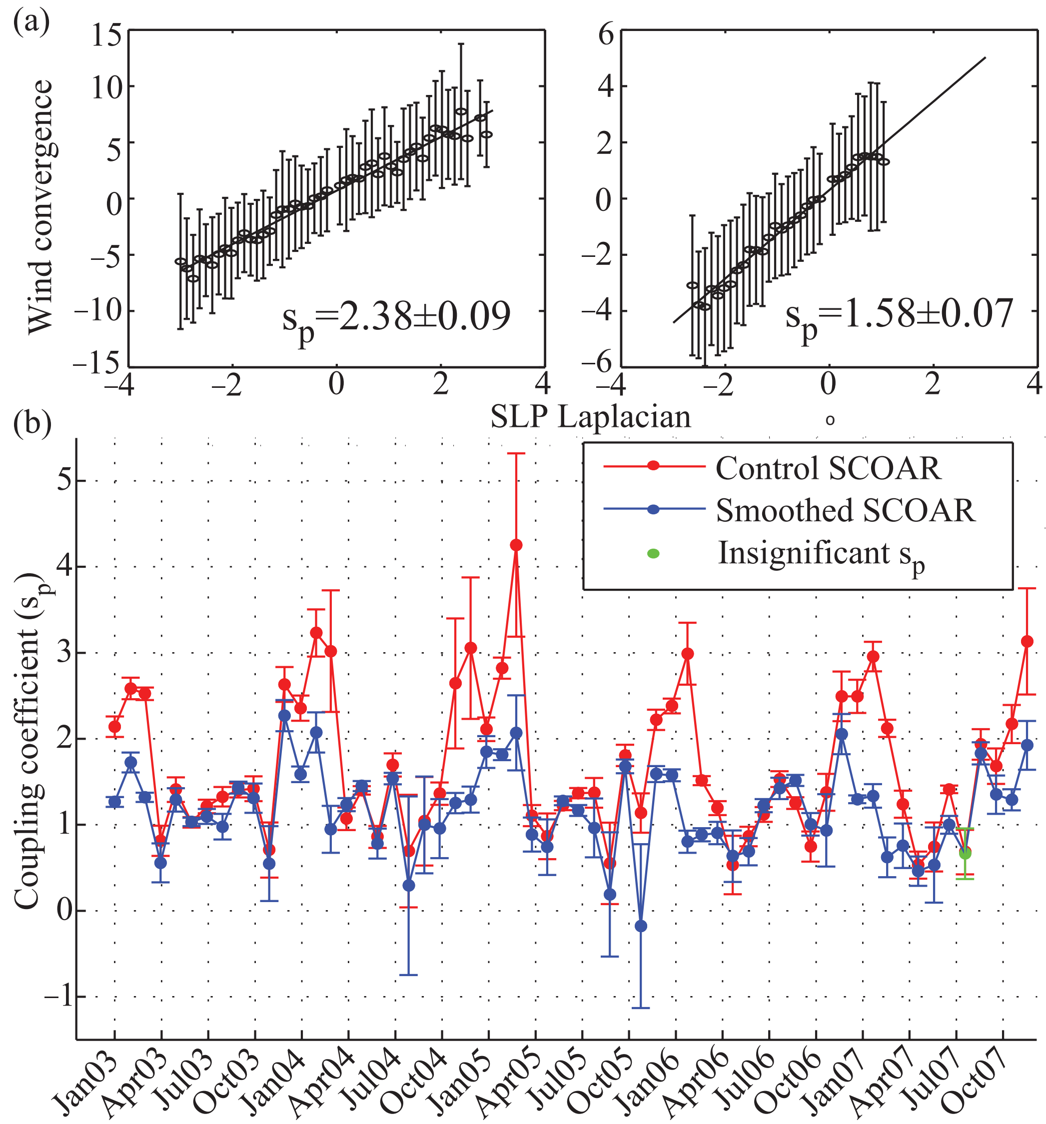

Figure 4.4: (a) Linear fits to bin-scatter plot of 10m wind convergence (10^{-6} s^{-1} against SLP Laplacian (10^{-9} Pa m^{-2}), over the same time period and domain of Fig. 4.2a, for Control SCOAR ((left) and Smoothed SCOAR (right), with coupling coefficients (s_p). (b) Time series of monthly s_p for 2003-2007 for Control SCOAR (red) and Smoothed SCOAR (blue). Error bars represent standard error of the slopes. Green dots indicate s_p with r^2 value smaller than 0.5 and p-value greater than 0.05

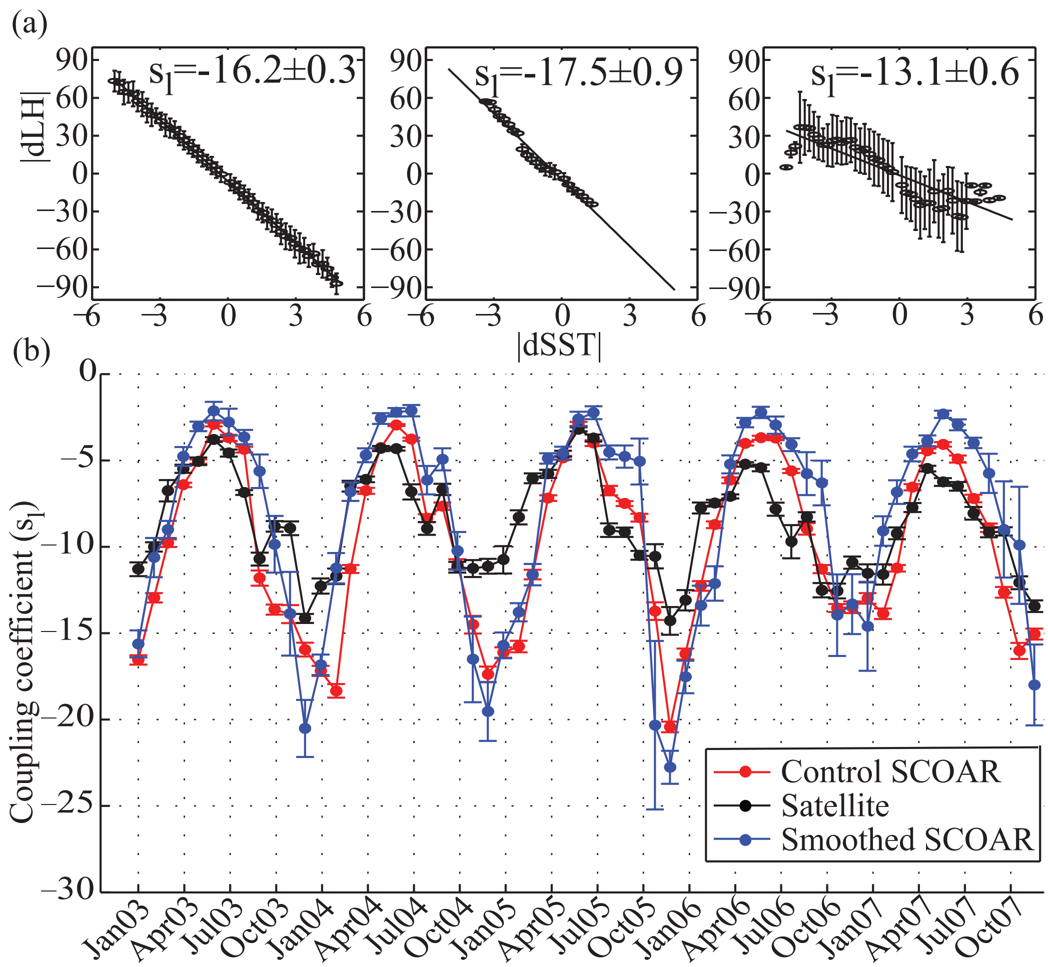

Figure 4.5: (a) Linear fits of the bin-scatter plots of spatial derivatives of latent heat flux (W/m^2 per 100km) and SST spatial derivatives (°C per 100km) over the same time period and domain of Fig. 4.2a, for Control SCOAR (left), Smoothed SCOAR (middle) and observations (right), with coupling coefficients (s_l). (b) Time series of monthly s_l for 2003-2007, for Control SCOAR (red), Smoothed SCOAR (blue) and observations (black). Solid dots indicate values that have r^2 value greater than 0.5 and p-value less than 0.05

4.2 Impact of Mesoscale SST on Precipitation

Since ocean-atmosphere interactions play a significant role in the KRS region, a deterministic approach is adopted by performing a comparative study between a Control SCOAR run and a Smoothed RSM to investigate the role of mesoscale SST on atmospheric processes, such as precipitation. Figure 4.6 gives a picture of the SST difference between the two runs, as well as the percentage of precipitation (PPT) difference for January 2001. The SST difference ranges between ±5% with an intensified region (144°E-156°E, 37°N-42°N; boxed domain in lower panel of Fig. 4.6) that corresponds with up to ±40% change in precipitation. A transect at 40.5°N (black line in top panel of Fig. 4.6) is chosen to study the vertical structure of the atmosphere and its relation to SST and precipitation.

Precipitation is often associated with convection of moist air that reaches saturation and rains out. Over open water, warmer SST sets up a low pressure anomaly and low level wind convergence, which in turn induces convection and brings moist surface air to heights where it will cool and reach saturation, and then rain out. Through such a mechanism, an alignment of SST, low-level wind convergence and precipitation would be expected.

Figure 4.7 shows a vertical profile of wind divergence at 40.5°N, overlaid with precipitation (black) and SST (red) averaged over January 2001 from Control SCOAR. Under full coupling, enhanced precipitation around 145°E-147°E, 149°E-150°E, and 154°E-156°E aligns well with low-level wind convergence(negative divergence) zone, but not SST maxima. Instead, peak precipitation coincide with negative gradients in SST. This can be attributed to the vertical mixing mechanism that induces low-level wind convergence along negative SST gradients, which in turn provides the convection needed for cloud formation and precipitation.

This idea is also supported at the mesoscale. Figure 4.8 shows the vertical cross section of difference in wind divergence between Control SCOAR and Smoothed RSM, overlaid with difference in precipitation (black) and difference in SST (red). Precipitation peaks at 146.5°E, 149.5°E and 154°E coincide with low-level peaks in wind convergence and along steep negative SST gradients. This reinforces the concept of enhanced (reduced) low-level wind convergence (divergence) induced by negative (positive) SST gradients through the vertical mixing mechanism. Convection can be measured by vertical velocity, for which Figure 4.9 illustrates the cross section of the difference in vertical pressure velocity (Pa/s) for the same transect. Precipitation and SST difference are the same as Fig. 4.8. Upward motion (negative vertical pressure velocity) also coincide with precipitation maxima and along negative SST gradients, so as to suggest that convection is induced by low-level wind convergence that arose from negative SST gradients.

The top panel of Figure 4.10 shows the distribution of precipitation difference between Control SCOAR and Smoothed RSM, overlaid with contours of SST difference, in the boxed domain (144°E-156°E, 37°N-42°N) of Fig. 4.6. Peaks and troughs of precipitation difference are not collocated with the mesoscale SST features. However, precipitation peaks and troughs have some alignment with maxima and minima in 10m wind convergence difference. This is seen on the middle panel of Figure 4.10, for which precipitation difference is overlaid with contours of difference in 10m wind convergence, where dashed (solid) contours indicate negative (positive) wind convergence. It suggests that surface wind convergence has an impact on precipitation at the mesoscale. The lower panel on Figure 4.10 is the difference in 10m wnd convergence overlaid with SST difference. Positive (negative) wind convergence generally collocates along the gradient of negative (positive) SST, suggesting that the mesoscale surface wind convergence is driven by the gradients in mesoscale SST through vertical mixing. Based on Fig. 4.10, scatterplots of precipitation difference against SST difference, and precipitation difference against 10m wind convergence difference are made (Figure 4.11). A linear regression is performed on each scatterplot and their respective coupling coefficients (slope to the linear fit) are computed, along with their corresponding r^2 coefficients. The coupling coefficient for precipitation difference against SST difference is found to be 0.06 mm/day per °C, but the huge spread of data points resulted in an associated r^2 of only 0.13, indicating that the coupling is insignificant. As for precipitation difference against 10m wind convergence difference, the data spreads less and the coupling coefficient is found to 0.21 mm/day per $1\text{x}10^{-5}\text{s}^{-1}$, with r^2=0.44. While this means that only 44% of the variance in precipitation is explained by surface wind convergence at the mesoscale, this is still significant given the nonlinearity of atmospheric processes that contribute to precipitation.

The difference between Control SCOAR and Smoothed RSM enables one the extract the impact of mesoscale SST on atmospheric process. In the KE region, it is seen that mesoscale SST gradients induces mesoscale surface wind convergence that collocate with precipitation anomalies, suggesting the important role of the vertical mixing mechanism on the mesoscale.

This chapter, in part, is being prepared for publication. Dian Ariyani Putrasahan, Arthur J. Miller, and Hyodae Seo. I am the primary investigator and author of this paper.

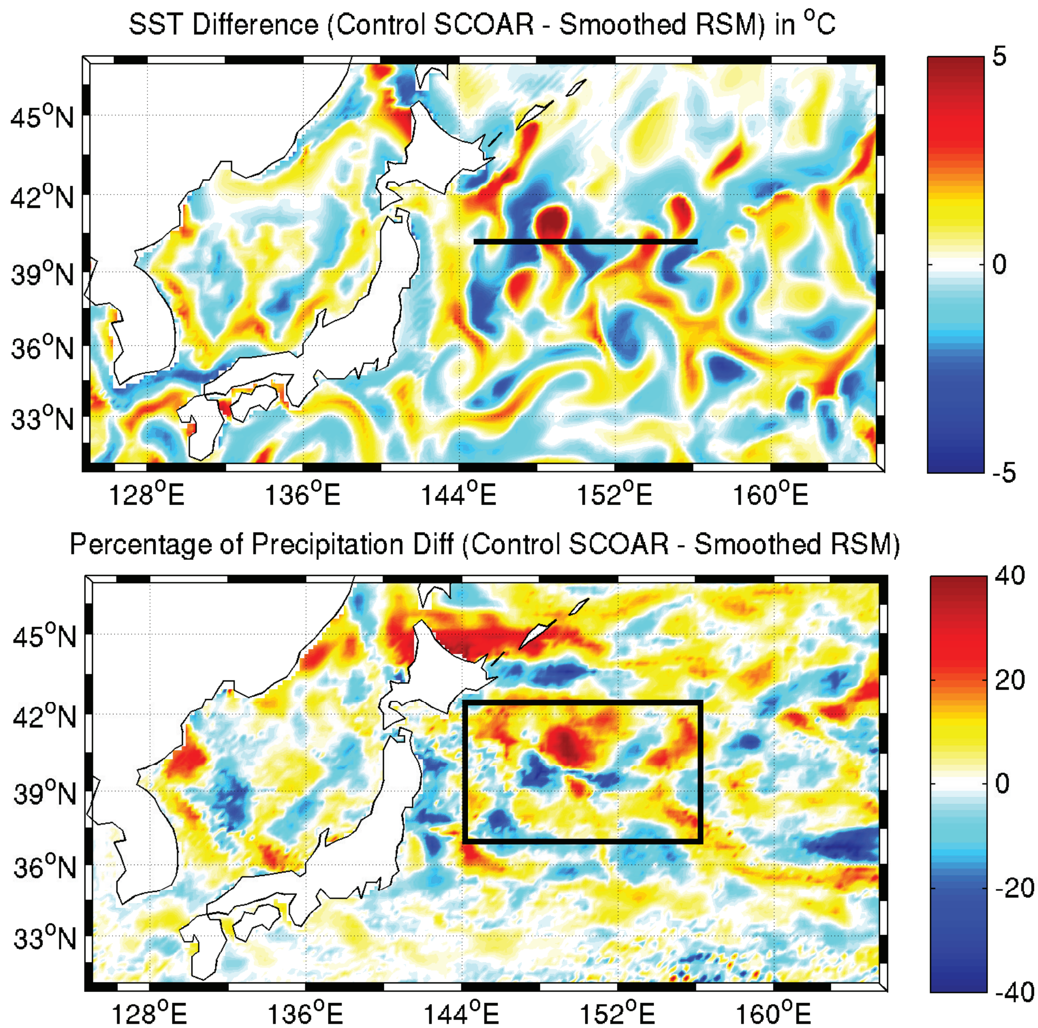

Figure 4.6: Difference in SST distribution (top) of Control SCOAR - Smoothed RSM for January 2001. Corresponding distribution of percentage difference in precipitation (bottom). Location of 40.5° transect and intensified mesoscale region [boxed domain; 144°E-156°E, 37°N-42°N] marked on top and bottom figures respectively.

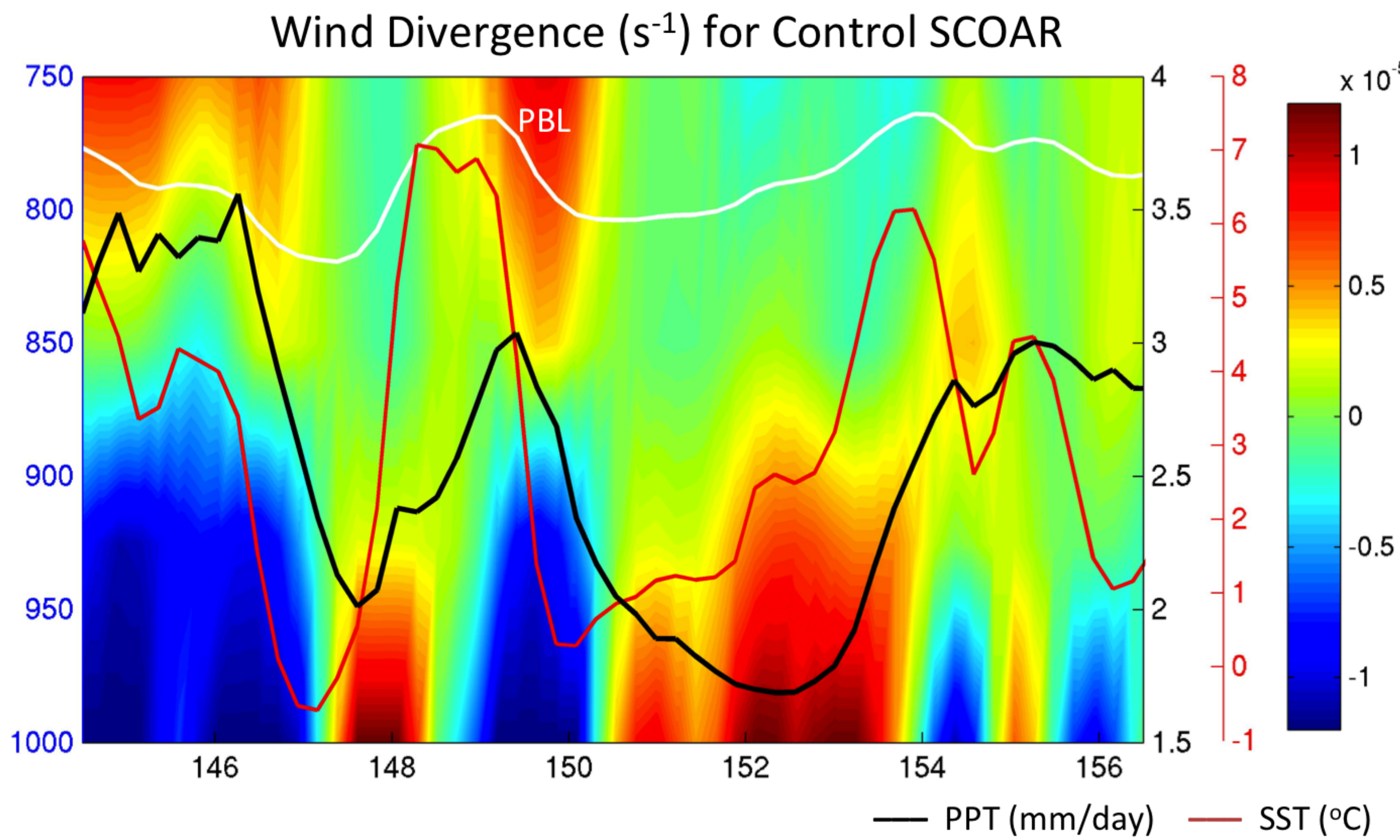

Figure 4.7: Vertical cross section of wind divergence [s^{-1}] on pressure coordinates (hPa; left blue axis) at 40°N for January 2001, based on Control SCOAR. There is an overlay of SST (°C; red), precipitation (mm/day; black) and PBL height (white) along this transect that runs from 144°E to 156°E (x-axis)

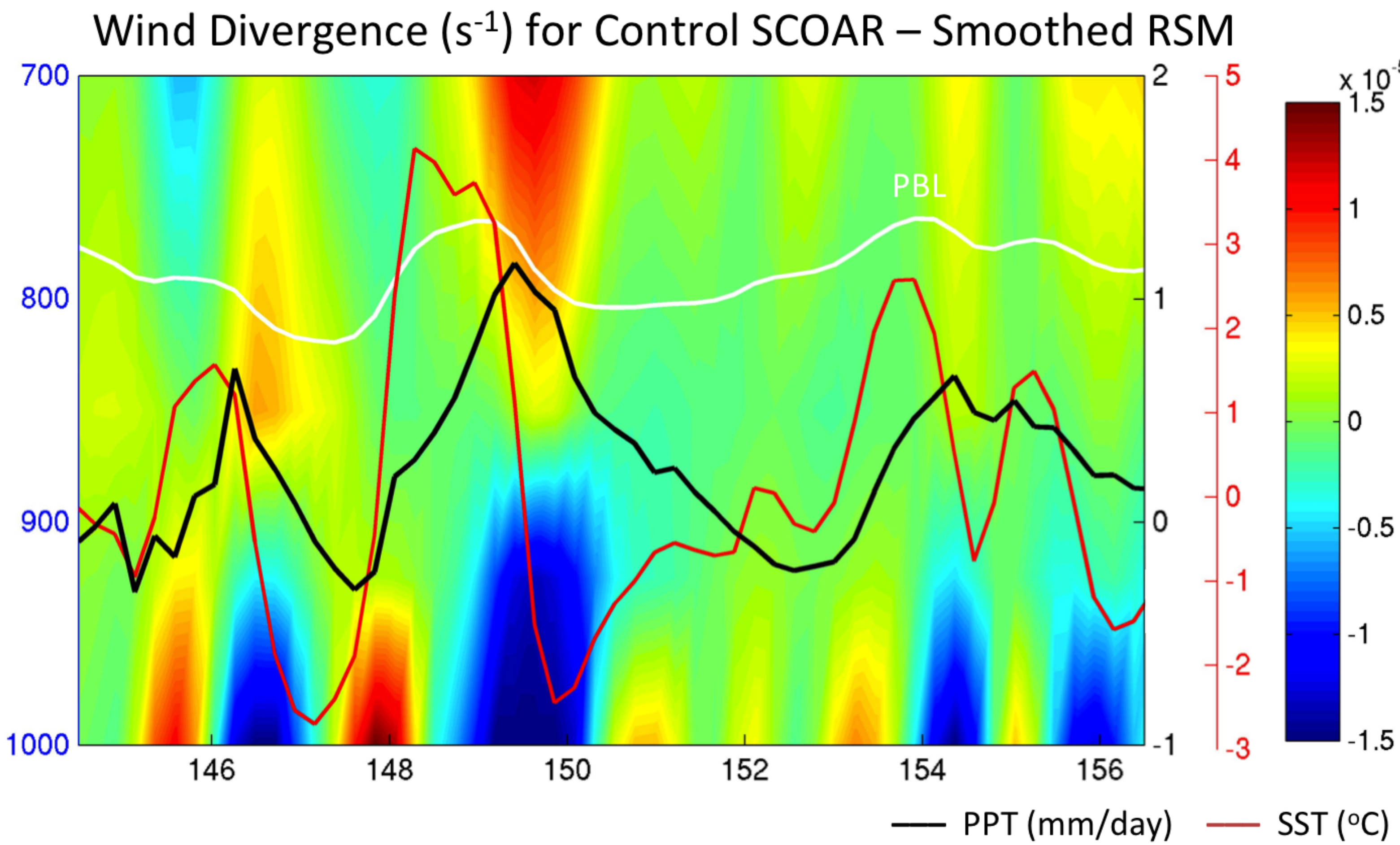

Figure 4.8: Vertical cross section of the difference in wind divergence [s^{-1})]from Control SCOAR - Smoothed RSM, at (144°E to 156°E, 40.5°N) for January 2001. There is an overlay with SST difference(°C; red), precipitation difference (mm/day; black), and PBL (white) from Control SCOAR.

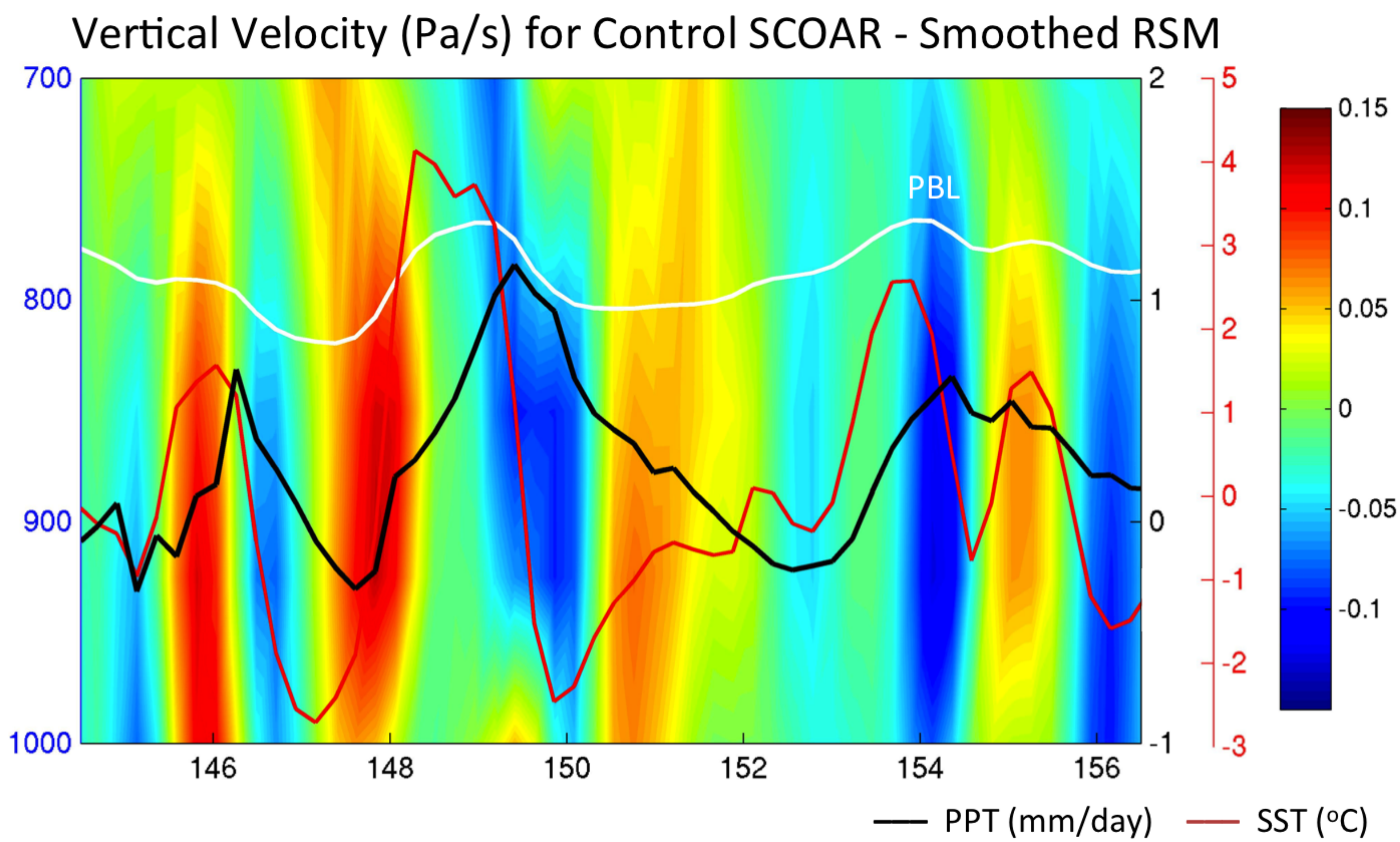

Figure 4.9: Same as Figure 4.8 except that it is the vertical cross section of the difference in vertical pressure velocity [Pa/s] from Control SCOAR - Smoothed RSM.

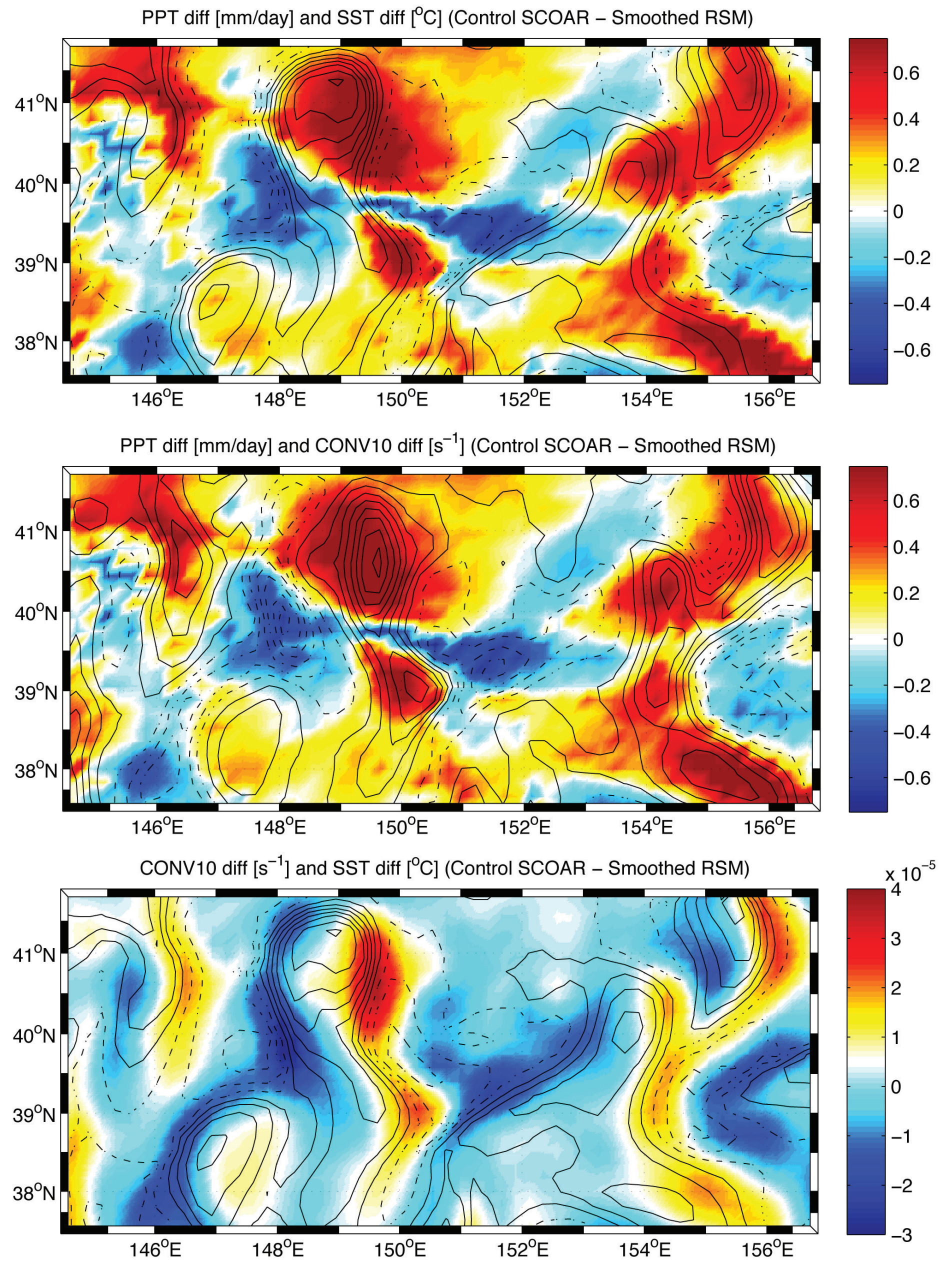

Figure 4.10: Colormap of precipitation difference [mm/day] of Control SCOAR - Smoothed RSM for January 2001, overlaid with contours of 1°C SST difference (top panel). Solid contours indicate positive SST difference, while dashed contours indicate negative SST difference. Middle panel has the same colormap of precipitation difference, but overlaid with contours of difference in 10m wind convergence [s^{-1}]. Similarly, solid contours represent positive wind convergence, and dashed contours represent negative wind convergence, with intervals of $5x10^{-6}$ s^{-1}. The bottom panel is a colormap of difference in 10m wind convergence [s^{-1}] overlaid with contours of contours of 1°C SST difference. Solid and dashed contours are the same as top panel.

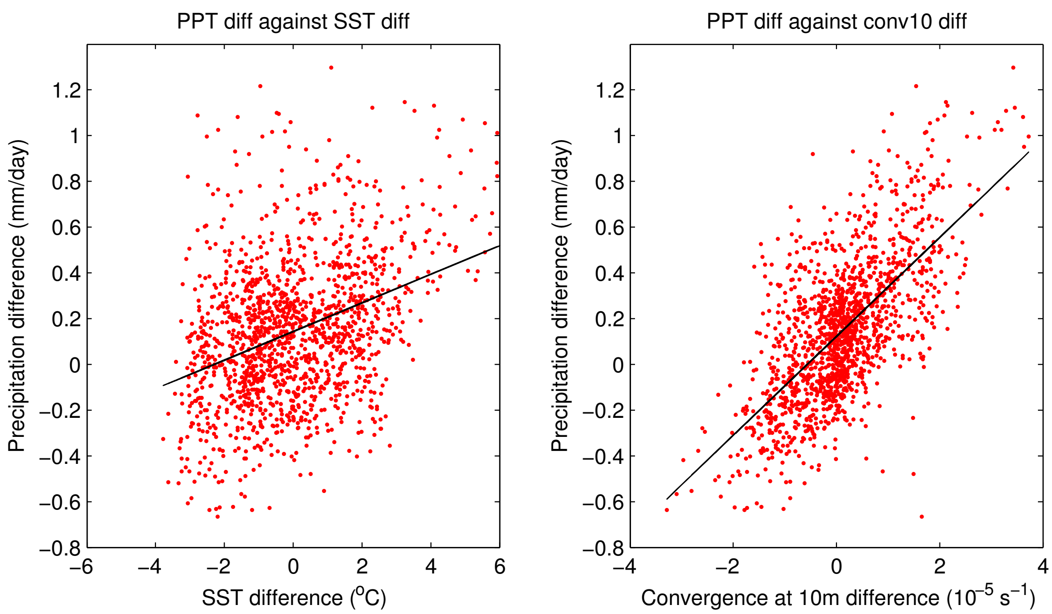

Figure 4.11: Scatterplots of precipitation difference against SST difference (right panel) and precipitation difference against 10m wind convergence difference (left panel), with linear regressions performed on each plot.

Chapter 5

Summary

The thesis has addressed several questions with regards to ocean-atmosphere interactions in the Humboldt Current System (HCS) and Kuroshio Extension (KE) region, using a coupled ocean-atmosphere regional model. The implementation of an online 2-D spatial smoother has allowed the investigation to the differences of ocean-atmosphere coupling in a fully-coupled mode versus large-scale coupled mode, and shows the importance of mesoscale coupling in cases for which ocean-atmosphere coupling is observed. In addition, the comparison of the fully-coupled case to spatially-smoothed uncoupled atmospheric run has provided the capability to extract ocean-atmosphere coupling at the mesoscale, and give a sense of the impact of mesoscale SST on atmospheric processes.

Chapter 2 provides a description of the three components in the SCOAR model, namely ROMS (ocean), RSM (atmosphere), and the SST-flux coupler. A 2-D lowess filter is implemented into the SST-flux coupler to provide a coupled framework that enables one to not only investigate the impact of mesoscale on the atmosphere and ocean, but also the effect of mesoscale coupling upon the atmosphere and ocean.

Chapter 3 section 1 presents the spatial distribution of wind stress and wind stress curl fields found in SCOAR and NCEP R2. It shows that SCOAR provides a good downscaling of NCEP R2 wind forcing that matches well with the magnitude and spatial pattern of wind stress fields found in QuikSCAT. This section explores two wind-driven upwelling processes, namely coastal Ekman upwelling and Ekman pumping, in several coastal locations and their contribution to the total wind-driven upwelling transport. In addition, it highlights the importance of the spatial pattern in wind stress field used to force the ocean, particularly along the coast. At Taltal, Tongoy (Coquimbo) and Arica, the total wind-driven upwelling transport in SCOAR and NCEP R2 have seasonally opposite signs because of the difference in the spatial distribution of the wind forcing product. At these locations, the differences in the wind stress magnitude and shifted location of wind stress maxima that affects the wind stress curl fields led to different upwelling transport (upwelling vs downwelling favorable conditions), which sets up different physical conditions for nutrient flux to the surface ocean and consequently the availability of nutrients for biological production.

In upwelling zones such as San Juan and Punta Lavapie, wind-driven upwelling in SCOAR is dominated by coastal Ekman upwelling. However, Ekman pumping can account for 20-30% of the total wind-driven upwelling transport during winter months. At these locations, the seasonal cycle of the total wind-driven upwelling transport are similar and of comparable amplitudes. However, the decomposition of the total transport to coastal Ekman upwelling transport and Ekman pumping transport reveals the difference in the relative contribution of each process to the upwelling conditions. Again, the wind product used (SCOAR vs NCEP R2) is critical to causing these differences, and thus sheds caution for attributing upwelling to a particular mechanism.

Chapter 3 section 2 sets up an experiment to study the spatial scale dependence of SST-wind stress coupling in the HCS using satellite observations, Control SCOAR (full coupling) and Smoothed SCOAR (large-scale coupling). Control SCOAR and satellite observations show a seasonal cycle in their SST-wind stress coupling (both downwind SST gradient with wind stress divergence, and crosswind SST gradient with wind stress curl) with comparable strengths and significant coupling. Although the model does not capture the seasonal cycle of the coupling, the comparison between the model runs can still serve to help understand the spatial scale-dependence of SST-wind stress coupling. Smoothed SCOAR showed no significance in SST-wind stress coupling throughout most of the run, which indicates the importance of the role of ocean mesoscale eddies on SST-wind stress coupling.

In chapter 3 section 3, an assessment of the coupling between SST, wind speed and latent heat flux within the context of a fully-coupled mode (Control SCOAR) and large-scale coupled mode (Smoothed SCOAR) is made. In both Control SCOAR and Smoothed SCOAR, no significant coupling can be drawn out between SST, wind speed and latent heat flux. However, at the mesoscale (Control SCOAR - Smoothed RSM), there is significant coupling between latent heat flux, SST and wind speed. The positive correlation between SST and surface wind speed at the mesoscale suggests that mesoscale SST anomalies have an imprint on the overlying atmospheric stability, which affects the vertical mixing of momentum onto surface mesoscale wind. Since significant coupling is also seen between mesoscale wind speed and latent heat flux as well as SST and latent heat flux at the mesoscale, the imprint of mesoscale SST on latent heat flux is attributed to both a direct influence of SST on the heat flux, as well as indirectly through the stability changes in the atmosphere that affects wind speeds and thus the latent heat flux, all at the mesoscale. The coupling between mesoscale SST and latent heat flux is significant through out 2000-2007, and in general, significant coupling between mesoscale wind speed and latent heat flux. For the times in which mesoscale wind speed and latent heat flux coupling is not significant, then significant coupling between mesoscale SST and latent heat flux is attributed to the direct impact of SST onto the latent heat flux.

Chapter 3 section 4 explores the effect of SST-wind stress coupling on ocean eddies. Control SCOAR (contains SST-wind stress coupling) and Smoothed SCOAR (does not have SST-wind stress coupling) show similarity in the shape and peak wavelength of the vorticity power spectrum. This suggests that the SST-wind stress coupling does not have an impact on the ocean eddies in the HCS. It is suspected that the weak SST gradients and SST-wind stress coupling found in HCS contributed to the lack of a rectified response of the ocean eddies. Smoothed ROMS has a larger peak in the power spectrum than the coupled cases, suggesting air-sea coupling reduces the energetics of the ocean eddies. However, the smoothing of the atmospheric forcing fields resulted in a different mean circulation near the coastal area which could change the instability properties in the ocean. As such, the larger energy in the power spectrum of Smoothed ROMS as compared to the coupled cases may be due to either or both absence of air-sea feedback and different instability properties.

Chapter 4 is the study over the Kuroshio Extension region. Section 1 investigates the spatial scale of ocean-atmosphere coupling through the vertical mixing mechanism (VMM) and pressure adjustment mechanism (PAM) by comparisons of a fully-coupled mode (Control SCOAR) and large-scale coupled mode (Smoothed SCOAR) . Within Control SCOAR, both mechanisms are significant and active, particularly during winter months. Through VMM, significant coupling between downwind SST and wind stress divergence is seen in both Control SCOAR and Smoothed SCOAR, suggesting that large-scale coupling cannot be neglected. This does not preclude that coupling on the mesoscale is insignificant in this case. VMM expressed as the the coupling between crosswind SST and wind stress divergence is also significant in Control SCOAR, but is not observed in Smoothed SCOAR. In this case, coupling found in Control SCOAR can be attributed to mesoscale coupling, where ocean eddies are essential. In the case of PAM, Control SCOAR and Smoothed SCOAR produces significant coupling, but Control SCOAR has higher coupling coefficients during the winter months. This suggests that mesoscale coupling acts to intensify the coupling within PAM during winter. Coupling between latent heat and SST is significant throughout 2003-2007 in both fully-coupled mode and large-scale coupled mode, with peak coupling during winter months.

Chapter 4 section 2 investigates the impact of mesoscale SST on precipitation for the month of January, 2001. Mesoscale SST anomalies do not collocate with precipitation anomalies, nor is there any coupling between SST and precipitation at the mesoscale. Rather, it is the 10m wind convergence anomalies that collocate with SST gradients and precipitation anomalies, and significant coupling is found between 10m wind convergence and precipitation at the mesoscale. This suggests that on the mesoscale, SST gradients induces surface wind convergence anomalies through the vertical mixing mechanism, which in turn provide changes in vertical velocities that affect precipitation anomalies.

Bibliography

Arakawa, A. and Schubert, W. H. (1974). Interaction of a cumulus cloud ensemble with the large-scale environment, part i. *Journal of Atmospheric Science*, 31:674–698.

Bryan, F., Tomas, R., Dennis, J., Chelton, D., Loeb, N., and McClean, J. (2010). Frontal scale air-sea interaction in high-resolution coupled climate models. *Journal of Climate*, 23:6277–6291.

Carton, J., Chepurin, G., and Cao, X. (2000a). A simple ocean data assimalation analysis of the glocal upper ocean 1950-1995, part 2: results. *Journal of Physical Oceanography*, 30:311–326.

Carton, J., Chepurin, G., Cao, X., and Giese, B. (2000b). A simple ocean data assimalation analysis of the glocal upper ocean 1950-1995, part 1: methodology. *Journal of Physical Oceanography*, 30:294–309.

Castelao, R. M. and Barth, J. A. (2006). Upwelling around cabo frio, brazil: The importance of wind stress curl. *Geophysical Research Letters*, 33:doi:10.1029/2005GL025182.

Cayan, D. R. (1992). Latent and sensible heat flux anomalies over the northern oceans: Driving the sea surface temperature. *Journal of Physical Oceanography*, 22:859–880.

Chelton, D., Esbensen, S., Schlax, M., Thum, N., Freilich, M., Wentz, F., C.L.Gentemann, McPhaden, M., and Schopf, P. (2001). Observations of coupling between surface wind stress and sea surface temperature in the eastern tropical pacific. *Journal of Climate*, 14:1479–1498.

Chelton, D., Schlax, M., and Freilich, M. (2004). Satellite measurements reveal persistent small-scale features in ocean winds. *Science*, 303:978–983.

Chelton, D., Schlax, M., and Samelson, R. (2007). Summertime coupling between sea surface temperature and wind stress in the california current system. *Journal of Physical Oceanography*, 37:495–517.

Chelton, D. and Wentz, F. (2005). Global microwave satellite observations of sea surface temperature for numerical weather prediction and climate research. *Bulletin of American Meteorological Society*, 86:1097–1115.

Chelton, D. and Xie, S.-P. (2010). Coupled ocean-atmosphere interaction at oceanic mesoscales. *Oceanogr.*, 23:52–69.

Cleveland, W. (1979). Robust locally weighted regression and smoothing scatterplots. *Journal of American Statistical Association*, 74:829–836.

Duhaut, T. and Straub, D. (2006). Wind stress dependence on ocean surface velocity: implications for mechanical energy input to ocean circulation. *Journal of Physical Oceanography*, 36:202–211.

Fairall, C., Bradley, E., Rogers, D., Edson, J., and Young, G. (1996). Bulk parameterization of air-sea fluxes for tropical ocean global atmosphere coupled-ocean atmosphere response experimant. *Journal of Geophysical Research*, 101:3747–3764.

Frankignoul, C., Sennechael, N., Kwon, Y.-O., and Alexander, M. (2011). Influence of the meridional shifts of the kuroshio and the oyashio extensions on the atmospheric circulation. *Journal of Climate*, 24:762–777.

Freilich, M., Long, D., and Spencer, M. (1994). Seawinds: A scanning scatterometer for adeos ii-science overview. In *Proc. Int. Geoscience and Remote Sensing Symp.*, pages 960–963. IEEE.

Garreuad, R. D. and Munoz, R. C. (2005). The low-level jet off the west coast of subtropical south america: Structure and variability. *Monthly Weather Review*, 133:2246–226.

Haack, T., Chelton, D., Pullen, J., Doyle, J., and Schlax, M. (1992). Mixed convective dynamic roll vortices and their effects on initial wind and temperature profiles. *Journal of Atmospheric Sciences*, 49:1181–1201.

Haack, T., Chelton, D., Pullen, J., Doyle, J., and Schlax, M. (2008). Summertime influence of sst on surface wind stress off the u.s. west coast from the u.s. navy coamps model. *Journal of Physical Oceanography*, 38:2414–2437.

Haidvogel, D., Arango, H., Hedstrom, K., Beckmann, A., Malanotte-Rissoli, P., and Shchepetkin, A. (2000). Model evaluation experiments in the north atlantic basin: Simulations in nonlinear terrain-following coordinates. *Dynamics of Atmospheres and Oceans*, 32:239–281.

Halpern, D. (2002). Offshore ekman transport and ekman pumping off peru during the 1997-1998 el nino. *Journal of Geophysical Research*, 29:191–194.

Hogg, A., Dewar, W., Berloff, P., Kravtsov, S., and Hutchinson, D. (2009). The effects of mesoscale ocean-atmosphere coupling on the large-scale ocean circulation. *Journal of Climate*, 22:4066–4082.

Hong, S.-Y. and Pan, H.-L. (1996). Nonlocal boundary layer vertical diffusion in a medium-range forecast model. *Monthly Weather Review*, 124:2322–2339.

Juang, H.-M. H., Hong, S.-Y., and Kanamitsu, M. (1997). The ncep regional spectral model: An update. *Bulletin of American Meteorological Society*, 78:No. 10.

Juang, H.-M. H. and Kanamitsu, M. (1994). The nmc nested regional spectral model. *Monthly Weather Review*, 122:3–26.

Kanamitsu, M., Ebisuzaki, W., Woolen, J., Potter, J., and Fiorino, M. (2002a). Ncep-dow amip-ii reanalysis (r-2). *Bulletin of the American Meteorological Society*, 83:1631–1643.

Kanamitsu, M., Kumar, A., Juang, H.-M. H., Schemm, J.-K., Wang, W., Yang, F., Hong, S.-Y., Peng, P., Chen, W., Moorthi, S., and Ji, M. (2002b). Ncep dynamical seasonal forecast system 2000. *Bulletin of the American Meteorological Society*, 83:1019–1037.

Kwon, Y.-O., Alexander, M., Bond, N., Frankignoul, C., Nakamura, H., Qiu, B., and Thompson, L. A. (2010). Role of the gulf stream and kuroshio-oyashio systems in large-scale atmosphere-ocean interaction: A review. *Journal of Climate*, 23:3249–3281.

Large, W., McWilliams, J., and Doney, S. (1994). Oceanic vertical mixing: A reivew and a model with a nonlocal boundary later parameterization. *Review in Geophysics*, 32:363–404.

Latif, M. (2006). On north pacific multidecadal climate variability. *Journal of Climate*, 19:2906–2915.

Lim, K.-S. S. and Hong, S.-Y. (2010). Development of an effective double-moment cloud microphysics scheme with prognostic cloud condensation nuclei (ccn) for weather and climate models. *Monthly Weather Review*, 138:1587–1612.

Lindzen, R. and Nigam, S. (1987). On the role of sea surface temperature gradients in forcing low-level winds and convergence in the tropics. *J. Atmos. Sci.*, 44:2418–2436.

Liu, W. (2002). Progress in scatterometer application. *Journal of Oceanography*, 58:121–136.

Liu, W., Xie, X., and Niiler, P. (2007). Ocean-atmosphere interaction over agulhas extension meanders. *Journal of Climate*, 20:5784–5797.

Ma, C.-C., Mechoso, C., Robertson, A., and Arakawa, A. (1996). Peruvian stratus clouds and the tropical pacific circulation: A coupled ocean-atmosphere gcm study. *Journal of Climate*, 9:1635–1645.

Miller, A. and Schneider, N. (2000). Interdecadal climate regime dynamics in the north pacific ocean: theories, observations and ecosystem impacts. *Progress in Oceanography*, 47:355–379.

Minobe, S., Kuwano-Yoshida, A., Komori, N., Xie, S.-P., and Small, R. (2008). Influence of the gulf stream on the troposphere. *Nature*, 452:206–209.

Minobe, S., Miyashita, M., Kuwano-Yoshida, A., Tokinaga, H., and Xie, S.-P. (2010). Atmospheric response to the gulf stream: Seasonal variations. *Journal of Climate*, 23:3699–3719.

Mizuno, K. and White, W. (1983). Annual and interannual variability in the kuroshio current system. *Journal of Physical Oceanography*, 88:1847–1867.

Moorthi, S. and Suarez, M. J. (1992). Relaxed arakawa-schubert: A parameterization of moist convection for general circulation models. *Monthly Weather Review*, 120:978–1002.

Nakamura, H., Sampe, T., Tanimoto, Y., and Shimpo, A. (2004). *Observed Associations Among Storm Tracks, Jet Streams and Midlatitude Oceanic Fronts*, volume 147 of *Geophysical Monograph*. American Geophysical Union.

Nonaka, M. and Xie, S.-P. (2003). Covariations of sea surface temperature and wind over the kuroshio and its extension: Evidence for ocean-to-atmosphere feedback. *Journal of Climate*, 16:1404–1413.

O'Neill, L., Chelton, D., and Esbensen, S. (2003). Observations of sst-induced perturbations of the wind stress field over the southern ocean on seasonal time scales. *Journal of Climate*, 16:2340–2354.

O'Neill, L., Chelton, D., Esbensen, S., and Wentz, F. (2005). High-resolution satellite measurements of the atmospheric boundary later response to sst variations along the agulhas return current. *Journal of Climate*, 18:2706–2723.

Pickett, M. H. and Panduan, J. D. (2003). Ekman transport and pumping in the california current based on the u.s. navys high-resolution atmospheric model (coamps). *Journal of Geophysical Research*, 108:doi:10.1029/2003JC001902.

Renault, L., Dewitte, B., M.F., Garreaud, R., Echevin, V., and Bonjean, F. (2009). Impact of atmospheric coastal jet off central chile on sea surface temperature from satellite observations (20002007). *Journal of Geophysical Research*, 114:doi:10.1029/2008JC005083.

Reynolds, R., Gentemann, C., and Wentz, F. (2004). Impact on trmm ssts on a climate-scale sst analysis. *Journal of Climate*, 17:2938–2952.

Samelson, R., Barbour, P., Barth, J., Bielli, S., Boyd, T., Chelton, D., Kosro, P., Levine, M., Skyllingstad, E., and Wilczak, J. (2002). Wind stress forcing of the oregon coastal ocean during the 1999 upwelling season. *Journal of Geophysical Research - Oceans*, 107:doi10.1029/2001/JC000900.

Samelson, R., Skyllingstad, E., Chelton, D., Esbensen, S., O'Neill, L., and Thum, N. (2006). On the coupling of wind stress and sea surface temperature. *Journal of Climate*, 19:1557–1566.

Sasaki, H., Nonaka, M., Masumoto, Y., Sasai, Y., Uehara, H., and Sakuma, H. (2008). An eddy-resolving hindcast simlation of the quasi-global ocean from 1950 to 2003 on the earth simulator.

Sasaki, H., Sasai, Y., Nonaka, M., Masumoto, Y., and Kawahara, S. (2006). An eddy-resolving simulation of the quasi-global ocean driven by satellite-observed wind field: Preliminary outcomes from physical and biological fields. *J. Earth Simul.*, 6:34–49.

Schlax, M., Chelton, D., and Freilich, M. (2001). Sampling errors in wind fields constructed from single and tandem scatterometer datasets. *Journal of Atmospheric and Oceanic Technology*, 18:1014–1036.

Seo, H., Jochum, M., Murtugudde, R., and Miller, A. (2006). Effect of ocean mesoscale variability on the mean state of tropical atlantic climate. *Geophysical Research Letters*, 33(L09606):doi:10.1029/2005GL025651.

Seo, H., Jochum, M., Murtugudde, R., and Miller, A. (2007a). Effect of ocean mesoscale variability on the mean state of tropical atlantic climate. *Geophysical Reseach Letters*, 33.

Seo, H., Miller, A., and Roads, J. (2007b). The scripps coupled ocean-atmosphere regional (scoar) model, with applications in the eastern pacific sector. *Journal of Climate*, 20:381–402.

Seo, H., Murtugudde, R., Jochum, M., and Miller, A. (2008). Modeling of mesoscale coupled ocean-atmosphere interaction and its feedback to ocean in the western arabian sea. *Ocean Modelling*, 25:120–131.

Shchepetkin, A. and McWilliams, J. (2005). The regional oceanic modeling system (roms): a split-explicit, free-surface, topography-following-coordinate ocean model. *Ocean Modelling*, 9:347–404.

Sherman, K. and Hempel, G. (2008). The unep large marine ecosystem report: A perspective on changing conditions in lmes of the worlds regional seas. Technical Report 182, United Nations Environment Programme. Nairobi, Kenya.

Shimada, T. and Minobe, S. (2011). Global analysis of the pressure adjustment mechanism over sea surface temperature fronts using airs/aqua data. *Geophysical Reseach Letters*, 38.

Small, R., de Szoeke, S., O'Neill, L., Seo, H., Song, Q., Cornillon, P., Spall, M., and Minobe, S. (2008). Air-sea interaction over ocean fronts and eddies. *Dynamics of Atmospheres and Oceans*, 45:274–319.

Smith, R. L. (1968). Upwelling. *Oceanography and Marine Biology Annual Review*, 6:11–46.

Spall, M. (2007). Notes and correspondence: Effect of sea surface temperature-wind stress coupling on baroclinic instability in the ocean. *Journal of Physical Oceanography*, 37:1092–1097.

Taguchi, B., Nakamura, H., Nonaka, M., and Xie, S.-P. (2009). Influences of the kuroshio/oyashio extensions on air-sea heat exchanges and storm-track activity as revealed in regional atmospheric model simulations for the 2003/04 cold season. *Journal of Climate*, 22:6536–6560.

Takatama, K., Minobe, S., Inatsu, M., Xie, S.-P., and Small, R. (2011). Diagnostics for near-surface wind convergence/ divergence response to the gulf stream in a regional atmospheric model. *Atmospheric Science Letters*, 12:206–209.

Thum, N., Esbensen, S., Chelton, D., and McPhaden, M. (2002). Air-sea heat exchange along the northern sea surface temperature front in the eastern tropical pacific. *Journal of Climate*, 15:3361–3378.

Tokinaga, H., Tanimoto, Y., Xie, S.-P., Sampe, T., Tomita, H., and Ichikawa, H. (2009). Ocean frontal effects on the vertical development of clouds over the western north pacific: In situ and satellite observations. *Journal of Climate*, 22:4241–4260.

Veechi, G., Xie, S., and Fischer, A. (2004). Ocean-atmosphere covariability in the western arabian sea. *Journal of Climate*, 17:1213–1224.

Wallace, J., Mitchell, T., and Deser, C. (1989). The influence of sea surface temperature on surface wind in the eastern equatorial pacific: seasonal and interannual variability. *Journal of Climate*, 2:1492–1499.

Wallace, J., Smith, C., and Jiang, Q. (1990). Spatial patterns of atmosphere-ocean interaction in the northern winter. *Journal of Climate*, 3:990–998.

Wentz, F., Gentemann, C., Smith, D., and Chelton, D. (2000). Satellite measurements of sea surface temperature through clouds. *Science*, 288:847–850.

Wentz, F. and Meissner, T. (2000). Algorithm theoretical basis document (atbd) version 2: Amsr ocean algorithm. Technical Report 121599A, Remote Sensing Systems.

Xie, S.-P. (2004). Satellite observations of cool ocean-atmosphere interaction. *Bulletin of American Meteorological Society*, 85:195–209.

Yu, C. and Weller, R. (2007). Objectively analyzed air-sea heat fluxes for the global oce-free oceans (1981-2005). *Bulletin of American Meteorological Society*, 88:527–539.

Zhang, G. and McFarlane, N. A. (1995). Sensitivity of climate simulations to the parameterization of cumulus convection in the canadian climate centre general circulation model. *Atmosphere-Ocean*, 3:407–446.